A Catalog of Galaxy Clusters Observed by XMM-Newton

S. L. Snowden[1], R. M. Mushotzky
Code 662, NASA/Goddard Space Flight Center, Greenbelt, MD 20771
and

K. D. Kuntz
Henry A. Rowland Department of Physics and Astronomy, The Johns Hopkins University, 366 Bloomberg Center, 3400 N. Charles Street, Baltimore, MD 21218
and

David S. Davis[2]
Department of Physics, University of Maryland, Baltimore County, 1000 Hilltop Circle, Baltimore, MD 21250

ABSTRACT

Images and the radial profiles of the temperature, abundance, and brightness for 70 clusters of galaxies observed by *XMM-Newton* are presented along with a detailed discussion of the data reduction and analysis methods, including background modeling, which were used in the processing. Proper consideration of the various background components is vital to extend the reliable determination of cluster parameters to the largest possible cluster radii. The various components of the background including the quiescent particle background, cosmic diffuse emission, soft proton contamination, and solar wind charge exchange emission are discussed along with suggested means of their identification, filtering, and/or their modeling and subtraction. Every component is spectrally variable, sometimes significantly so, and all components except the cosmic background are temporally variable as well. The distributions of the events over the FOV vary between the components, and some distributions vary with energy. The scientific results from observations of low surface brightness objects and the diffuse background itself can be strongly affected by these background components and therefore great care should be taken in their consideration.

Subject headings: x-rays: observations, clusters of galaxies, analysis: methods

1. Introduction

Clusters of galaxies are the largest and most massive collapsed objects in the universe, and as such they are sensitive probes of the history of structure formation. While first discovered in the optical band in the 1930s (for a review see Bahcall (1997)), in some ways the name is a misrepresentation since most of the baryons and metals are in the hot X-ray emitting intercluster medium and not the galaxies. Clusters are more fundamentally "X-ray objects" as it is this energy range where this preponderance of the baryons is visible. Studies of their evolution can place strong constraints on all theories of large scale structure and determine precise values for many of the cosmological parameters. As opposed to galaxies, clusters probably retain all the enriched material created in

[1]Steven.L.Snowden@nasa.gov
[2]CRESST and Astroparticle Physics Laboratory, NASA/GSFC, Greenbelt, MD 20771

them and being essentially closed boxes they provide a record of nucleosynthesis in the universe. Thus measurement of the elemental abundances and their evolution provide fundamental data for the origin of the elements. The distribution of the elements in the clusters reveals how the metals were removed from stellar systems into the IGM. Clusters should be "fair" samples of the universe and studies of their mass and their baryon fraction should reveal the "gross" properties of the universe as a whole. Since most of the baryons are in the gaseous phase and clusters are dark matter dominated, the detailed physics of cooling and star formation are much less important than in galaxies. This makes clusters much more amenable to detailed simulation than galaxies or other systems in which star formation has been a dominant process. While gravity is clearly dominant in massive systems, much of the entropy of the gas in low mass systems is produced by processes other than shocks – an indication of the importance of non-gravitational processes in structure formation at lower mass scales.

Clusters are luminous, extended X-ray sources and are visible out to high redshifts with present day technology. The virial temperature of most groups and clusters corresponds to $T \sim 2 - 100 \times 10^6$ K ($kT \sim 0.2 - 10$ keV, velocity dispersions of $180 - 1200$ km s^{-1}), and while lower mass systems certainly exist we usually call them galaxies. Most of the baryons in groups and clusters of galaxies lie in the hot X-ray emitting gas that is in virial equilibrium with the dark matter potential well (the ratio of gas to stellar mass is $\sim 2 - 10 : 1$, Allen, Schmidt, & Fabian (2001)). This gas is enriched in heavy elements (Mushotzky et al. 1978) and is thus the reservoir of stellar evolution in these systems. The presence of heavy elements is revealed by line emission from H and He-like transitions as well as L shell transitions of the abundant elements. Most clusters and groups are too hot to have significant line emission from C or N but all abundant elements with $z > 8$ (Oxygen) have strong lines from H and He-like states in the X-ray band and their abundances can be well determined.

Clusters of galaxies were discovered as X-ray sources in the late 1960's (see Mushotzky (2002) for a historical review) and large samples were first obtained with the *Uhuru* satellite in the early 1970's (Jones & Forman 1978). Large samples of X-ray spectra and images were first obtained in the late 1970's with the *HEAO* satellites (see Jones & Forman (1984) for a early review). The early 1990's brought large samples of high quality images with the *ROSAT* satellite and good quality spectra with *ASCA* and *Beppo-SAX*. In the last few years there has been an enormous increase in the capabilities of X-ray instrumentation due to the launch and operation of *Chandra* and *XMM-Newton*. Both *Chandra* and *XMM-Newton* can find and identify clusters out to $z > 1.2$ and their morphologies can be clearly discerned to $z > 0.8$. Their temperatures can be measured to $z \sim 1.2$ and *XMM-Newton* can determine their overall chemical abundances to $z \sim 1$ with a sufficiently long exposure. For example, a cluster at $z = 1.15$ has recently had its temperature and abundance well constrained by a 1 Ms *XMM-Newton* exposure (Hashimoto et al. 2004).

Temperature and abundance profiles to $z \sim 0.8$ can be well measured and large samples of X-ray selected clusters can be derived. *Chandra* can observe correlated radio/X-ray structure out to $z > 0.1$ and has discovered internal structure in clusters. The *XMM-Newton* grating spectra can determine accurate abundances for the central regions of clusters in a model independent fashion for oxygen, neon, magnesium, iron silicon.

1.1. Temperature Structure of Clusters

As discussed in detail by Evrard (2003), we now have a detailed understanding of the formation of the dark matter structure for clusters of galaxies. If gravity has had the only important physical effect since the formation, then the gas should be in hydrostatic equilibrium and its density and temperature structure should provide a detailed measurement of the dark matter distribution in the cluster. Recent theoretical work has also taken into account other process such as cooling which can be important. The fundamental form of the Navarro, Frenk, & White (1997) dark matter potential and the assumption that the fraction of the total mass that is in gas is constant with radius results in a prediction that the cluster gas should have a declining temperature profile at a sufficiently large distance from the center (in R/R_{viral} units), both from analytic (Komatsu & Seljak 2001) and numerical model-

ing (Loken et al. 2002). The size of the temperature drop in the outer regions is predicted to be roughly a factor of 2 by $R/R_{viral} \sim 0.5$. This prediction is consistent with the *ASCA* results of Markevitch et al. (1998). However there is considerable controversy about the analysis and interpretation of temperature profiles from *ASCA* (White & Buote (2000); Kikuchi et al. (1999)). Irwin & Bregman (2000) and de Grandi et al. (1999) analyzed the *Beppo-SAX* data with the former finding isothermal gas and the latter a temperature gradient in the "cooling" flow clusters. *XMM-Newton* is perfect for resolving this controversy, having a much better point spread function than *ASCA* and much more collecting area than *Beppo-SAX* and *Chandra* and having a larger field of view than *Chandra*. However there is a selection effect due to the smaller *XMM-Newton* field of view than *ASCA*, and in order to go out to the virial radius in one pointing one must observe clusters at $z > 0.1$. Additional insights into the profiles of clusters was obtained from the *ROSAT*, *ASCA*, and *Beppo-SAX* missions but the instrumental limitations left significant differences in the determination of the cluster temperature profiles (Markevitch et al. (1998); Irwin, Bregman, & Evrard (1999); White (2000); Irwin & Bregman (2000); Finoguenov, Arnaud, & David (2001); de Grandi & Molendi (2001)). There are several published results from *XMM-Newton* Majerowicz, S., Neumann, & Reiprich (2002); Pratt & Arnaud (2002)) and a review by Arnaud, Pointecouteau, & Pratt (2005). The analysis of Arnaud, Pointecouteau, & Pratt (2005) indicates that there may be a temperature drop at even larger radii but the relatively high *XMM-Newton* background and uncertainties in modeling it makes the results somewhat uncertain. The origin of the difference between some of the *Beppo-SAX*, *ASCA* and *XMM-Newton* results is not clear. It is thus possible that there is a difference between the low z systems studied by *Beppo-SAX* and *ASCA* and the higher redshift systems studied by *XMM-Newton* and/or a selection effect in the objects so far analyzed with *XMM-Newton*. The recent *Chandra* results of Vikhlinin et al. (2006) show a temperature profile in good agreement with the Markevitch et al. (1998) results and the standard theory. *XMM-Newton* and *Chandra*, do not suffer from the PSF problems of *ASCA* and *Beppo-SAX* and have much broader energy ranges that the *ROSAT* mission. Analysis of samples of cooling flow clusters with *XMM-Newton* (Piffaretti et al. (2005); Pratt et al. (2007)) and *Chandra* (Vikhlinin et al. 2005) are mostly consistent with the *ASCA* profiles which showed the temperature profiles decline in the outer parts of the clusters (Markevitch et al. 1998). However flatter profiles have also been found (Allen, Schmidt, & Fabian (2001); Kaastra et al. (2004); Arnaud, Pointecouteau, & Pratt (2005)) with *XMM-Newton* and *Chandra* observations.

The measurement of the cluster mass function can provide a sensitive cosmological test but are sensitive to the observational parameters especially at large radius. Recent simulations show that cluster temperature profiles decline with radius but less rapidly than is shown by previous X-ray analysis (e.g., Kay et al. (2004)). The total mass is quite sensitive to the temperature profile (Rasia et al. 2006) which needs to be well determined to large radii.

In this paper we consider a large sample of clusters observed with the *XMM-Newton* observatory and derive temperature, density and abundance profiles for many of these systems out to the virial radius using a new technique of background subtraction.

1.2. Analysis of Extended Sources

The analysis of extended sources in X-ray astronomy is typically problematic and quite often very complex. This is particularly true for objects which subtend the entire field of view (FOV) of the observing instrument such as nearby galaxies, relatively nearby clusters of galaxies, many regions of galactic emission, and of course the cosmic diffuse background. Even with objects smaller than the FOV, quite often the simple subtraction of a nearby "background" region from the same data set is inappropriate due to spectral and spatial variations in the internal background and angular variations in the cosmic background. The use of deep "blank sky" observations can also be inappropriate due to the same considerations, as well as the probability that many background components are temporally varying. Because of the temporal variation of the background, the average of the blank-sky data, even after normalization, may not match the conditions of a specific observation

of interest, and so may yield an incorrect result.

While the cores of many clusters are relatively bright in X-rays and so the treatment of the background is not such a significant consideration, at the edges of clusters it is absolutely critical. Clusters fade gently into the backgrounds at large radii. Therefore improving the modeling of the backgrounds extends the reliable determination of cluster parameters to larger radii.

Critical to compensating for the various background components by filtering, subtraction, or modeling is a basic understanding of their origin and effects on the detectors. Unfortunately this usually takes a considerable amount of time to develop, which is why useful methods for a specific observation become available to the general community only years into the mission. Even then, the methods will continue to evolve with greater understanding of the various background components and their temporal evolution (if any), and the operation of the instruments. In addition, the efforts are quite often undertaken by individuals who are not project personnel, but whose scientific interests require the improved analysis methods.

This is certainly true of the *XMM-Newton* mission and observations using the EPIC instruments. Several groups have presented methods and published scientific results based upon them (Arnaud et al. (2001); Read & Ponman (2003); Nevalainen, Markevitch, & Lumb (2005); de Luca & Molendi (2004)). As opposed to past methods which derive background spectra from normalized blank-sky observations, this paper presents the details of a method based as much as possible on the specific understanding of the individual background components. This method was used successfully in the paper identifying the solar wind charge exchange emission in the *XMM-Newton* observation of the Hubble Deep Field North (Snowden, Collier, & Kuntz 2004).

Section 2 of this paper gives a short description of the *XMM-Newton* observatory, § 3 discusses the various background components and the suggested methods used to compensate for them, § 4 demonstrates the data reduction method using the observation of Abell 1795. § 5 applies the methods to the determination of the temperature, abundance, and flux radial profiles of a catalog of 70 clusters of galaxies and presents the results, and § 6 discusses the conclusions. Note that the detailed discussion of the science derived from these observations is deferred to Paper II.

Currently the specific method and software package discussed here are only applicable to EPIC MOS data. This is due to physical differences between the MOS and pn detectors and not to differences in the nature of the backgrounds experienced by them. In time it is likely that the analysis methods described here will be extended to the pn.

2. *XMM-Newton* and the EPIC MOS Detectors

The *XMM-Newton* observatory (Ehle et al. 2005) orbits the Earth in a long period ($\sim$ 48 hours) highly elliptical path (the original perigee and apogee were $\sim$ 6000 km and $\sim$ 115,000 km but they have since evolved over the mission to $\sim$ 19,000 km and $\sim$ 103,000 km as of 2006 June). The scientific package of *XMM-Newton* is comprised of six independent but co-aligned instruments which operate simultaneously. The European Photon Imaging Camera (EPIC) is comprised of three CCD imagers of two distinct technologies (MOS and pn), and are coupled to the three X-ray mirror assemblies. The EPIC instruments provide imaging over a $\sim 30'$ FOV with moderate energy resolution. Half of the light from two of the X-ray mirrors (those with the MOS detectors) are diverted by reflection gratings to the Reflection Grating Spectrometer (RGS), two instruments which provide high spectral resolution for point sources and small-scale extended objects ($< 2'$). The final scientific instrument is the Optical Monitor (OM) which is an optical/UV telescope with a FOV only somewhat smaller than that of EPIC ($\sim 20'$).

The EPIC MOS detectors are each comprised of seven individual CCDs where one is roughly centered on the optical axis and the others form a hexagonal pattern surrounding it. The central CCD can be operated independently in several different observation modes (imaging, windowed imaging, and timing) while the outer CCDs always operate in the standard imaging mode. There are three optical blocking filters (thin, medium, and thick) which can be set by the observer. The filter wheel has a circular aperture with a $30'$ diameter which leaves portions of the outer CCDs shielded

from exposure to the sky. These unexposed corners of the detectors play a vital role in the modeling of the quiescent particle background (QPB) as described below. The filter wheel also has settings which expose the CCDs to an on-board calibration source (cal-closed position) and which block the sky (filter wheel closed position, FWC), data from the latter position are also used in modeling the QPB. 13 of the 14 MOS CCDs are still functioning as of 2007 March, one of the MOS1 outer CCDs (CCD #6) was lost to a micrometeorite hit on 2005 March 9.

3. EPIC MOS Background Components

There are five major contributors to the background of EPIC MOS (and pn) observations that we consider here. However, the characterization of some components as background is occasionally debatable as they may actually be the main scientific interest of an observation. The first is the quiescent particle background, a continuum component produced by the interaction of high energy penetrating particles with the detectors. Generally included with, but distinct from, the QPB are fluorescent X-rays (FX) which are produced by the particle flux interacting with various components of the satellite and then are detected by the instruments. For the MOS the fluorescent X-rays are dominated by Al Kα ($E \sim 1.49$ keV) and Si Kα ($E \sim 1.75$ keV), but there are also lines from other elements at higher energies (Au, Cr, Mn, Fe, Ni, Zn). The continuum QPB dominates at high (above ~ 2 keV) and low (below ~ 1.2 keV) energies while the Al and Si lines dominate the $1.3 - 1.9$ keV band.

The third background component is also produced locally at the detectors and is caused by soft protons (SP, $E \sim 10 - 100$ keV) which travel down the telescope light path and deposit their energy directly in the detectors. The SP spectrum is a power-law continuum and varies both in magnitude and hardness.

For many observations the fourth component, the cosmic X-ray background (CXB), is a source of contamination although it can also be the scientific goal of the observation. The diffuse CXB dominates below ~ 1 keV and has a thermal spectrum dominated by emission lines. It is superposition of Galactic emission from multiple sources as well as Galactic halo and perhaps even more distant emission, and is strongly variable over the sky. Included in the CXB is the unresolved emission from the superposition of cosmological objects (e.g., AGN, Hickox & Markevitch (2007)) which dominates at higher energies and Galactic stars with a relatively minor contribution at lower energies (Kuntz & Snowden 2001). The average spectrum of the cosmological emission is for the most part a power law continuum with a possible change in slope at lower energies. There is thought to be a true cosmic variation of magnitude on the sky but there is also the obvious variation caused by the excision of point sources to various levels.

The fifth background component, solar wind charge exchange emission (SWCX, e.g., Wargelin et al. (2004); Snowden, Collier, & Kuntz (2004)), like the CXB, can either be background or a source of scientific interest, although admittedly to a rather limited community. SWCX in the MOS energy band is essentially all line emission at energies less than ~ 1.3 keV and is strongly variable in both total magnitude and relative line strengths. For the MOS detectors of *XMM-Newton* the strongest SWCX emission is from C VI, O VII, O VIII, Ne IX, and Mg XI, although this ignores the $\frac{1}{4}$ keV band where *ROSAT* observations were occasionally affected by very strong SWCX emission.

3.1. Quiescent Particle Background

The QPB for the EPIC MOS detectors has been well studied by Kuntz & Snowden (2007) (hereafter KS07) and is the dominant background above ~ 2.0 keV. In general it is relatively featureless and resembles a power law which is not folded through the instrumental effective area. Figure 1 shows MOS1 and MOS2 spectra compiled from observations with the filter wheels closed while Figure 2 shows FWC images in several bands. In this configuration no particles or X-rays passing down the telescope tube can penetrate to the detectors. Also, the on-board calibration sources are not visible to the detectors. The FOV of the detectors for cosmic X-rays and soft protons is constrained by a circular aperture indicated by the circles in the figure. The permanently shielded regions of the CCDs, i.e., the corner regions outside of the circles in Figure 2, are read out the same as those within the FOV and experience roughly the same QPB flux.

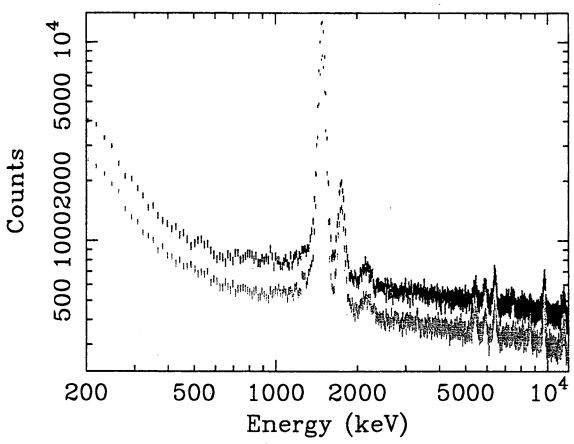

Fig. 1.— Filter wheel closed spectra for the MOS1 (green) and MOS2 (blue) detectors. The MOS2 data have been scaled by a factor of 1.5 in order to separate the spectra for clarity. The spectra are comprised of a general continuum from the with QPB and the FX lines of Al, Si, Au, and other elements.

The QPB spectra for the two detectors (Figure 1) are very similar and show a strong continuum with the Al Kα and Si Kα lines, as well as a few lines from other elements. Figure 2 shows the images of the FWC data in several different energy bands. The distribution of counts over the detectors is clearly not uniform, and in addition the contributions from the Al Kα and Si Kα fluorescent lines are distributed somewhat differently from the average as well.

In addition to the spatial variation of the QPB over the detectors, there is also a temporal variation in the spectra both in magnitude and in hardness. Figure 3 (top panel) shows the QPB count rates from the CCD corners outside of the FOV. The temporal variation is due both to changes in the CCDs and their operating conditions as well as variations of the particle flux over the course of the solar cycle. Some of the short-term scatter is due to the varying conditions during the orbit ($\sim$ 2 days). Observations can take place both inside and outside of the magnetosheath and at various distances from the particle belts. Figure 3 (bottom panel) shows the QPB hardness ratio (the ratio of the 2.0 – 8.0 keV band to the 0.5 – 1.2 keV band) over the course of the mission for the individual CCDs. Of note is the occasional deviations

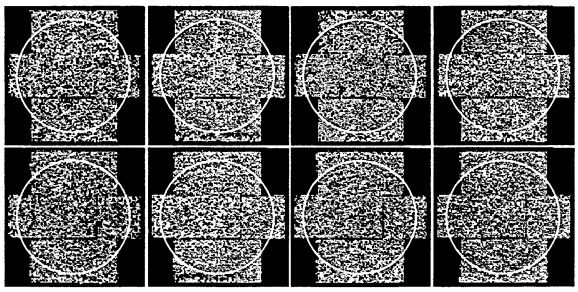

Fig. 2.— Image in detector coordinates of the FWC data for the MOS1 (upper row) and MOS2 (lower row) detectors. The data are from (left to right) the 0.35 – 1.25, 1.25 – 2.0, 2.0 – 4.0, and 4.0 – 8.0 keV bands, and have been binned into 25″ × 25″ pixels. The 1.25 – 2.0 band is most affected by the FX contamination, and it is likely that there is some difference between the spatial distributions between FWC and open data due to the different source geometry. Note that all of the bands show at least somewhat different structure. The circles indicate the FOV regions of the instruments outside of which the detectors are always shielded from cosmic X-rays.

of CCD #5 of both instruments as well as MOS1 CCD #4 from relatively nominal levels and the loss of MOS1 CCD #6 near revolution (orbit) 950. These deviations are due to a strong enhancement in the background below $E \sim 1$ keV and are extensively discussed in KS07.

3.1.1. Treatment of the QPB

In all of the discussion above only the quiescent part of the particle background is considered, these are the time periods not affected by flares. In general, times of particle background flaring are so intense that the instruments must be turned off for their health. Periods of less intense flaring are easily filtered out by light-curve screening, which is discussed in § 3.2.1.

The QPB for an individual observation (primary observation, PO) can be modeled and subtracted with, in general, quite high reliability using the FWC data in conjunction with data from the unexposed corners of the CCDs (KS07). The modeling is a multi-step process, and is done for each detector and CCD individually. The process creates a background spectrum tailored for the

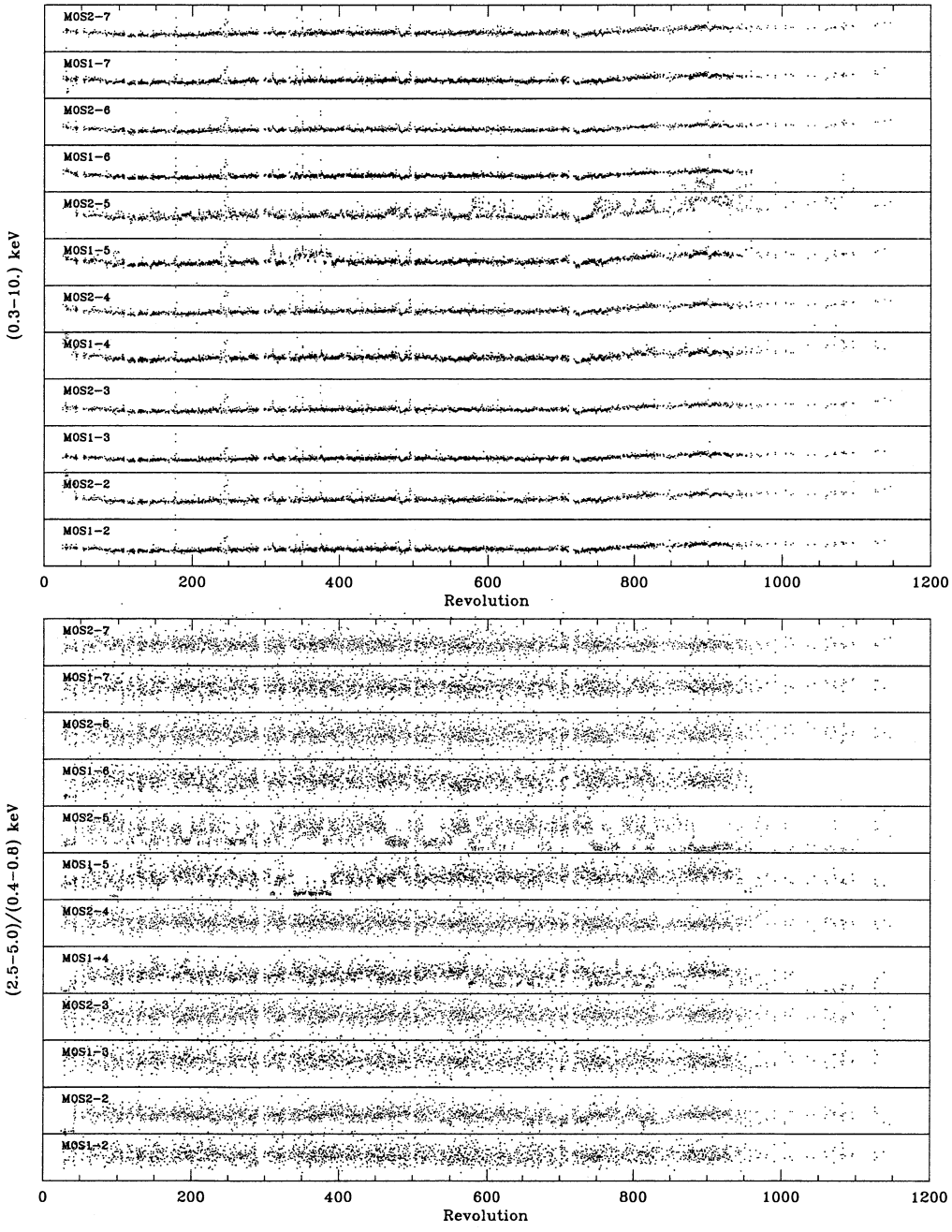

Fig. 3.— Top Panel: QPB count rate in the $0.3-10.0$ keV band from the out of FOV corners of the detectors from KS07 (their Figure 6) for the individual CCDs from both MOS instruments. The MOS1 data are shown in black, the MOS2 data are shown in blue, and time periods of anomalous CCD background behavior are shown in red. Bottom Panel: QPB $(2.5-5.0$ keV$)/(0.4-0.8$ keV) hardness from the out of FOV corners of the detectors from KS07 (their Figure 7) for the individual CCDs from both MOS instruments. The MOS1 data are shown in black, the MOS2 data are shown in blue, and time periods of anomalous CCD background behavior are shown in red.

specific region of interest where the spectrum of an astrophysical object is extracted. To summarize the process outlined in KS07: 1) After the PO has been screened for flares, the spectra from the unexposed corners of the outer CCDs are extracted. 2) The magnitudes ($2.0-8.0$ keV band) and hardness ratios ($2.0-8.0$ keV band to the $0.5-1.2$ keV band) for the spectra are determined. 3) A data base of all archived observations is searched for observations (secondary observations, SO) whose unexposed corner spectra have similar magnitudes and hardness. 4) The PO spectra are then augmented by the SO spectra increasing the statistical significance of individual spectral bins to a useful level. This step makes the assumption that data collected from time periods of similar spectral magnitude and hardness have in aggregate the same spectrum. This appears to generally be the case although CCDs #4 and #5 in their anomalous states can be problematic. 5) Spectra from the FWC data are extracted from CCD corners as well as from the region of interest. If the region of interest is comprised of more than one CCD, the individual CCD spectra are kept separate. 6) For the outside CCDs the FWC spectra from the region of interest are scaled, spectral bin by spectral bin, by the ratio of the augmented observation spectra from the CCD corners to the FWC spectra from the corners. 7) For reasons discussed in § 3.1.2 below, the spectral region affected by the Al Kα and Si Kα lines ($1.2-2.0$ keV) is cut out and replaced by an interpolated power law. The EXPOSURE and BACKSCAL keywords in the background spectrum are set to be consistent with the PO. The spectrum is then included as background in spectral fitting.

3.1.2. Treatment of the FX Background

There are two reasons why the Al-Kα and Si-Kα FX background can not be treated in the same manner as the QPB. First, the environment with the filter wheel open (with the thin, medium, and thick filters) is different from that with the filter wheel closed, and therefore the distribution and magnitude of the FX background are unlikely to be the same. Second, there are quite large numbers of counts in the lines providing high statistics. Because of this, even the slight residual variations in the instrumental gains (within the gain uncertainty) can produce large residuals. The most straight-forward method for treating the lines is to fit them as separate Gaussian model components where the line energy is allowed to vary to achieve an acceptable fit.

3.2. Soft Proton Background

The SP background is produced by relatively low energy protons ($\sim 10-100$ keV) passing down the telescope tube, penetrating the filters, and depositing their energy directly in the CCDs. This is a very problematic component which can vary from undetectable levels (by examination of the count rate) to strong flaring of over one hundred counts per second rendering the observation useless for the study of all but the brightest point sources. The SP spectrum is a continuum with variable hardness. The distribution of SP events across the FOV is different from both cosmic X-rays and the QPB, and varies as well with energy. Figure 4 shows SP background images collected from time intervals of slightly enhanced background ($\sim$ 1 counts s^{-1}) for several energy bands. While there is a significant variation in the distributions from low to high energies, and between the two detectors, they are relatively similar at energies > 2.0 keV for the individual detectors where the SP contribution is relatively stronger.

3.2.1. Treatment of the SP Background

The primary treatment of the SP background is to filter the data by creating a light curve and excluding all time intervals with a count rate greater than some selected threshold. There are a number of different filtering methods in the literature but they all give basically the same results. Since most, if not all observations contain residual SP contamination at some level, the setting of the threshold becomes dependent on a trade-off between the level of that contamination and the amount of the exposure left over after the screening. Our goal is to retrieve as much useful data as possible so rather than setting a strict limit to exclude all possible time periods of SP contamination (e.g., de Luca & Molendi (2004)), we follow the working assumption that there will be residual contamination which will be modeled during the spectral fitting process.

The filtering light curve is usually extracted in a high-energy band (e.g., $2.5-12.0$ keV) and may

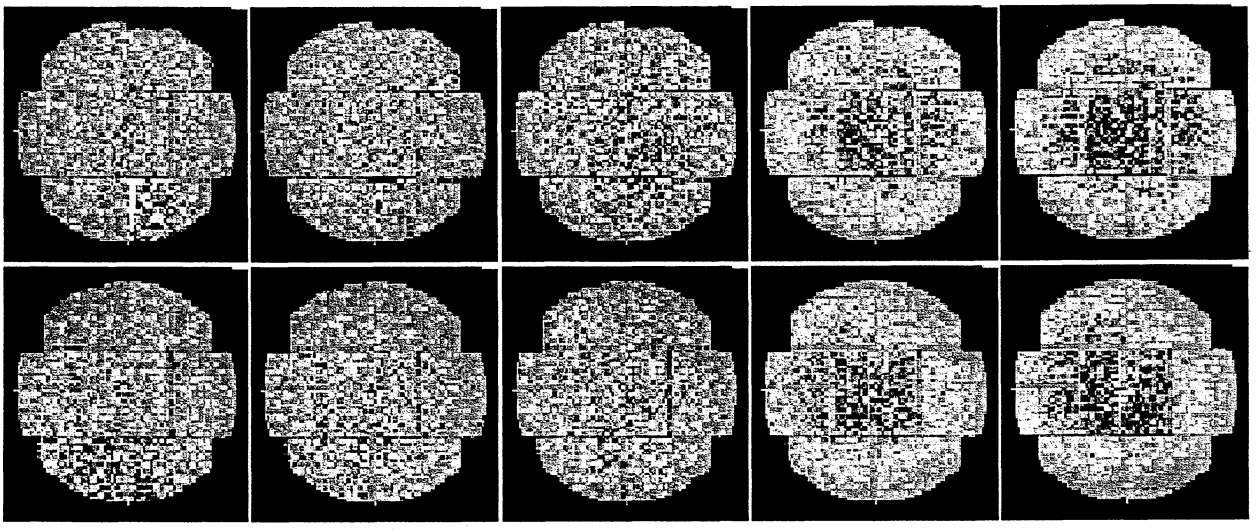

Fig. 4.— Image in detector coordinates of the SP data for the MOS1 (upper row) and MOS2 (lower row) detectors. From left to right the data are from the $0.35 - 0.8$ keV, $0.8 - 1.25$ keV, $1.25 - 2.0$ keV, $2.0 - 4.0$ keV, and $4.0 - 8.0$ keV bands. For better statistics, data are from the observations using all filters have been combined as there is little difference between the distributions for the thin, medium, and thick filter observations separately. Note that the distributions are not flat across the detectors nor are they symmetrically vignetted like cosmic X-rays. As well, the distributions are not the same for different energies.

or may not have had point sources excluded. However, only infrequently is there a source in the field which is bright, sufficiently hard, and variable enough to significantly affect the filtering process. The light curve can be filtered either by setting a fixed absolute threshold, or more creatively by using the light curve of the specific observation to set the threshold. We use this method in our analysis of the clusters presented here (see § 4). In this method a histogram is made of the light curve count rate which typically has a roughly Gaussian peak with a high count-rate tail. A Gaussian is then fit to the peak of the distribution and the threshold set at the mean value of the Gaussian plus some number of sigma (typically about 1.5). A second threshold can, and in general probably should also be set at the mean value minus the same number of sigma to avoid biasing the data to lower count rates. The fitted width of the Gaussian can give an indication of residual low level contamination, although examination of the light curve can often do the same. The benefit of this more complicated screening method is that it works well for observations of bright, hard extended objects (e.g., clusters of galaxies).

As noted above, even after screening there may well be residual SP contamination in the data. This can be accommodated in the spectral fitting process by the inclusion in the model of a power law component which is not folded through instrument effective area. Care needs to be taken, however, as power from the source signal can be transferred to the SP component.

Also note, again, that the screening process is inherently a trade-off between the amount of data available for analysis and how clean those data are. Figure 5 shows examples of two observation light curves along with the light curve histograms. As can be seen, the extent of the contamination in a given observation is extremely variable, as well as the magnitude of that contamination. Also be aware that even though a light curve may look relatively flat, there is no guarantee that there is no contamination. Although the longer that the observation count rate looks constant, the more likely it is that the level of contamination is minimal.

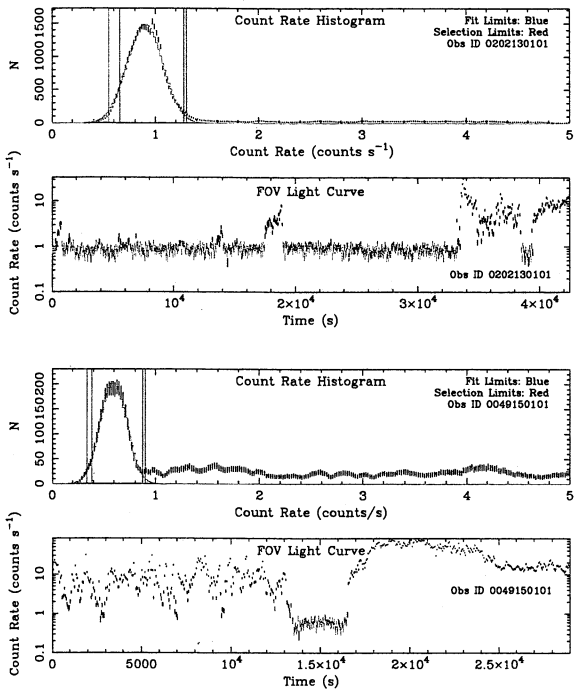

Fig. 5.— Sample light curves and light-curve histograms from two observations with different levels of SP contamination. The top two panels show the light-curve histogram and light curve for the data from ADS/Sa.XMM#0202130101 while the bottom two panels show the same for ADS/Sa.XMM#0049150101.

3.3. Solar Wind Charge Exchange Background

This is a relatively infrequent but insidious contributer to the backgrounds of extended objects, and particularly of observations of the diffuse background. SWCX emission is produced as the solar wind flows out from the Sun and interacts with material in the solar system. This includes both interstellar neutral material from the Local Cloud (Lallement 2004) flowing through the solar system and exospheric material at Earth's magnetosheath (Robertson & Cravens 2003). The highly ionized atoms in the solar wind collide with the neutral material and pick up electrons in excited states from which they radiatively decay. In the MOS energy band this includes emission from C VI, O VII, O VIII, Ne IX, and Mg XI, some of which are commonly used for plasma temperature, density, and ionization equilibrium diagnostics.

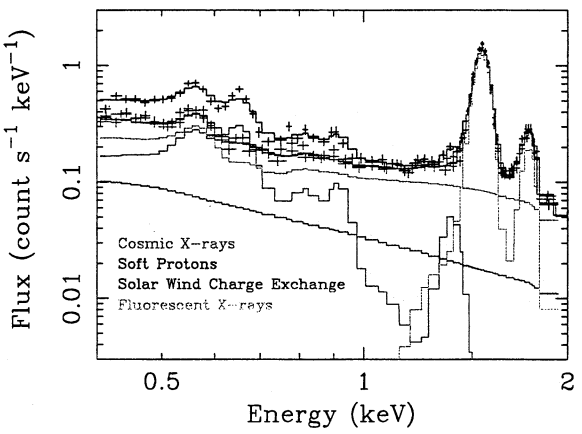

Fig. 6.— Spectra from two of the four *XMM-Newton* EPIC MOS observations of the Hubble Deep Field North (ADS/Sa.XMM#0202130101 in black and ADS/Sa.XMM#0049150101 in red). The black data points and curve show the spectrum from the contaminated observation while the red data points and curve show an uncontaminated spectrum. The uncontaminated spectrum agreed well with the two other observations of this direction. The additional curves show the fitted model contributions to the fits where all components besides the SWCX emission were fit simultaneously for the two spectra.

Figure 6 shows the example of SWCX emission from Snowden, Collier, & Kuntz (2004), an analysis of four observations of the Hubble Deep Field North (HDF-N). Displayed are two spectra from the same direction collected at different times (separated by two weeks). Since the cosmic background does not vary with time, the spectra should be the same except for the possibility of SP contamination which would be a continuum enhancement rather than the clear emission lines. The O VII (0.56 keV) and O VIII (0.65 keV) lines are particularly clearly seen as excesses. For about 40 ks of the contaminated observation there was no significant indication in the $0.5-0.75$ keV light curve that there was anything unusual happening. If there were no other observations of the HDF-N and if the contaminated observation lasted only for that 40 ks, there would have been no reason *a priori* to suspect the data.

3.3.1. *Treatment of the SWCX Background*

Because the SWCX emission originates externally to the satellite and is unlikely to show any angular structure in the *XMM-Newton* FOV, it is inseparable from the cosmic background. Depending on the length of the observation and the specific SWCX occurrence, the contamination may or may not be detectable in the observation light curve. The emission is at energies less than 1.5 keV, primarily in the $0.5 - 1.0$ keV band, so a light curve of that band may show variation in the diffuse count rate while the light curve in the hard band ($2.0 - 8.0$ keV) would not. SWCX contamination may also be detectable in the spectrum. There can be very strong O VIII and Mg XI emission unfittable by any normal equilibrium or normal abundance plasma models. There are also certain observation geometries which may be more susceptible to SWCX contamination than others, specifically any line of sight which passes near the subsolar point of Earth's magnetosheath (Robertson & Cravens 2003).

3.4. Cosmic X-ray Background

The CXB is comprised of many components which vary considerably over the sky. At high energies ($E > 1$ keV) and away from the Galactic plane the dominant component is the extragalactic power law. Most of this power law represents the superposition of the unresolved emission from discrete cosmological objects (i.e., AGN). There is considerable discussion considering the uniformity of this emission over the sky and what the true form of the spectrum is (e.g., whether the slope changes for energies less than 1 keV (Tozzi et al. 2006). The contribution of this component to the observed spectrum is clearly going to be dependent on the extent to which point sources have been excluded from the analysis. The emission is also absorbed by the column of Galactic material along the line of sight.

At lower energies there is a greater variety of components, most of which have thermal emission spectra. In the solar neighborhood the Local Hot Bubble (LHB, Snowden et al. (1998) and references therein) provides the dominant contribution near $\frac{1}{4}$ keV. The LHB is an irregularly shaped region surrounding the Sun with a radial extent of ~ 30 pc to over 100 pc (preferentially extended out of the plane of the Galaxy) which is filled with a plasma of $T \sim 10^6$ K. The cavity, or absence of significant amounts of neutral material, is well studied with ISM absorption line measurements (e.g., Sfeir et al. (1999)). In the halo of the Galaxy there is additional plasma with $T \sim 10^6$ K. The distribution of this plasma is quite patchy and probably has a relatively low scale height. There is additional general diffuse emission at $\frac{3}{4}$ keV which may be associated with the Galactic halo or perhaps the local group (McCammon et al. 2002; Kuntz, Snowden, & Mushotzky 2001). Except for the emission from the LHB, these components are all absorbed by the column density of the Galactic ISM.

Also contributing to the cosmic X-ray background are a wide variety of distinct Galactic objects, some of which subtend large angles on the sky. Loop I is a nearby superbubble which has a diameter of $\sim 100°$, and its emission is combined with the Galactic X-ray bulge which extends to $|b| > 45°$. There are supernova remnants, the Galactic ridge, and the unresolved emission from stars all contributing to the CXB with varying spectra affected by varying amounts of absorption. The CXB at $\frac{1}{4}$ keV, $\frac{3}{4}$ keV, and 1.5 keV can vary by an order of magnitude over the sky, and it can vary independently between those bands (although to a lesser extent for the $\frac{3}{4}$ keV and 1.5 keV bands). Figure 7 displays the *ROSAT* All-Sky Survey (RASS) sky maps in the $\frac{1}{4}$ keV, $\frac{3}{4}$ keV, and 1.5 keV band from Snowden et al. (1997).

3.4.1. *Treatment of the Cosmic X-ray Background*

The CXB is the dominant background component at energies less than 1.35 keV, i.e., below the Al Kα and Si Kα instrumental lines. It is significant in all directions and it can not be modeled as a single spectrum independent of position on the sky. The variation in both spectral shape and magnitude makes it very problematic to separate from the source of interest when the source covers a large fraction or all of the instrument FOV. This is particularly troublesome for the study of objects like clusters of galaxies where the source emission fades into the background at an uncertain rate and radius. Several unanswered scientific questions are dependent on the true temperature radial profile and mapping that profile to the greatest possible

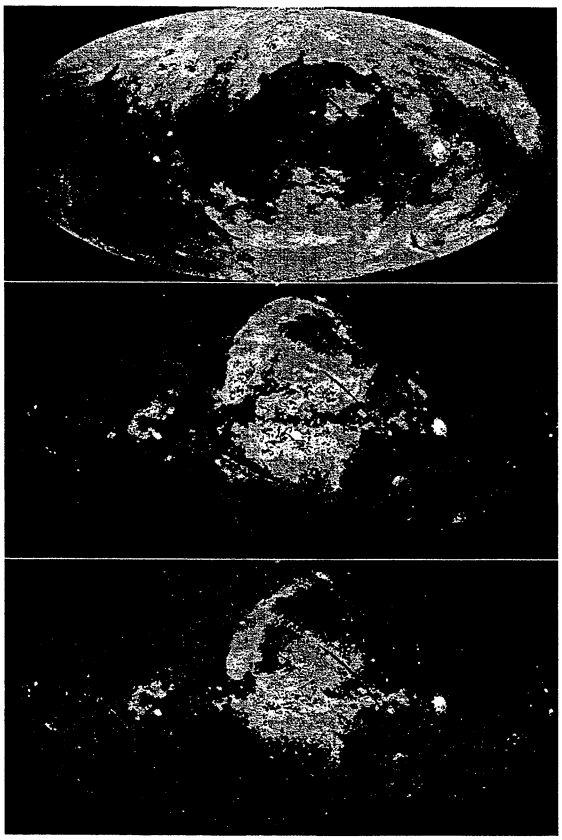

Fig. 7.— All-sky maps in the $\frac{1}{4}$ keV (upper), $\frac{3}{4}$ keV (middle), and 1.5 keV (lower) bands from Snowden et al. (1997) in an Aitoff-Hammer projection with the Galactic center at the center with longitude increasing to the left. Red and while indicate higher intensities while purple and blue indicate lower intensities.

radius is critical.

In the absence of an otherwise source-free region within the field of view there is no way to subtract CXB from the source spectrum as (as noted above) the use of blank-field data may be inappropriate. Because of this, the CXB should be modeled as part of the fitting process. Unfortunately, it is easy to transfer significant power between the various background components of a source with low surface brightness. It is therefore desirable to constrain the fits to the greatest extent possible. One method for doing so for the CXB is to use spectra from the *ROSAT* All-Sky Survey. A publicly-available tool (http://heasarc.gsfc.nasa.gov/cgi-bin/Tools/xraybg/xraybg.pl) at the High Energy Science Archive Research Center (HEASARC) extracts seven-channel spectra from the data of Snowden et al. (1997) for user-defined regions (circular or annuli). These data can be simultaneously fit, after proper correction for the observed solid angle, with the *XMM-Newton* MOS data by a standard model for the CXB. For example (and this will be demonstrated in § 4 below for Abell 1795) a CXB RASS spectrum can be extracted for an annulus surrounding the cluster, but not including it. With the assumption that the annulus spectrum is a good representation of the CXB in the direction of the cluster, a model including 1) an unabsorbed $\sim$ 0.1 keV thermal spectrum representing the LHB, 2) an absorbed $\sim$ 0.1 keV thermal spectrum representing the cooler Galactic halo emission, 3) an absorbed $\sim$ 0.25 keV thermal spectrum representing the hotter halo emission (and/or emission from the local group), and 4) an $E^{-1.46}$ power law representing the unresolved cosmological emission can be fit to the RASS and MOS data, with additional components representing the cluster, SP, and FX components fit only to the MOS data.

4. Abell 1795 – A Case Study

Abell 1795 is a well-studied nearby cluster of galaxies. It was chosen for the example presented here as it was used by Nevalainen, Markevitch, & Lumb (2005) for their discussion of the analysis of *XMM-Newton* observations of extended objects. The observation (ADS/Sa.XMM#0202130101) was taken on 2000 June 26 with an exposure of $\sim$ 49.6 ks. The pointing direction was α, δ = 207.2208°, 26.5922°.

The preparation of the data for analysis presented below uses the XMM-ESAS package prepared by the NASA/Goddard Space Flight Center XMM-Newton Guest Observer Facility (GOF) in conjunction with the ESA Science Operations Center (SOC) and the Background Working Group (BGWG, http://). The software is publicly available through both the GOF and SOC and is provided with a manual.

4.1. Temporal Filtering

The Abell 1795 observation was relatively clean by visual observation of its light curve with just a few excursions to high count rates from SP contamination. Figure 8 shows the results from the temporal filtering algorithm. Filtering the data reduced the exposure to 36.5 ks, roughly 75% of the original observation. However, the slight ripple in the light curve indicates that there is likely to be some residual SP contamination.

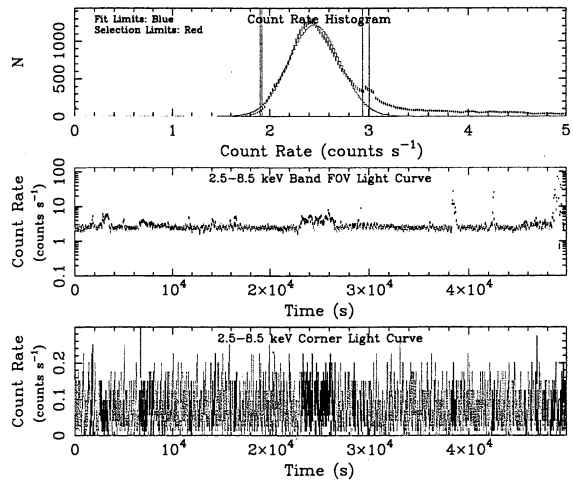

Fig. 8.— Temporal filtering results for the MOS1 Abell 1795 cluster observation with ObsID 0097820101. The upper panel plots the light curve histogram for the $2.5 - 8.5$ keV band from the FOV, the middle panel displays the $2.5 - 8.5$ keV band FOV light curve, and the lower panel displays $2.5 - 8.5$ keV band light curve from the unexposed corners of the instrument. The histogram is derived from the smoothed light curve. In the upper panel, the blue vertical lines show the range for the Gaussian fit, the green curve shows the Gaussian fit, while the red vertical lines show the upper and lower bounds for filtering the data. In the bottom two panel green points indicate accepted data while black points indicate data excluded by the filtering algorithm. The high count rate excursions are produced by soft protons rather than a particle background flare as the latter case would produce a mirror increase in the corner data.

In the screening process a light curve with a 1 s binning in the $2.5 - 8.5$ keV band was first created from the photon event file (PEF). This light curve, binned by 50 s, is shown in the the middle panel of Figure 8. The light curve is smoothed with a 50 s running average and a histogram created from the smoothed data (upper panel). The presence of the SP contamination is shown by the high count-rate tail of the of the otherwise relatively Gaussian distribution. That the flaring in the light curve is not caused by an increase in the high-energy particle background is shown by the corner count rate (lower panel) not having similar enhancements. The histogram is searched for the maximum and a Gaussian is fit to the data surrounding the peak. A count-rate cut of the light curve is made by setting thresholds at $\pm 1.5\sigma$ on either side of the fitted peak channel. Note that the setting of these thresholds is somewhat arbitrary, and that there is no absolute answer. With cleaner data wider limits can be set, but always it is a trade-off between the amount of accepted data and how clean those data are.

4.2. Extraction of Spectra

After the data have been screened spectra can be extracted and model background spectra created. For this analysis of Abell 1795 the goal is the determination of the temperature radial profile, thus the extracted spectra will be from concentric annuli. For this process we use XMM-ESAS perl scripts and FORTRAN software (Snowden & Kuntz 2006), which also require various SAS tasks.

Extraction selection expressions consistent with the requirements for the SAS task *evselect* are required for the annuli. These are most easily created using SAS and the *xmmselect* task and its interface with the *ds9* image display software. From *xmmselect* an image was created in detector coordinates (*DETX* and *DETY*). The detector coordinates of the center of Abell 1795 was determined from the image, and then the desired region descriptions defined. As an example of the region selection descriptors,

((DETX,DETY) IN circle(201,-219,2400))
&&!((DETX,DETY) IN circle(201,-219,1200))

selects data from the MOS1 detector from the $1' - 2'$ annulus. The numbers 201 and -219 are detector coordinates (*DETX* and *DETY*) of the cluster center while the numbers 1200 and 2400 are the inner and outer radii of the annulus, all in units of 0.05 arc seconds. The annulus is created by selecting all data within the first circle but not

within the second circle (the "&&" symbol is used for the Boolean "and" and the "!" symbol is used for the Boolean "not"). Note that the DETX and DETY positions for a given sky position in the MOS1 and MOS2 detectors will be different.

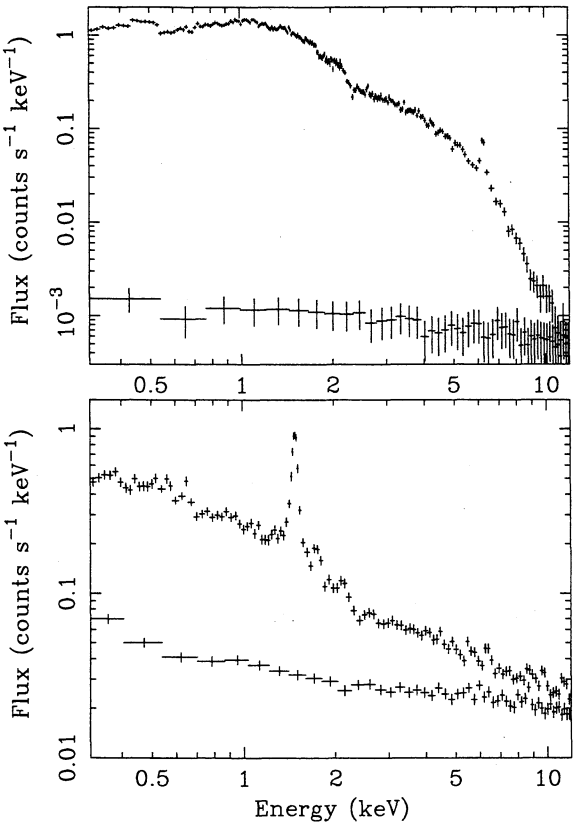

Fig. 9.— Spectra from two annuli from the Abell 1795 analysis, $1' - 2'$ (upper panel) and $10' - 15'$ (lower panel). In each panel the upper spectrum is the total spectrum while the lower spectrum is the modeled QPB spectrum. The data have not been normalized for solid angle, otherwise the $1' - 2'$ spectrum would be relatively brighter by about two orders of magnitude.

4.3. Modeling the Particle Background

The model particle spectra were created using the XMM-ESAS package which follows the process as outlined in § sec:qpb above. Figure 9 displays total and model QPB spectra from an inner and an outer annulus of the Abell 1795 analysis. As expected the fainter outer annulus is much more strongly affected by the various background components, in particular the FX contamination is clearly represented by the Al-Kα line and the residual SP contamination which is responsible for the difference between the spectra above $E \sim 8$ keV.

4.4. Modeling the Cosmic Background

Modeling and constraining the CXB is a two-part process. First, the RASS spectrum of the CXB in the direction of interest can be obtained from the HEASARC "X-ray Background Tool" (see § 3.4.1 above). Since the object of interest in this analysis is a discrete object and not the CXB itself, an annular extraction region should be used where the inner annulus radius is large enough to exclude cluster emission. The outer annulus radius should not be too large so the spectrum is as appropriate as possible for the cluster region. For this analysis of Abell 1795, inner and outer radii of 1° and 2°, respectively, were used.

4.5. The Fitted Spectral Model

The model for the example is rather extensive as it to a great extent represents most of the emission components along the line of sight to and including the Abell 1795 cluster and the local background components. To complicate the process even further, the fitted parameters for some of the components will differ between the different annuli.

$$P_1 + G_1 + G_2 + C_1 \times C_2 \times (A_1 + (A_2 + A_3 + AC \times e^{-\sigma N_{Hc}} + P_2) \times e^{-\sigma N_{Hg}}$$

P_1	Power law representing the residual SP contamination.
G_1, G_2	Gaussians representing the Al Kα and Si Kα FX lines.
C_1, C_2	Constant representing the different solid angles of the extraction annuli and calibration offsets between the two detectors.
A_1	CXB LHB thermal component.
A_2	CXB cooler halo thermal component.
A_3	CXB hotter halo thermal component.
P_2	CXB extragalactic power law component.
N_{Hg}	Column density of Galactic hydrogen.

The equation above is a fairly complete model for the non-cluster component of the observed spectrum in the cluster analysis. P_1 is a power law representing the residual SP contamination. This is not folded through the instrumental effective areas. G_1 and G_2 are Gaussians which represent the Al Kα and Si Kα FX lines. C_1 and C_2 are constant scale factors which represent the different solid angles of the extraction annuli and any relative calibration offsets between the two detectors. For consistency with the RASS data, the C_1 parameter should be set to the the solid angle in units of square arc minutes (in practice, this is the spectrum BACKSCAL keyword value produced by SAS divided by 1440000). The cosmic background is represented by A_1 for the LHB, A_2 for the cooler halo component, A_3 for the hotter halo component, P_2 is the extragalactic power law, and N_{Hg} is the column density of Galactic neutral hydrogen. To model the cluster emission we use a simple absorbed thermal model where the absorption is allowed to vary.

4.6. The Data

For this analysis we have extracted data from 10 annuli for the cluster. These are the same annuli which are used for the rest of the clusters in this catalog. They size of the annuli were chosen to be reasonable, where reasonableness in this, and most cases, is not unique. The dominant constraint is that the number of events in a specified annulus must be sufficient for a significant spectral fit.

4.7. The Fit

The setting up of the spectral fit is a time-consuming process. For the number of spectra (20 MOS1 and MOS2 spectra and 1 RASS spectrum) and the complex model used for the fit, there are 546 parameters. Clearly if all 546 parameters are fit independently convergence of the fit would take place only on geologic time scales. However, many of the parameters can be either linked or frozen to known values, some of which may be later allowed to vary once the fit is relatively accurate. The cosmic background will be the same for all spectra and so the parameters can be linked (the redshifts and abundances of the thermal components can be frozen to 0.0 and 1.0, respectively). The solid angle scale factors should be frozen to their appropriate values and the instrument scale factors should be linked. The normalizations for the SP contributions can be linked using the model distribution available in the XMM-ESAS package and the power law index can be linked. For the cluster contribution to the spectra, the redshift can be linked. In practice, often the abundance parameter should be linked for adjacent annuli to provide sufficient statistics to constrain the fitted values. Table 1 provides suggested initial parameters and whether they should be constrained.

There are further complications to the fitting process. First, because of the finite PSF of the EPIC instruments, some X-rays which originate in one annulus on the sky are detected in a different annulus. In cases where there are strong spectral gradients, e.g., for clusters with a strong cooling flow, this can significantly affect the results with the inner annulus having a higher fitted temperature and the neighboring annuli having cooler fitted temperatures than their true values. In all cases the fitted value for the flux will be higher than the true value. The arfgen task of SAS now has the capability of calculating the "cross-talk" effective area file for X-rays originating in one region but which are detected in another. In the Xspec spectral fitting package, this requires the use of Version 12 or higher. Second, the use of Xspec V12 requires that the SP power law be included as a separate model with a separate response matrix. This response matrix must be diagonal with unity elements.

4.8. Abell 1795 Results

Figure 10 shows the final Xspec V12 fit to the 21 Abell 1795 spectra in all of its glory. The fit has a final χ^2 value of 4913 with 3943 degrees of freedom for a χ^2_ν value of 1.25. The fit is generally good with only relatively minor deviations between 0.3 and 12.0 keV.

Figure 11 shows the comparison between the Vikhlinin et al. (2005) *Chandra*, Nevalainen, Markevitch, & Lumb (2005) *XMM-Newton* and current analysis of Abell 1795. As expected, there is reasonable agreement between the *XMM-Newton* results. However, the *Chandra* results are very significantly different from those of *XMM-Newton*. This discrepancy is consistent for the higher temperature clusters which have been compared. The sense of the difference is that the higher the fitted temperature the more likely it

TABLE 1
SPECTRAL FIT PARAMETERS.

Spectral Component	Model Component	Parameter	Initial Guess	Initial Constraint	Final Constraint
SP	P_1	α_1	0.9	Fix	Free
–	–	Normalization	10^{-5}	Free	Free
FX	G_1	Energy	1.49 keV	Fix	Free
–	–	Width	0.0 keV	Fix	Free
–	–	Normalization	10^{-5}	Free	Free
FX	G_2	Energy	1.75 keV	Fix	Free
–	–	Width	0.0 keV	Fix	Free
–	–	Normalization	10^{-5}	Free	Free
Scale	C_1	Solid Angle	Set	Fix	Fix
Scale	C_2	Scale Factor	1.0	Fix	Free
CXB[a]	A_1	kT	0.1	Fix	Free
–	–	Normalization	5.0×10^{-6}	Free	Free
–	A_2	kT	0.1	Fix	Free
–	–	Normalization	5.0×10^{-6}	Free	Free
–	A_3	kT	0.25	Fix	Free
–	–	Normalization	10^{-6}	Free	Free
–	P	α	1.46	Fix	Fix
–	–	Normalization	8.88×10^{-7}	Fix	Free
–	N_{Hg}	Galactic Column	1.2×10^{20}	Fix	Free
A1795	A_4	kT	5.0 keV	Free	Free
–	–	Abundance	0.5	Free	Free
–	–	Redshift	0.06	Free	Free
–	–	Normalization	5.0×10^{-4}	Free	Free
–	N_{Hc}	Cluster Column	1.2×10^{20}	Fix	Free

[a]The abundances and redshifts of the cosmic thermal components are fixed at 1.0 and 0.0, respectively.

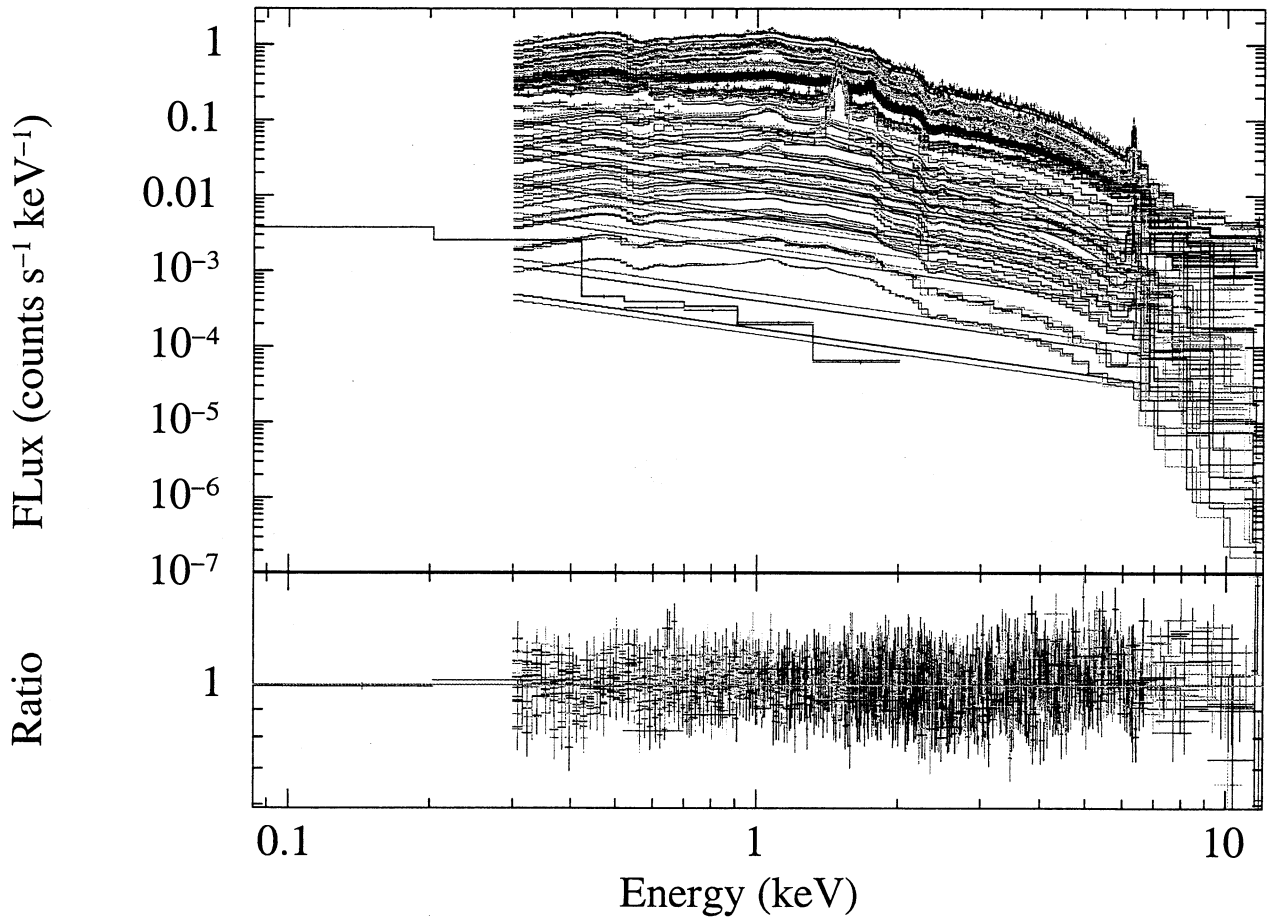

Fig. 10.— Spectral fit to the data from Abell 1795.

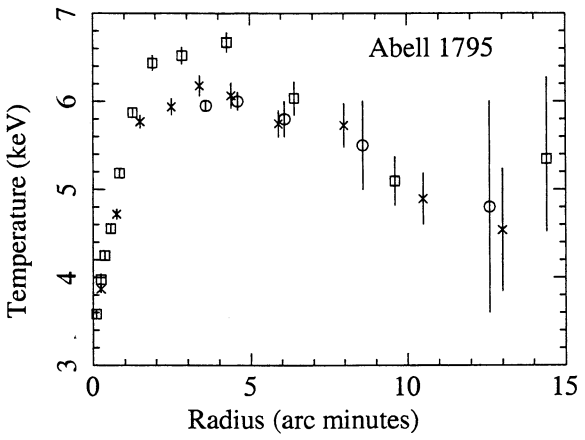

Fig. 11.— Comparison of results for the A1795 temperature radial profile from *Chandra* (square, Vikhlinin et al. (2005)), and *XMM-Newton* analysis (circle, Nevalainen, Markevitch, & Lumb (2005); cross, this analysis). The radii for the *XMM-Newton* points have been slightly offset in the plot for clarity.

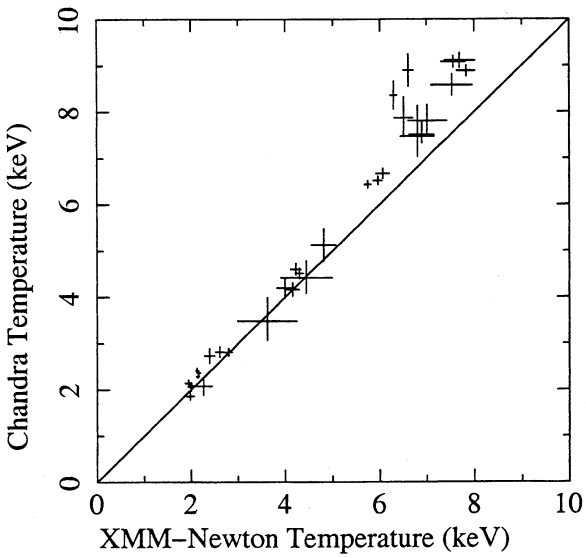

Fig. 12.— Comparison of results for the temperature radial profiles for various clusters in their $\sim 1' - 5'$ annuli from *Chandra* (Vikhlinin et al. (2005)) and *XMM-Newton* (this analysis).

is that *Chandra* will find a higher temperature than *XMM-Newton* with the effect typically becoming significant above $\sim 5 - 6$ keV. Figure 12 displays this difference in the fitted temperatures for clusters in their $\sim 1' - 5'$ annuli (*Chandra* data from Vikhlinin et al. (2005)). This discrepancy is currently being studied by both projects.

One suggested explanation for the discrepancy was the effect of the finite PSF of *XMM-Newton* and the spreading of the cooler X-rays from the cluster core to the inner annuli. Indeed, this is what led to the development of the arfgen modification to account for the cross-talk. While the correction effect does go in the right direction (Figure 13 top panel), for Abell 1795 it is barely significant and not nearly sufficient to account for the difference. Also, use of the *Chandra* image with its finer PSF for the calculation of the cross-talk contribution has no significant effect. However, the effect can be significant in cases where the flux and temperature gradients is steeper (on an angular scale) and greater in magnitude. Figure 13 (bottom panel) shows a similar comparison for the cluster Abell 2204. In this case the fitted temperature of the second annuli increases by ~ 1.5 keV when the correction for PSF smearing is applied.

5. The Cluster Catalog

We applied the method described above for the Abell 1795 data to process in a consistent manner 70 clusters of galaxies from the *XMM-Newton* archive. The selection of the clusters was empirical, postage-stamp count images from the *ROSAT* All-Sky Survey were examined for each of the *XMM-Newton* cluster observations. Those which appeared to have (subjectively) reasonable extent and reasonable brightness were chosen for processing. A total of just over 100 clusters were selected.

The initial step of the processing was to filter the data to exclude periods of SP flaring and to create count images. Clusters where the accepted exposure time was less than ~ 8 ks as well as clusters with a surface brightness insufficient to produce reasonable statistic were excluded from further analysis. The selection against overly contaminated observations excluded $\sim$ 30 clusters. For those observations with filtered times acceptable for processing, roughly 25% of of the original processing time was lost to flaring. (This loss does not include the useless exposures of observations with multiple exposures.) A few other clusters were excluded from the processing because of their extreme asymmetry or the presence of strong

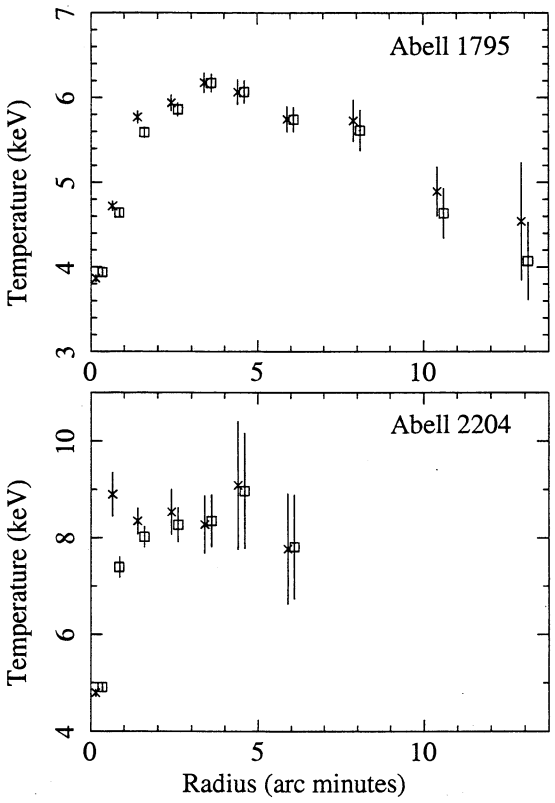

Fig. 13.— Comparison of results for the Abell 1795 (top panel) and Abell 2204 (bottom panel) temperature radial profiles from analysis including (cross) and not including (square) the effect of PSF smearing (crosstalk between adjacent annuli). The radii have been slightly offset in the plot for clarity.

substructures.

For the accepted observations, the center of the cluster was determined from an image, bright point sources were excluded, and the data were processed to produce spectra for the ten annuli listed in Table 2 for both MOS detectors. The count images in the $0.2 - 1.0$ keV band were examined for evidence of the individual CCDs operating in an anomalous state. If so, the individual CCD was excluded from the spectral extraction. The HEASARC X-ray Background Tool was used to create RASS spectra in, typically, a $1 - 2$ degree annulus around the cluster. For a few cases (e.g., the Coma and Virgo clusters) the annulus had to be increased in size to exclude the cluster. The X-ray Background Tool also provides the column density of Galactic H I which was fixed in the spectral fits. The analyzed clusters are listed in Table 3. Included in the table are the fitted X-ray redshifts, *XMM-Newton* observation identification (ObsID), accepted and initial exposures, and the surface brightness limits for the image color bar scalings.

In order to test the reliability of our analysis methods we used a second observation of the cluster Abell 1835 for comparison. Figure 14 plots the fitted temperatures which are in very good agreement. We had hoped to do similar comparisons with other clusters but no other cases where there were multiple observations of a single cluster had sufficient acceptable (uncontaminated data) or the pointing directions of the observations were too far apart.

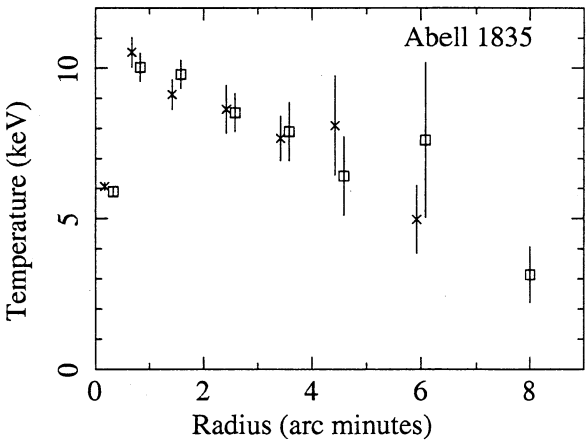

Fig. 14.— Comparison of temperature radial profile results for the two observations of Abell 1835.

The temperature, abundance, and flux radial profiles for the 70 clusters listed in Table 3 are shown in Figures 18 through 35 in the Appendix. We also include soft ($0.35 - 1.25$ keV) and hard ($2.0 - 8.0$ keV) band images of the clusters in the Appendix (Figures 18 through 35). The images combine the MOS1 and MOS2 data and are background subtracted (QPB and SP), exposure corrected, and adaptively smoothed. Table 3 provides the upper scaling limits for the color coding (purple and blue indicate low intensity while red and white indicate high intensity), all images have lower limits of zero, and all images are logarithmically scaled. Units are counts s^{-1} deg^{-2} where

TABLE 2
ANNULI DEFINITIONS.

Annulus	Inner Radius	Outer Radius
1	$0'$	$0.5'$
3	$0.5'$	$1'$
3	$1'$	$2'$
4	$2'$	$3'$
5	$3'$	$4'$
6	$4'$	$5'$
7	$5'$	$7'$
8	$7'$	$9'$
9	$9'$	$12'$
10	$12'$	$14'$

NOTE.—Inner and outer radii in arc minutes of the annuli used in the analysis of the clusters presented here.

the typical level of the cosmic background is ~ 1 in these units. The intensities are average values of what the detectors observe rather than the sum.

6. Results and Conclusions

In this paper we have outlined a robust and reliable method for analyzing extended X-ray sources observed with the *XMM-Newton* EPIC MOS detectors. The method combines screening of the data for periods of background enhancements (most notably the soft proton contamination), detailed modeling of the particle background spectrum, and the determination of other background components in the spectral fitting process (residual SP contamination, fluorescent particle background lines, and the cosmic background).

We have demonstrated our method with the bulk processing of the observation of 70 clusters of galaxies. Comparison of the results for two separate observations of Abell 1835 show very good agreement between their fitted parameters. However, comparison of our results with the *Chandra* results of Vikhlinin et al. (2005) for the overlapping subset of clusters shows a significant discrepancy for higher temperature clusters. The sense of this discrepancy is that the higher the fitted temperature, the greater the likelihood that *Chandra* will find a higher temperature and *XMM-Newton*. The differences can be over 1 keV at $7-8$ keV.

While the detailed scientific analysis and discussion of these results are deferred to Paper II, a few aspects are clear from plots of the entire data set. For the combined plots, the radii of the annuli have been scaled to the R_{500} value of the cluster as derived from the equation $R_{500} = 2.6 \times ((1.0+z)^{\frac{-3}{2}} \times (T/10.0)^{\frac{1}{2}}$ (Evrard, Metzler, & Navarro 1996) where z is the fitted value for the cluster redshift and T is the average fitted value for the cluster temperature in the $1'-4'$ annulus. Figures 15, 16, and 17 show the cumulative plots for the temperature, abundance, and flux, respectively. Both the temperature and flux have been normalized to the values in the range 5% - 30% of R_{500}. In addition, only points where the fitted values are three times the fitted uncertainty are plotted.

Inspection of Figure 15 shows, as seen before (e.g. Pratt et al. (2007), Arnaud, Pointecouteau, & Pratt (2005), Vikhlinin et al. (2006)) a wide variety of temperature profiles inside 5% of R(500).

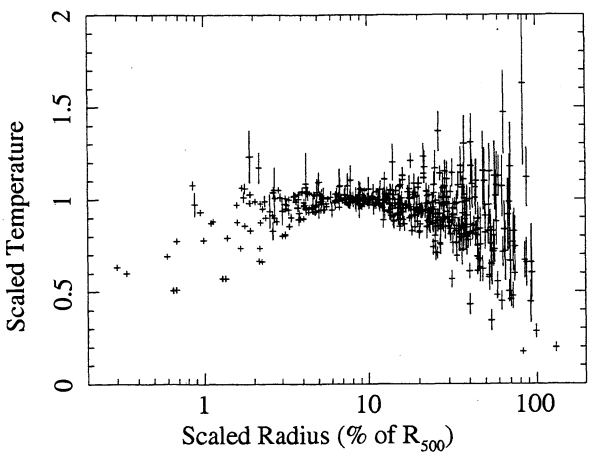

Fig. 15.— Scaled temperature radial profiles for all of the analyzed clusters.

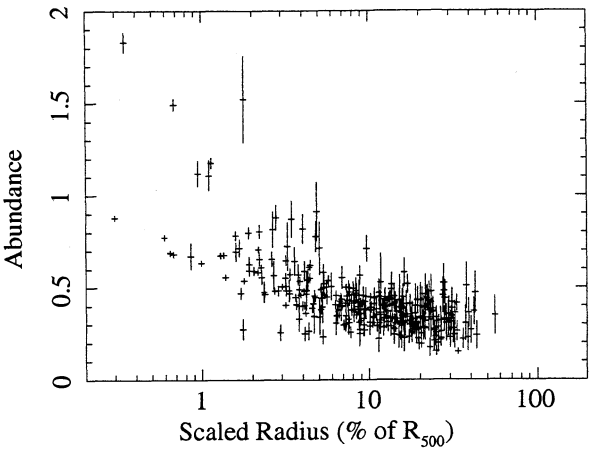

Fig. 16.— Abundance radial profiles for all of the analyzed clusters.

Most of these can be characterized by a temperature drop in the center.. (Richard, you have more to say here?) Over the range from $0.05 - 0.2R_{500}$ the clusters are isothermal to better than 5%. Beyond $\sim 0.2R_{500}$ a significant fraction of the clusters (Paper II) show temperature drops, but they are not all self-similar. However a significant fraction of the clusters are isothermal out to the largest radii measurable.

As noted by Arnaud, Pointecouteau, & Pratt (2005), many of the clusters show a self-similar surface brightness profile (Figure 17). Outside of $\sim 0.03R_{500}$ there is significant scatter in the profile. With respect to the overall abundance, as was noted for *ASCA* spectra of clusters by f (199x) and later for many *XMM-Newton* and *Chandra* spectra (Maugham et al. 2007) there is in a significant fraction of the clusters an abundance increase in the center. However outside of the central $\sim 0.05R_{500}$ there is no evidence for an abundance gradient and all the clusters are very close to the average value of $A = 0.3$ on the Anders & Grevesse (1989) abundance scale (Figure 16). Detailed analysis of these results will appear in Paper II.

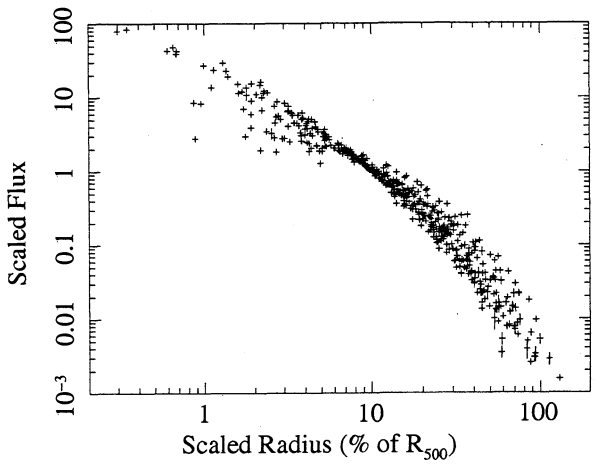

Fig. 17.— Scaled flux radial profiles for all of the analyzed clusters.

REFERENCES

Allen, S. W., Schmidt, R. W. & Fabian, A. C. 2001, MNRAS, 328, L37

Anders E. & Grevesse N. 1989, Geochimica et Cosmochimica Acta, 53, 197

Arnaud, M., Neumann, D. M., Aghanim, N., Gastaud, R., Majerowicz, S., & Hughes, J. P. 2001, A&A, 365, L80

Arnaud, M., et al. 2002, A&A, 390, 27

Arnaud, M., Pointecouteau, E. & Pratt, G. W. 2005, A&A, 441, 893

Bahcall, N. A. 1997, ARA&A, 15, 1505

De Grandi, S. & Molendi, S. 2001, ApJ, 567, 163

de Grandi, S., Bhringer, H., Guzzo, L., Molendi, S., Chincarini, G., Collins, C., Cruddace, R., Neumann, D., Schindler, S., Schuecker, P., & Voges, W. 1999, ApJ, 514, 148

De Luca, A. & Molendi, S. 2004 A&A, 419, 837

Ehle, M., et al. 2005, *XMM-Newton* Users' Handbook (Madrid:ESA)

Evrard, S. 2003, Carnegie Observatories Astrophysics Series, Vol. 3, Clusters of Galaxies: Probes of Cosmological Structure and Galaxy Evolution , ed. J. S. Mulchaey, A. Dressler, and A. Oemler (Cambridge:Cambridge Univ. Press)

Evrard, A. E., Metzler, C. A., & Navarro, J. F. 1996, ApJ, 469, 494

Fabricant, D. & Gorenstein, P. 1983, ApJ, 267, 535

Fabricant, D., Lecar, M., & Gorenstein, P. 1980, ApJ, 241, 552

Finoguenov, A., Arnaud, M. & David, L. P. 2001, ApJ, 555, 191

f

Gorenstein, P., Bjorkholm, P., Harris, B., & Harnden, F. R., Jr. 1973, ApJ, 183, 57

Hashimoto, Y., Barcons, X., Böhringer, H., Fabian, A. C., Hasinger, G., Mainieri, V., & Brunner, H. 2004, A&A, 417, 819

Hickox, R. C. & Markevitch, M. 2007, in press

Hughes, J. P., Gorenstein, P., & Fabricant, D. 1988, ApJ, 329, 82

Irwin, J. A., Bregman, J. N. & Evrard, A. E. 1999, ApJ, 519, 518

Irwin, J. A., & Bregman, J. N. 2000, ApJ, 538, 543

Jones, C., & Forman, W. 1978, ApJ, 224, 1

Jones, C., & Forman, W. 1984, ApJ, 276, 38

Kaastra, J. S., Tamura, T., Peterson, J. R., Bleeker, J. A. M., Ferrigno, C., Kahn, S. M., Paerels, F. B. S., Piffaretti, R., Branduardi-Raymont, G. & Böhringer, H. 2004, A&A, 413, 415

Kay, S. T., Thomas, P. A., Jenkins, A., & Pearce, F. R. 2004, MNRAS, 355, 1091

Kikuchi, K., Furusho, T., Ezawa, H., Yamasaki, N. Y., Ohashi, T., Fukazawa, Y., & Ikebe, Y. 1999, PASJ, 51, 301

Komatsu & Seljak 2001, MNRAS, 327, 1353

Kuntz, K., & Snowden, S. L. 2000, ApJ, 543, 195

Kuntz, K. D., & Snowden, S. L. 2001, ApJ, 554, 684

Kuntz, K. D., & Snowden, S. L. 2007, A&A, submitted

Kuntz, K. D., Snowden, S. L., & Mushotzky, R. F. 2001, ApJ, 548, 11

Lallement, R. 2004, A&A, 418, 143

Loken, C., Norman, M. L., Nelson, E., Burns, J., Bryan, G. L., & Motl, P. 2002, ApJ, 579, 571

Majerowicz, S., Neumann, D. M., & Reiprich, T. H. 2002, A&A, 394, 77

Markevitch, M., Forman, W. R., Sarazin, C. L., & Vikhlinin, A. 1998, ApJ, 503, 77

Maughan, B. J., Jones, C., Forman, W., & Van Speybroeck, L. 2007, in press

McCammon, D., et al. 2002, ApJ, 576, 188

Mushotzky, R. F., Serlemitsos, P. J., Boldt, E. A., Holt, S. S., & Smith, B. W. 1978, 1978, ApJ, 225, 21

Mushotzky, R. 2002, in The Century of Space Science (Klewer:The Netherlands), 473

Navarro, J. F., Frenk, C. S., & White, S. D. M. 1997, ApJ, 490, 493

Nevalainen, J., Markevitch, M.,& Lumb, D. 2005, ApJ, 629, 172

Piffaretti, R., Jetzer, Ph., Kaastra, J. S. & Tamura, T. 2005, A&A, 433, 101

Pratt, G. W. & Arnaud, M. 2002, A&A, 394, 375

Pratt, G. W., Bhringer, H., Croston, J. H., Arnaud, M., Borgani, S., Finoguenov, A., & Temple, R. F. 2007, A&A,461, 71

Rasia, E., Ettori, S., Moscardini, L., Mazzotta, P., Borgani, S., Dolag, K., Tormen, G., Cheng, L. M. & Diaferio, A. 2006, MNRAS, 369, 2013

Read, A., & Ponman, T. 2003, å, 409, 395

Robertson, I. P., & Cravens, T. E. 2003, Geophys. Res. Lett., 30(8), 1439

Sfeir, D. M., Lallement, R., Crifo, F., & Welsh, B. Y. 1999, A&A, 346, 785

Snowden, S. L., Collier, M. R., & Kuntz, K. D. 2004, ApJ, 610, 1182

Snowden, S. L., & Kuntz, K. D. Snowden, S. L. 2006, *XMM-Newton* GOF

Snowden, S. L., Egger, R., Freyberg, M. J., McCammon, D., Plucinsky, P. P., Sanders, W. T., Schmitt, J. H. M. M., Trümper, J., & Voges, W. 1997, ApJ, 485, 125

Snowden, S. L., Egger, R., Finkbeiner, D. P., Freyberg, M. J., & Plucinsky, P. P. 1998, ApJ, 493, 715

Tozzi, P. et al. 2006, A&A, 451, 457

Vikhlinin, A., Markevitch, M., Murray, S. S., Jones, C., Forman, W., & Van Speybroeck, L. 2005, ApJ, 628, 655

Vikhlinin, A., Kravtsov, A., Forman, W., Jones, C., Markevitch, M., Murray, S. S., & Van Speybroeck, L. 2006 ApJ, 640, 691

Wargelin, B. J., Markevitch, M., Juda, M., Kharchenko, V., Edgar, R. J., & Dalgarno, A. 2004, ApJ, submitted

White, D. A. 2000, MNRAS, 312, 663

White, D. A. & Buote, D. A. 2000, MNRAS, 312, 649

This 2-column preprint was prepared with the AAS LaTeX macros v5.2.

TABLE 3
CLUSTERS.

Cluster	Redshift	ObsID	Filtered Exposure (s)	Original Exposure (s)	0.35-1.25 keV Band Scaling (cnts s^{-2} deg^{-2})	2.0-8.0 keV Band Scaling (cnts s^{-2} deg^{-2})	χ^2_ν	ν
2A 0335+096	0.0329	147800201	74890.7	95962.0	4500	1700	1.48	5002
A68	0.2481	84230201	23818.7	29567.6	350	200	1.25	704
A85	0.0520	65140101	12012.2	12524.4	5000	1800	2.02	1836
A133	0.0575	144310101	19042.1	33670.5	2800	700	1.17	1306
A209	0.2116	84230301	16847.6	21796.1	400	290	0.99	643
A262	0.0140	109980101	22256.9	23897.0	1900	200	1.26	2067
A383	0.1874	84230501	25444.9	33379.3	3000	1000	1.08	942
A399	0.0644	112260101	10807.6	14297.6	200	200	1.03	809
A426	0.0147	85110101	47272.9	53646.5	10000	6000	2.48	8982
A478	0.0808	109880101	49696.1	56249.2	3500	4000	1.27	4913
A496	0.0293	135120201	15845.2	29448.0	3500	1400	1.19	2625
A520	0.1946	201510101	27227.4	46371.6	200	150	1.15	1140
A576	0.0420	205070301	8752.0	21671.3	300	140	1.04	528
A665	0.1788	109890501	49696.9	78487.2	500	300	1.21	2117
A773	0.2161	84230601	12332.1	15082.8	350	300	1.28	464
A1060	0.0131	206230101	32724.8	63773.6	400	200	1.24	3165
A1068	0.1471	147630101	19188.9	29669.0	1000	400	1.03	852
A1413	0.1349	112230501	23397.2	25922.4	1000	500	1.09	1311
A1589	0.0722	149900301	15121.6	17170.7	150	50	1.19	550
A1650	0.0812	93200101	34006.0	42534.0	1200	800	1.10	2470
A1689	0.1809	93030101	34530.0	39169.6	2700	1900	1.17	2031
A1775	0.0754	108460101	22065.8	32003.9	500	200	1.18	1042
A1795	0.0614	97820101	35144.6	50011.7	5000	2000	1.25	3958
A1835	0.2490	98010101	24849.0	40635.5	4000	2000	1.12	1301
A1835a	0.2454	147330201	27895.1	83817.3	4000	2000	1.17	1465
A1837	0.0663	109910101	46233.9	49031.5	500	200	1.14	1529
A1914	0.1735	112230201	19219.6	25571.4	1000	700	1.15	1334
A1991	0.0642	145020101	22620.9	41790.5	2000	500	1.33	1184
A2029	0.0728	111270201	11088.8	17846.7	4000	3000	1.18	2195
A2052	0.0333	109920101	28743.7	30397.0	4000	1000	1.37	2759
A2065	0.0728	202080201	19205.3	33870.7	800	500	1.09	1444
A2163	0.2021	112230601	10177.1	15766.7	400	550	1.16	760
A2199	0.0277	8030201	14190.8	20051.5	2500	1000	1.24	2745
A2204	0.1512	112230301	18367.1	22097.7	4000	3000	1.30	1687
A2218	0.1723	112980101	17673.1	18169.1	300	200	1.30	709
A2256	0.0530	141380201	10233.8	18369.3	300	200	1.24	987
A2319	0.0519	302150101	15145.8	16668.9	650	650	2.51	2672
A2589	0.0417	204180101	22934.0	46670.6	400	200	1.10	1574
A2597	0.0804	147330101	46726.9	104451.1	5000	2000	1.13	2388

TABLE 3—*Continued*

Cluster	Redshift	ObsID	Filtered Exposure (s)	Original Exposure (s)	0.35-1.25 keV Band Scaling (cnts s^{-2} deg^{-2})	2.0-8.0 keV Band Scaling (cnts s^{-2} deg^{-2})	χ^2_ν	ν
A2626	0.0549	148310101	38306.4	41119.6	1000	400	1.11	1746
A2667	0.2205	148990101	17682.8	30914.4	3500	1500	1.21	863
A2717	0.0510	145020201	47414.8	54010.5	500	100	1.20	1668
A3112	0.0723	105660101	22271.5	23247.0	6000	2500	1.24	1919
A3158	0.0609	300210201	19076.9	22149.7	400	300	1.37	1755
A3526	0.0054	46340101	43699.3	47182.9	5000	1000	2.32	5031
A3558	0.0459	107260101	40643.4	44026.4	600	400	1.23	3601
A3560	0.0429	205450201	27009.7	45271.8	150	70	1.10	1261
A3581	0.0225	205990101	33930.6	43670.2	2400	500	1.40	2206
A3827	0.0959	149670101	21024.9	24970.8	500	400	1.23	1437
A3888	0.1537	201903101	23250.1	30469.8	500	400	1.08	1564
A3911	0.0958	149670301	22883.3	27269.2	200	150	1.02	1236
A3921	0.0919	112240101	28488.8	30763.6	400	300	1.10	1467
A4059	0.0467	109950201	22581.2	24398.8	1200	400	1.18	1952
AS 1101	0.0564	123900101	30530.1	60996.9	4000	1100	1.14	1982
AWM 7	0.0155	135950301	30530.1	60996.9	1000	500	1.35	3793
Coma	0.0218	124711401	16195.8	23598.0	500	300	1.15	3692
E1455+2232	0.2583	108670201	33785.9	39993.7	1600	1800	1.25	1100
EXO0422	0.0336	300210401	38373.1	41070.2	3000	1500	1.26	2402
Hydra	0.0521	109980301	17944.5	31546.3	4000	2000	1.29	2180
Klemola 44	0.0286	204460101	29668.9	29669.0	1200	500	1.28	2757
M87	0.0042	114120101	35931.1	39551.8	15000	3000	3.71	5401
MKW 3S	0.0417	109930101	33244.3	51038.7	1900	800	1.24	2699
MKW 4	0.0214	93060101	13585.2	15368.8	1000	200	1.26	673
Perseus	0.0148	305780101	101982.0	124869.2	15000	15000	3.63	10095
PKS 0745-19	0.0986	105870101	18043.2	26946.8	3000	5000	1.24	1872
RXCJ0605.8-3518	0.1367	201901001	17798.1	26668.6	3000	1500	1.30	904
RXJ0658-55	0.3069	112980201	21464.2	42770.6	600	400	1.22	961
RXJ1347-1145	0.4477	112960101	30122.7	38121.7	4000	3000	1.29	1290
Sersic 159-3	0.0563	147800101	81339.4	122209.4	3500	1000	1.51	3488
Triangulum	0.0478	93620101	9168.9	14497.8	500	600	1.02	1890
ZW3146	0.2817	108670101	51450.6	53597.1	4000	2000	1.36	1802

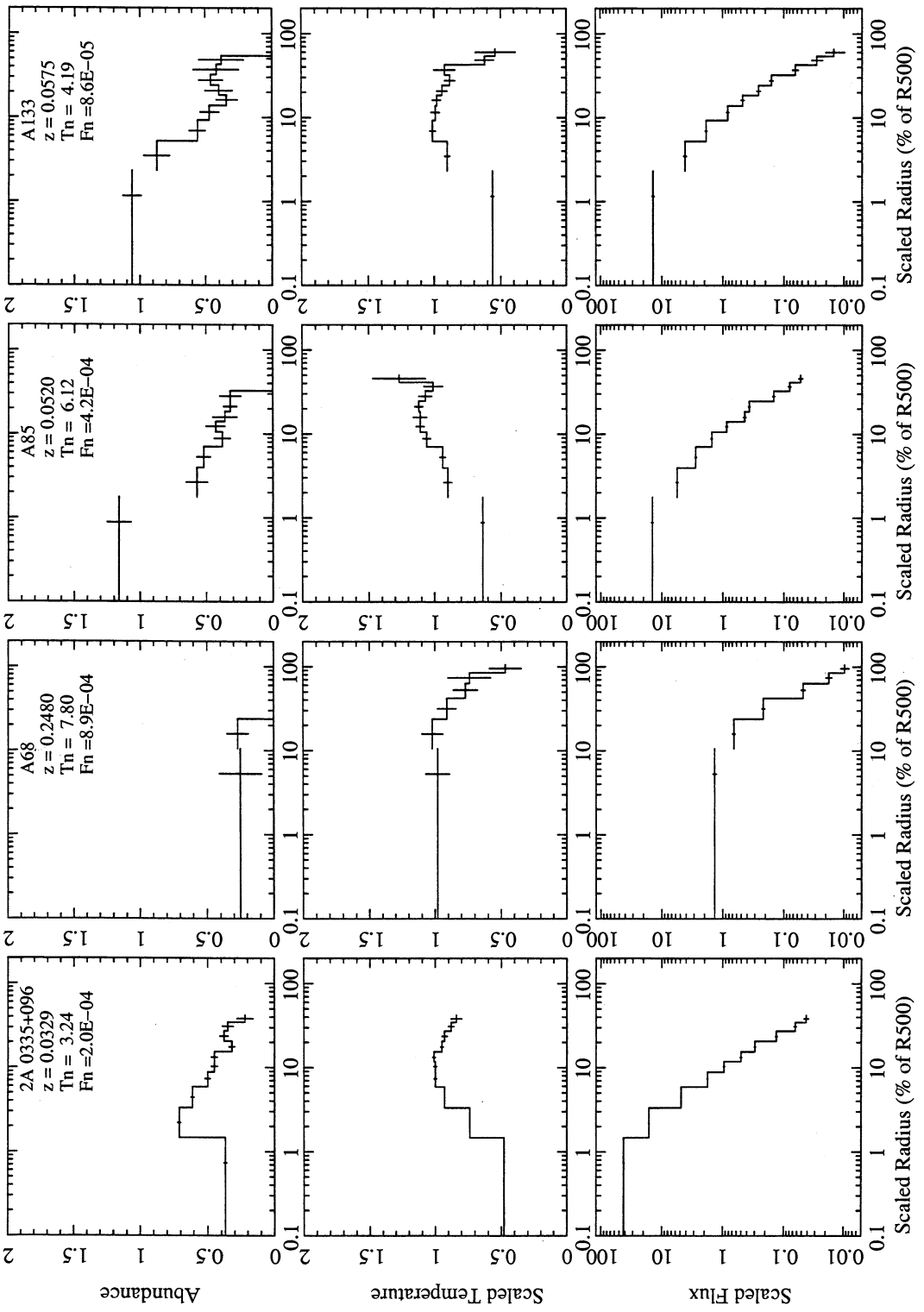

Fig. 18.— Cluster temperature, abundance, and flux radial profiles.

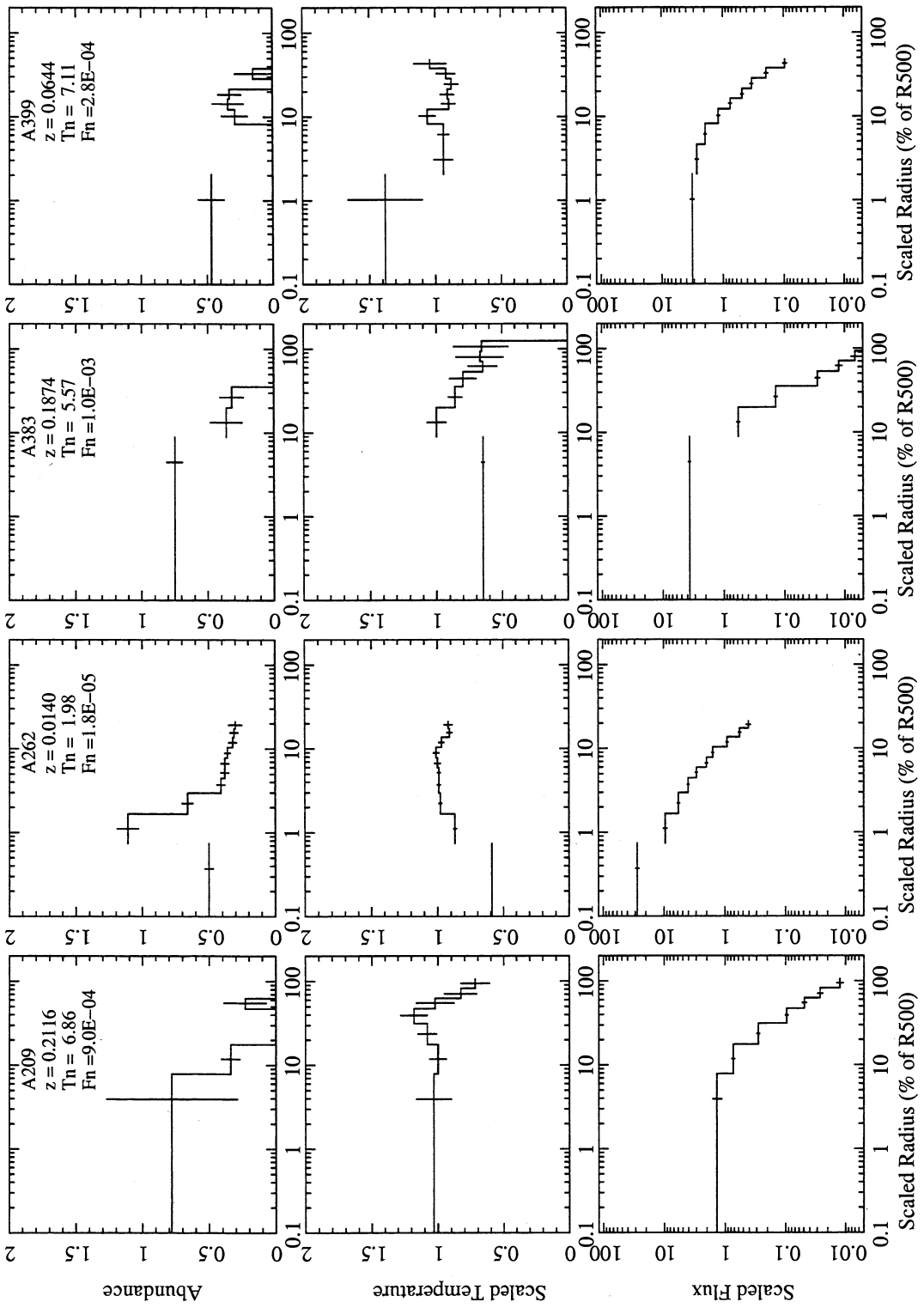

Fig. 19.— Cluster temperature, abundance, and flux radial profiles.

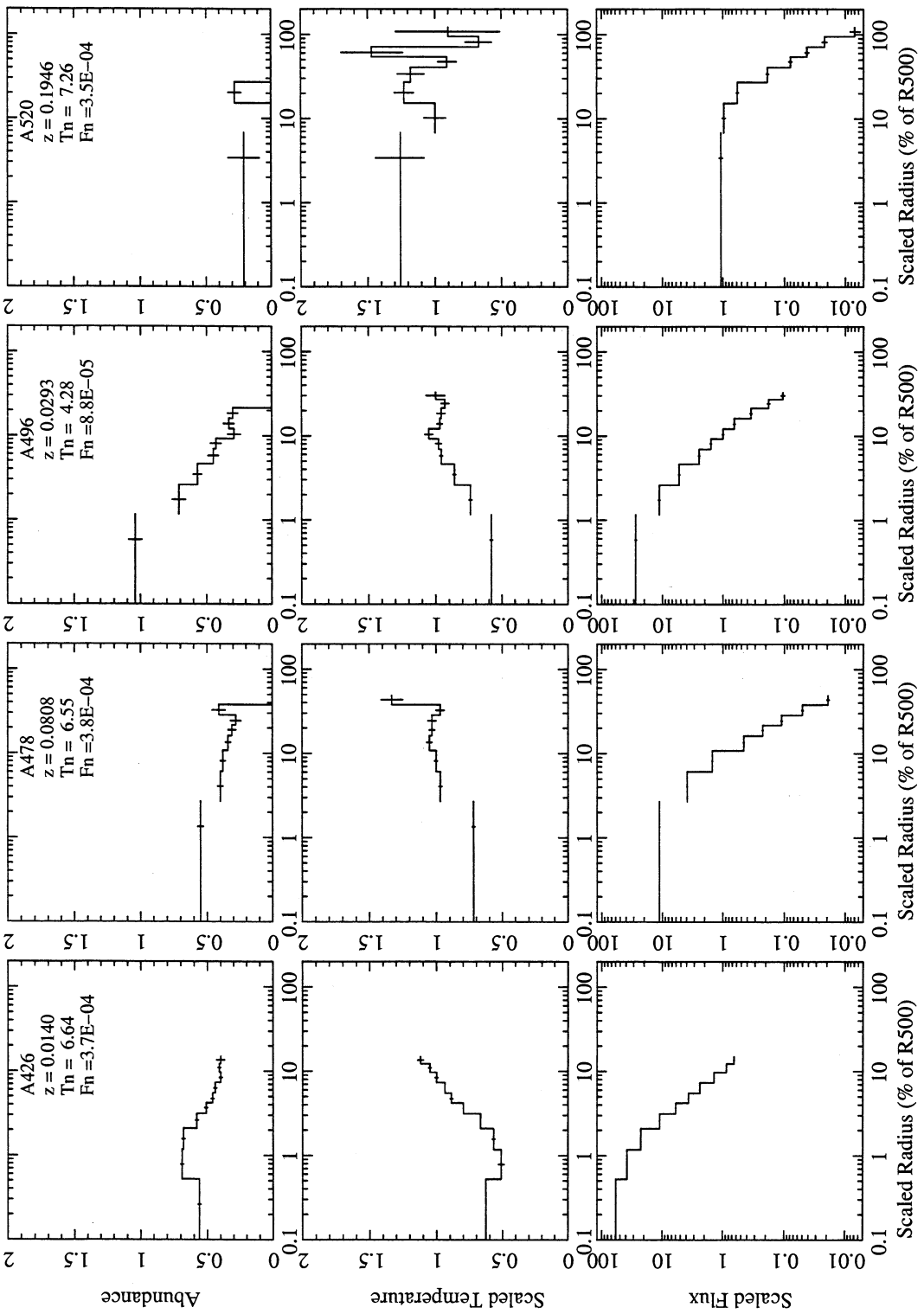

Fig. 20.— Cluster temperature, abundance, and flux radial profiles.

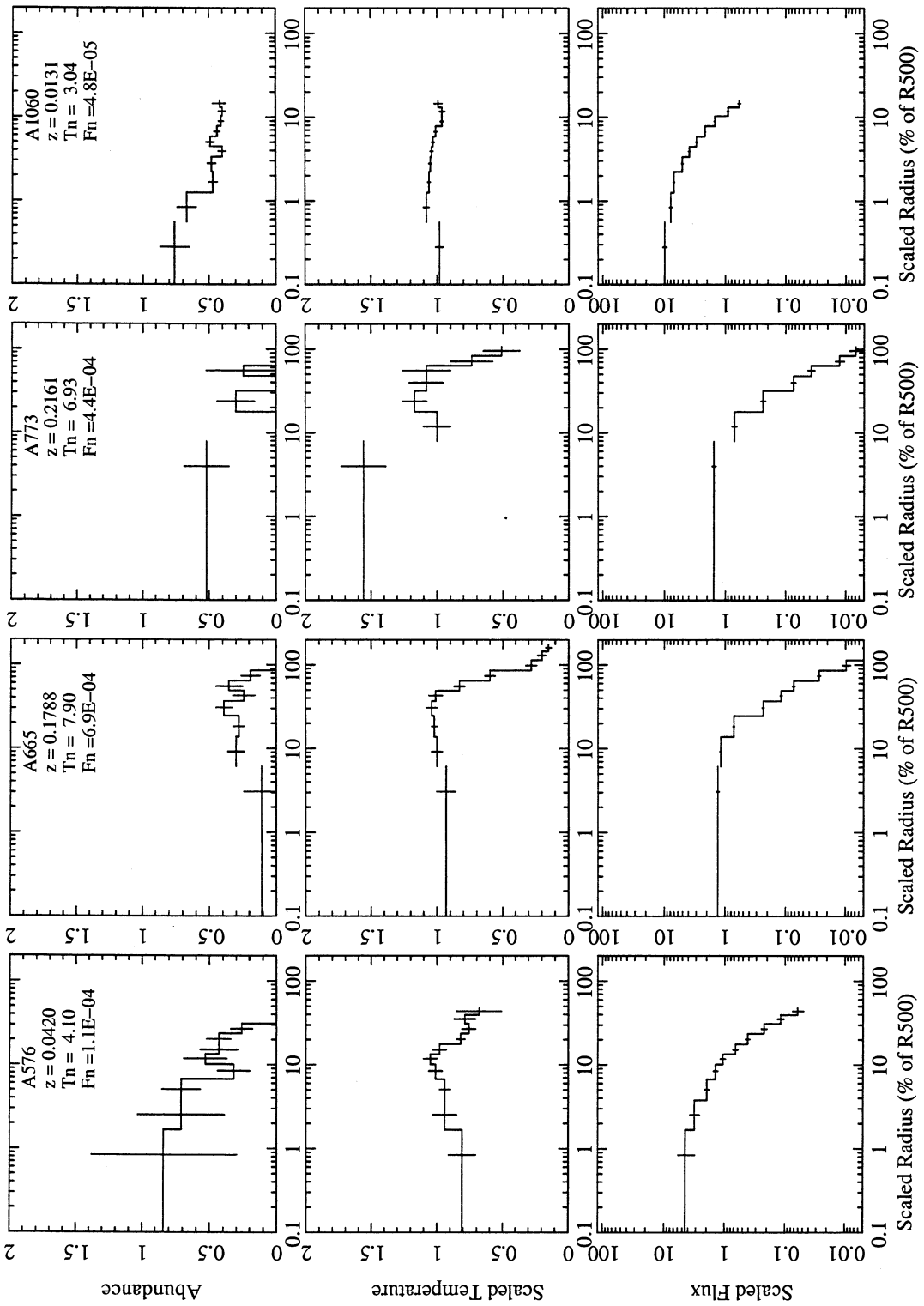

Fig. 21.— Cluster temperature, abundance, and flux radial profiles.

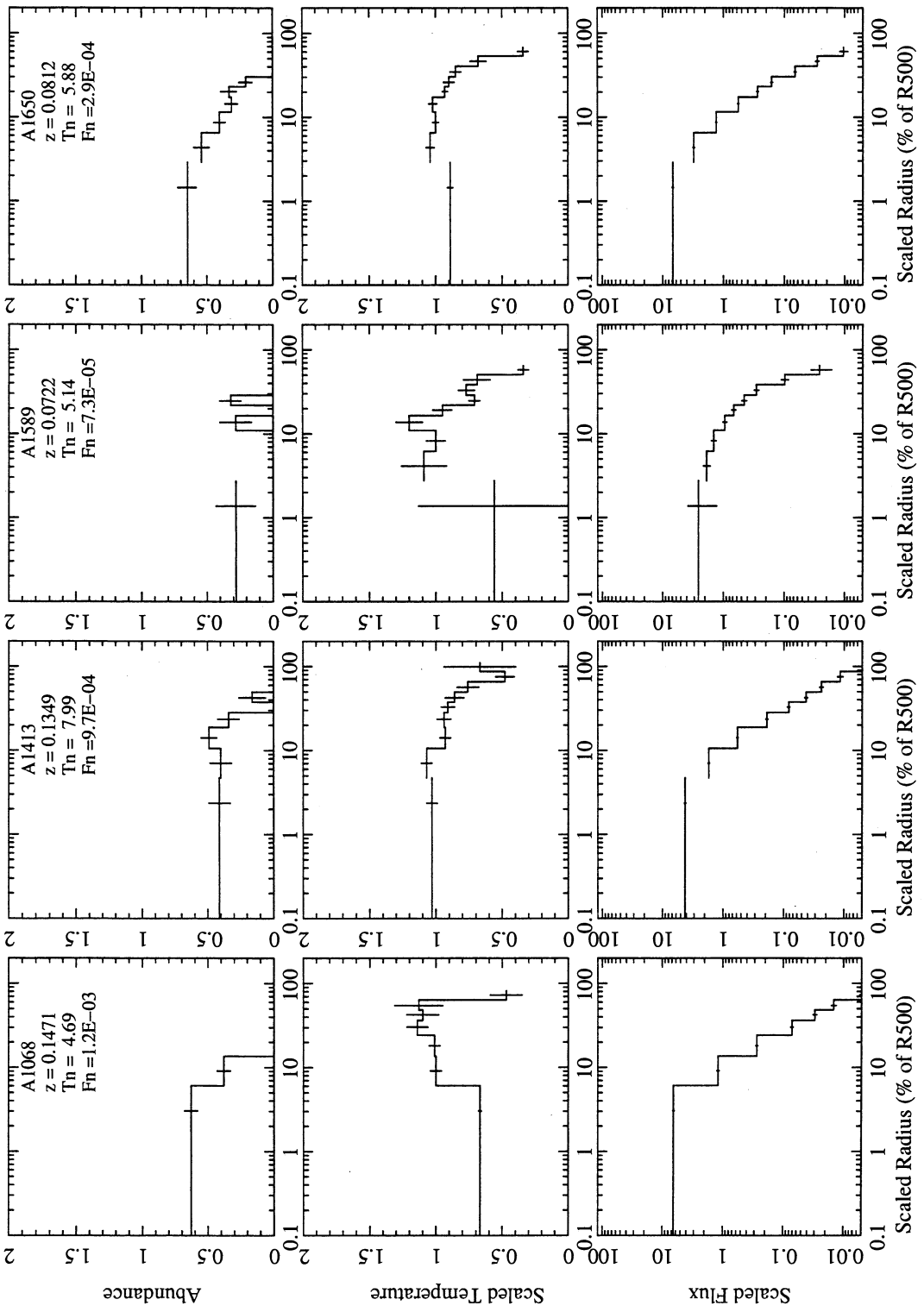

Fig. 22.— Cluster temperature, abundance, and flux radial profiles.

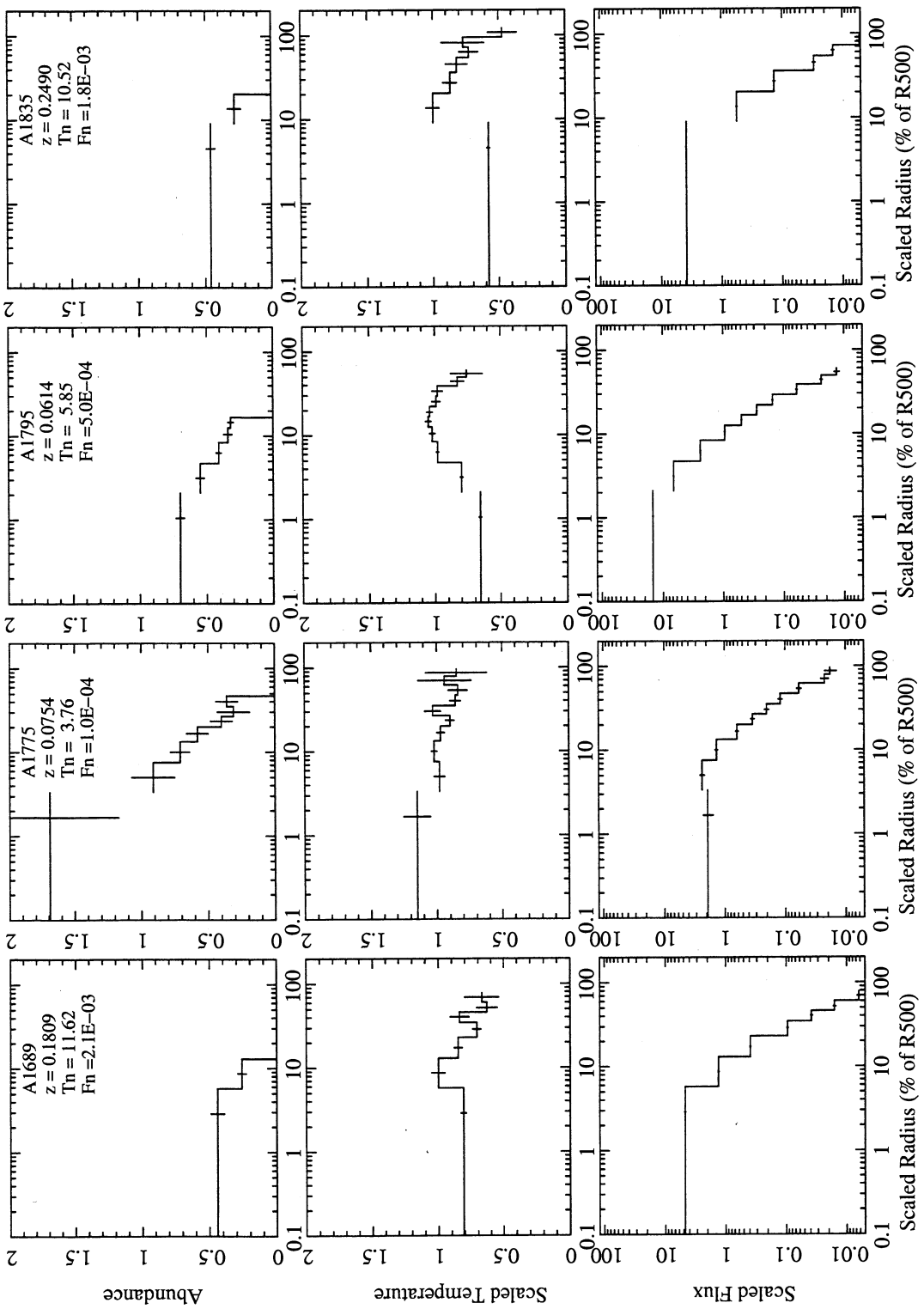

Fig. 23.— Cluster temperature, abundance, and flux radial profiles.

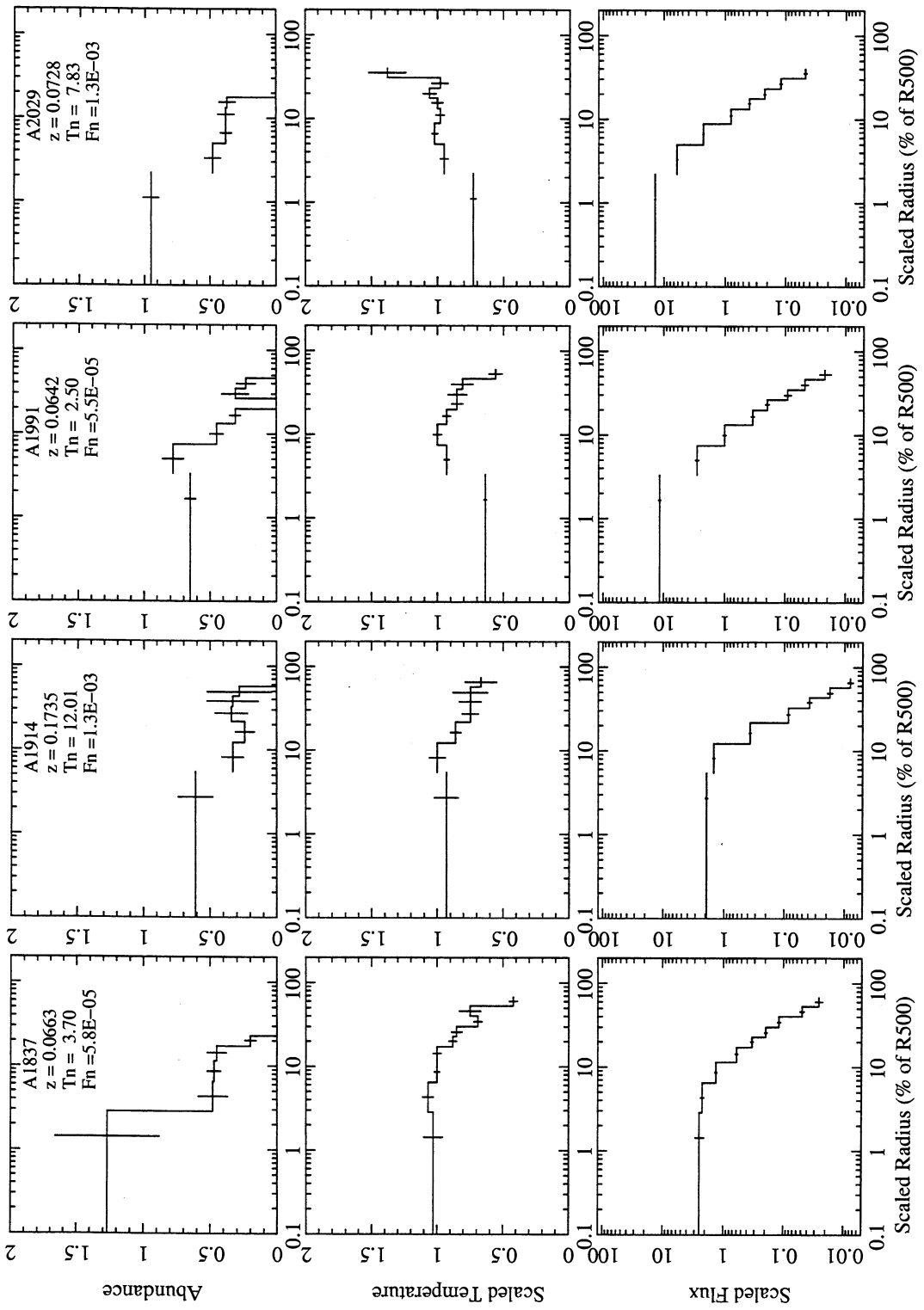

Fig. 24.— Cluster temperature, abundance, and flux radial profiles.

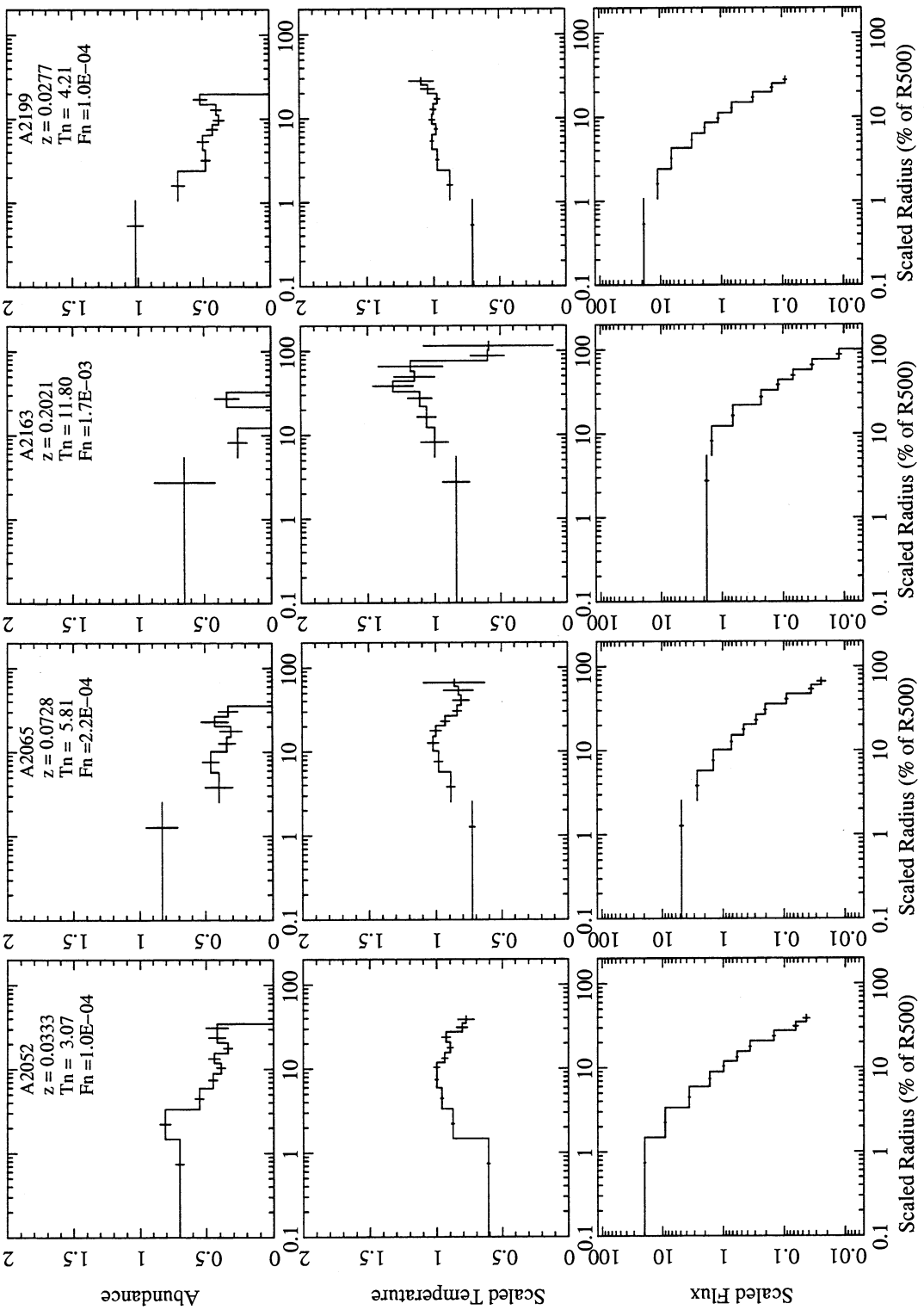

Fig. 25.— Cluster temperature, abundance, and flux radial profiles.

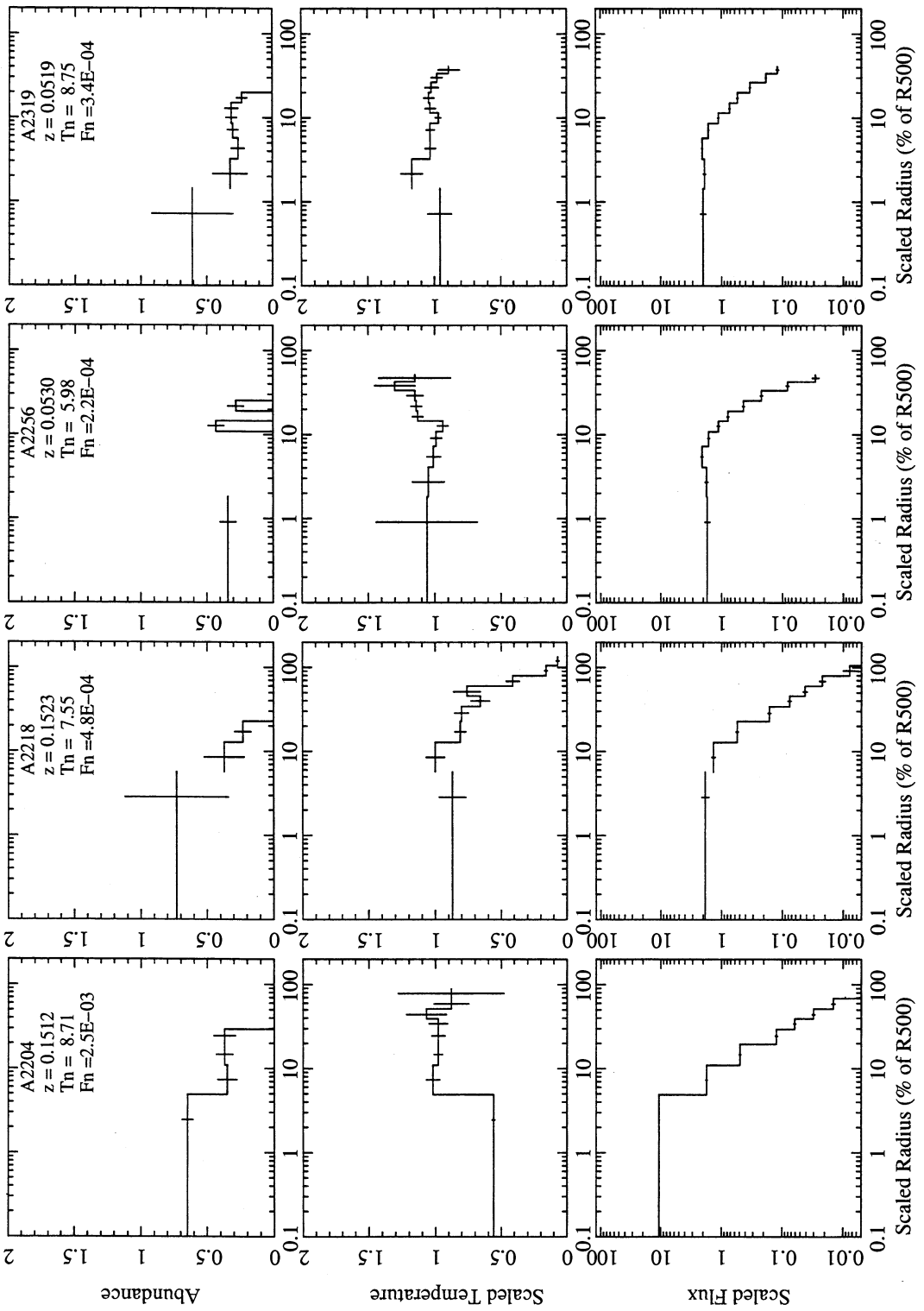

Fig. 26.— Cluster temperature, abundance, and flux radial profiles.

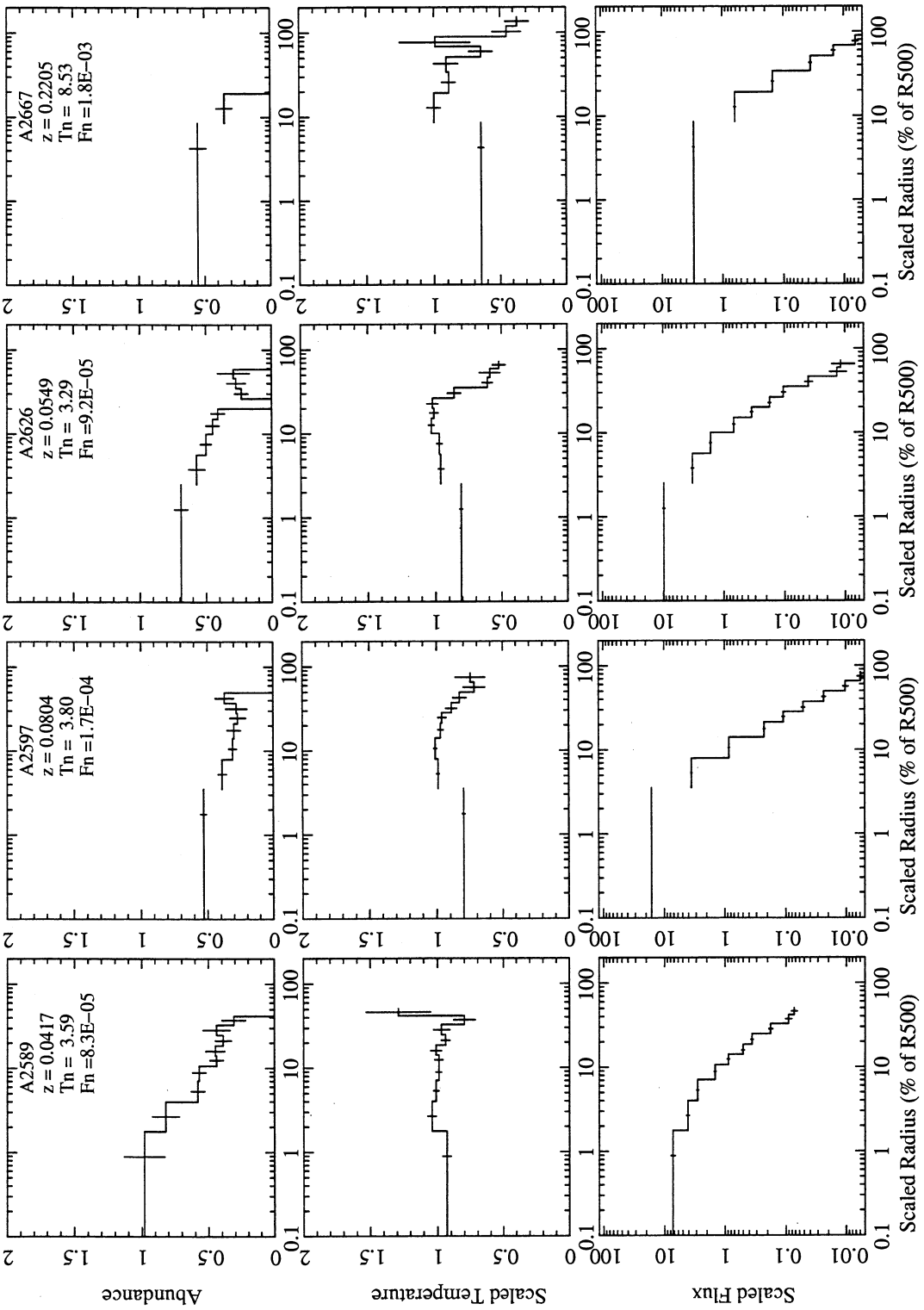

Fig. 27.— Cluster temperature, abundance, and flux radial profiles.

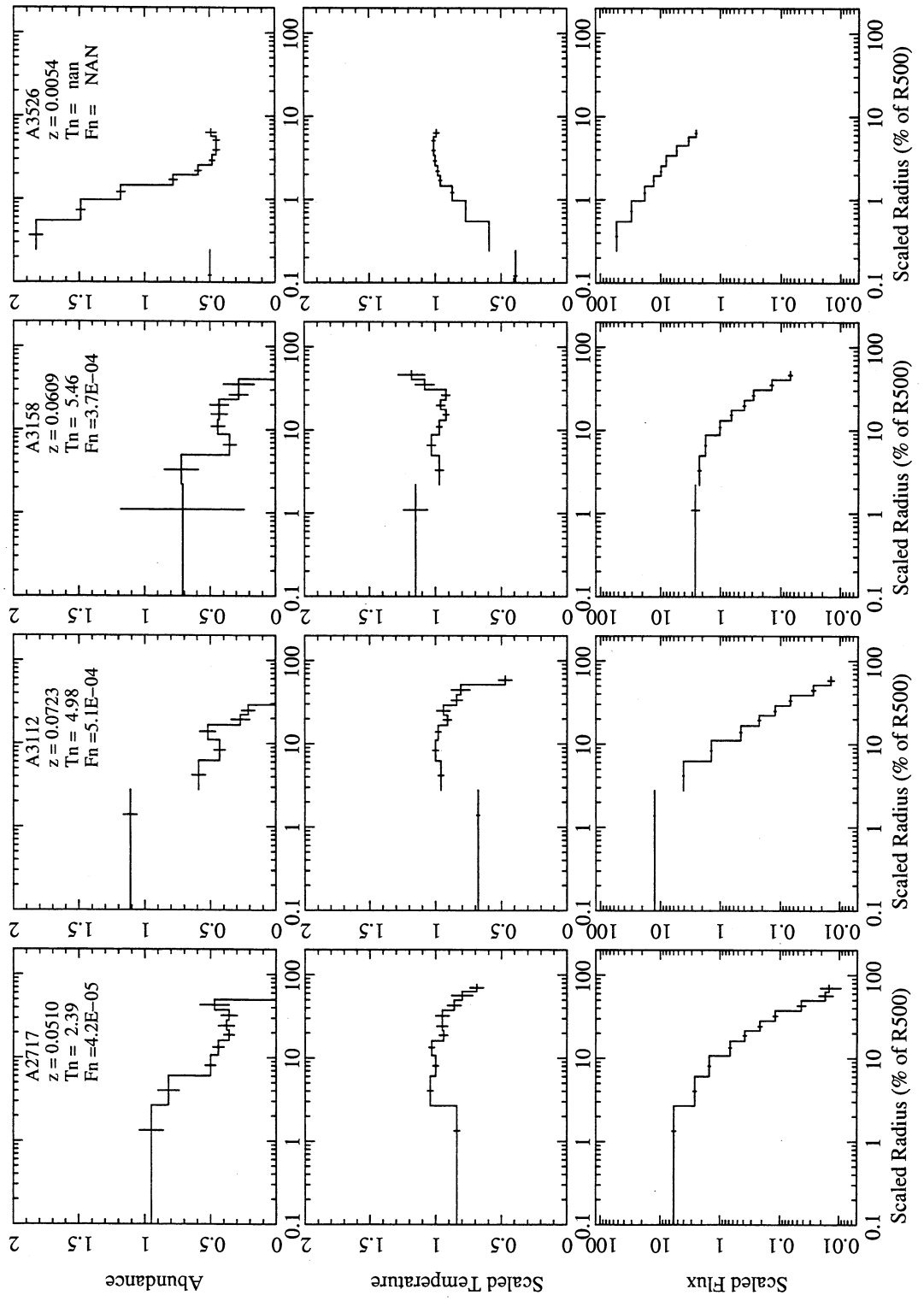

Fig. 28.— Cluster temperature, abundance, and flux radial profiles.

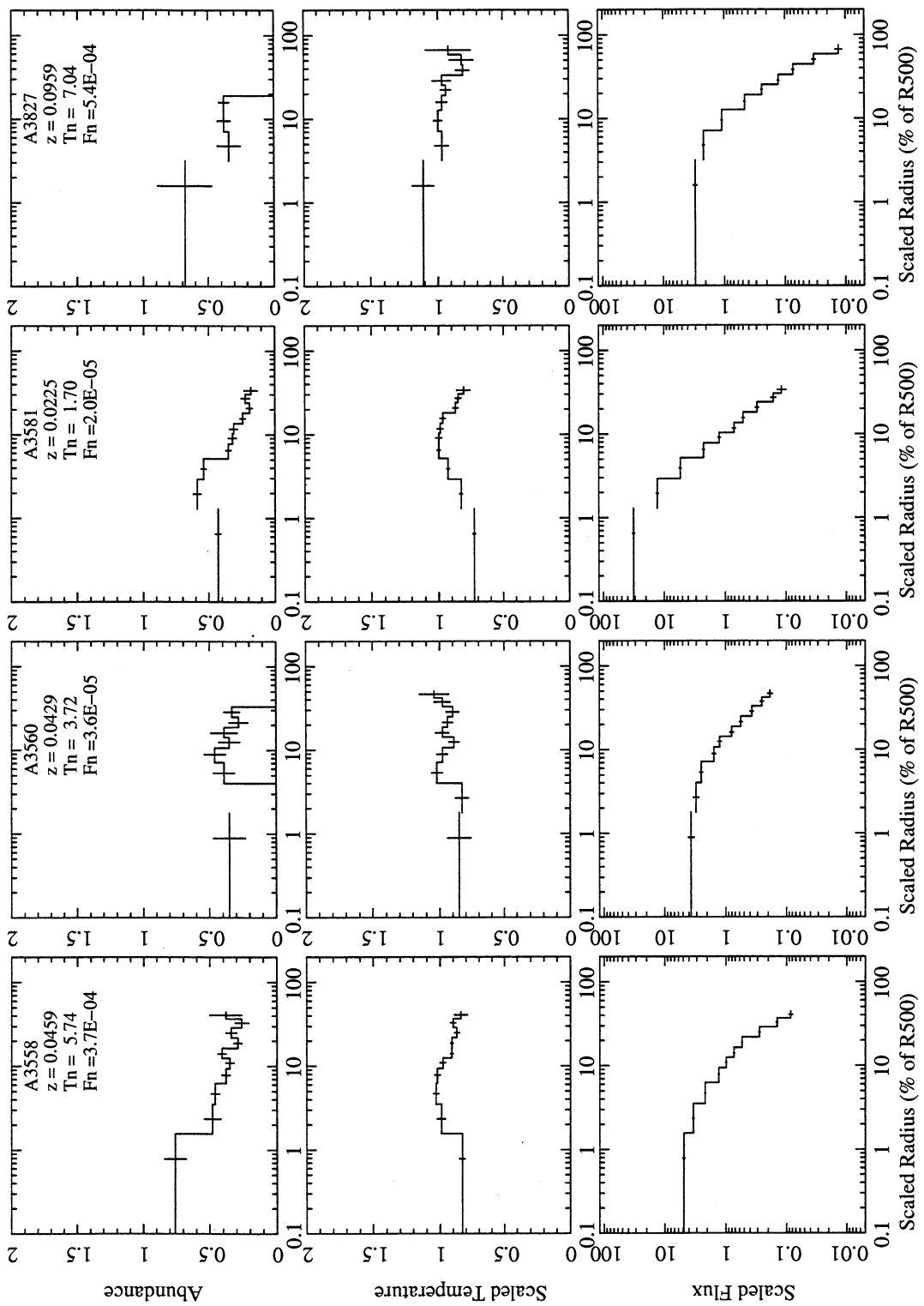

Fig. 29.— Cluster temperature, abundance, and flux radial profiles.

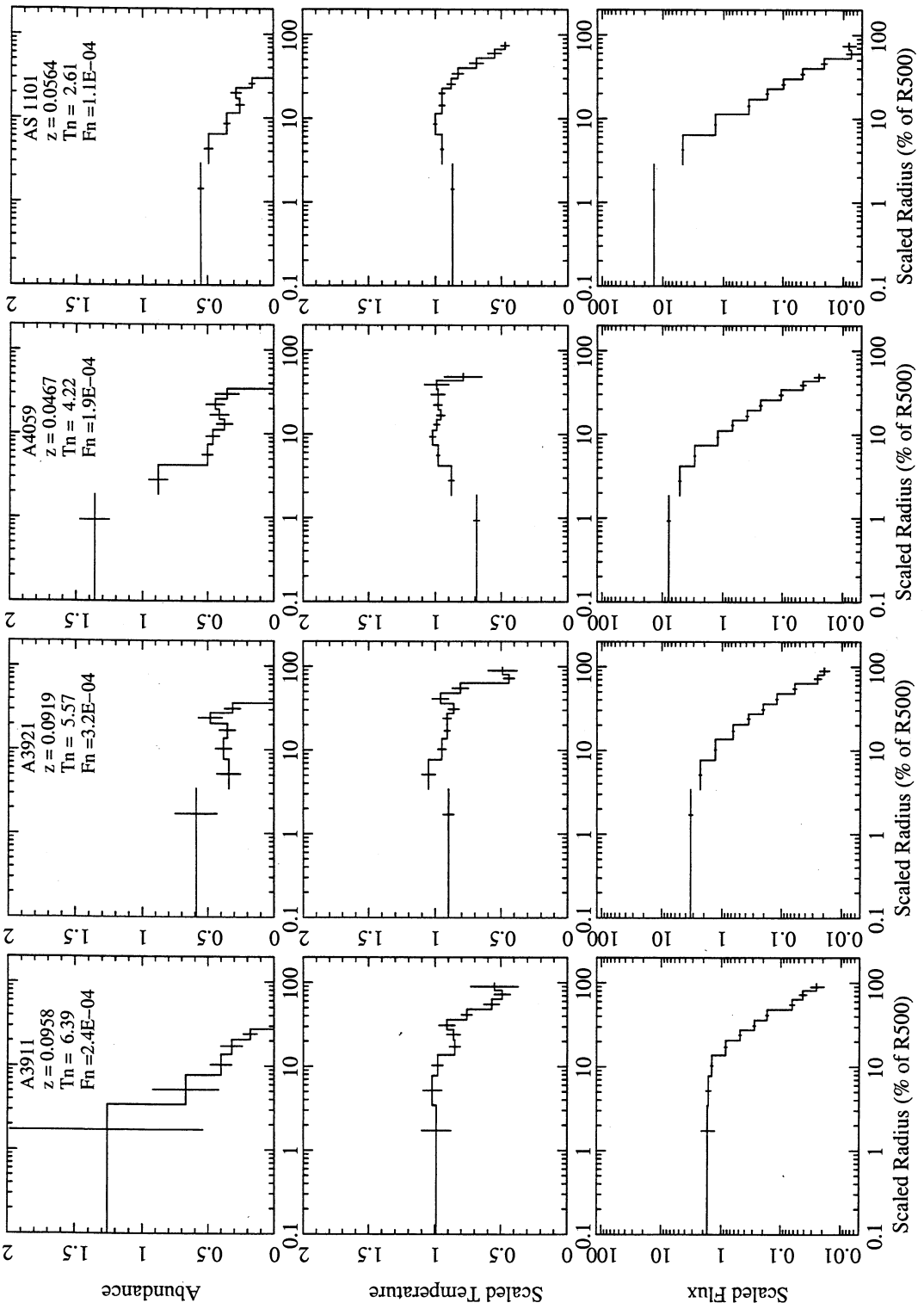

Fig. 30.— Cluster temperature, abundance, and flux radial profiles.

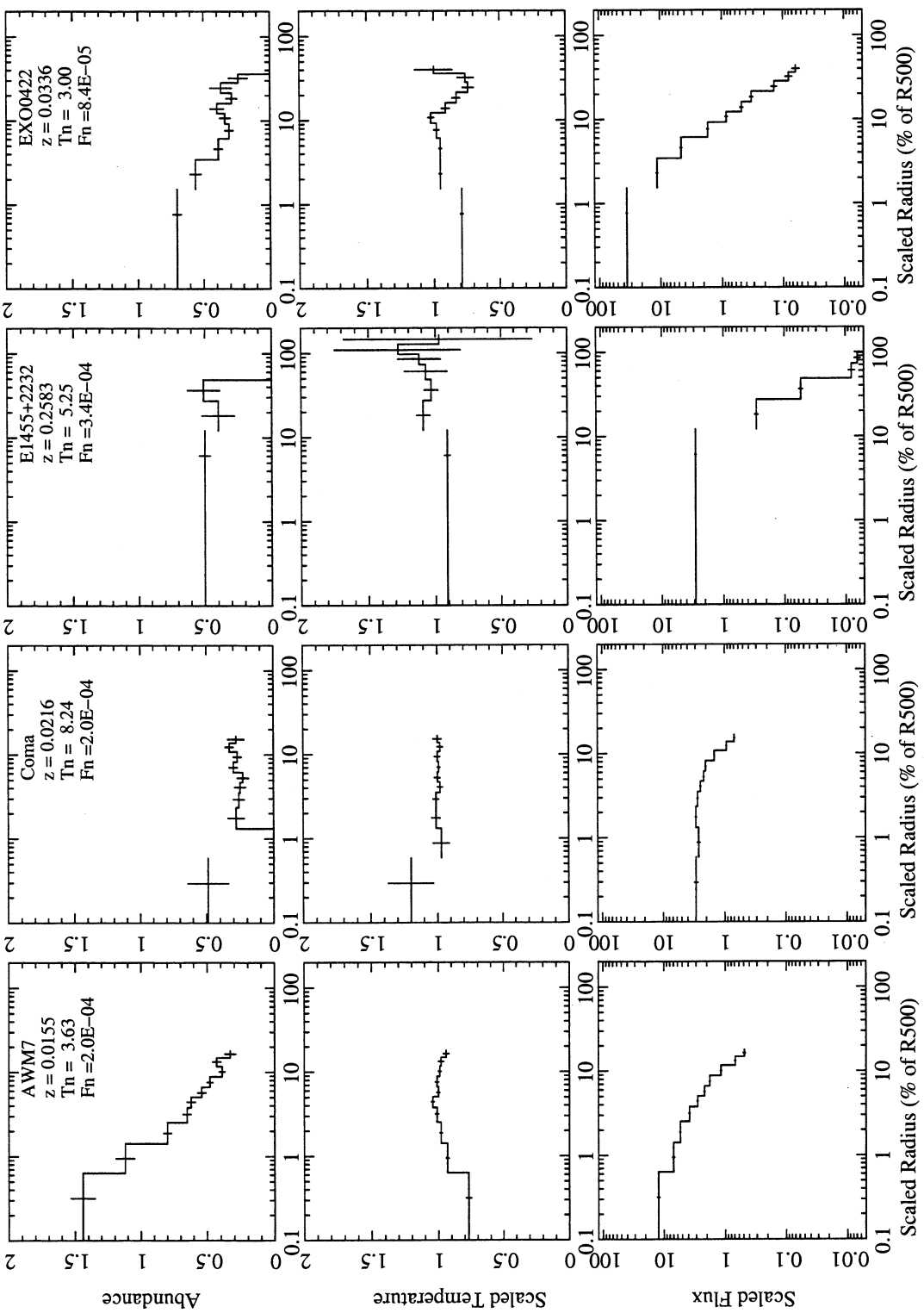

Fig. 31.— Cluster temperature, abundance, and flux radial profiles.

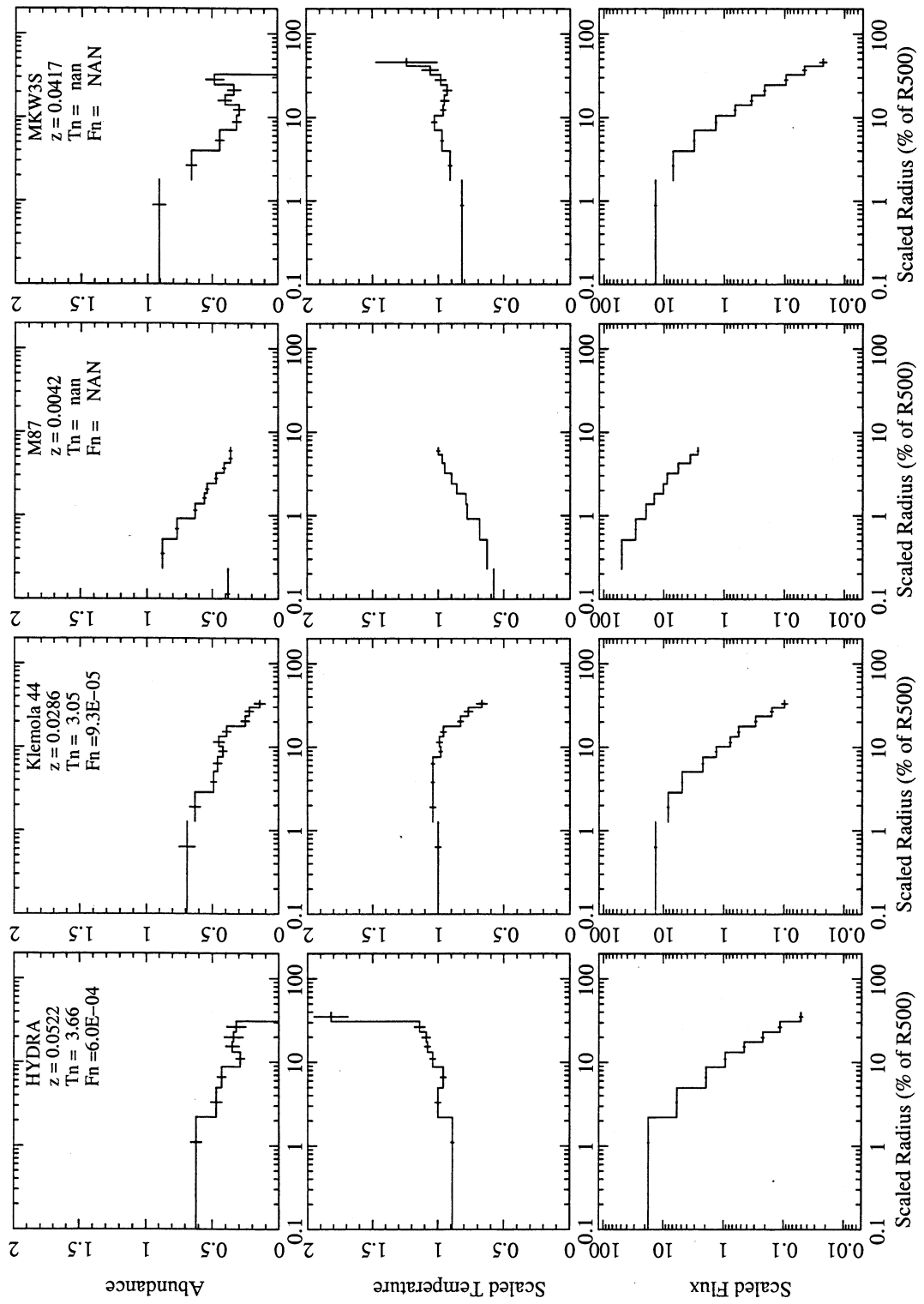

Fig. 32.— Cluster temperature, abundance, and flux radial profiles.

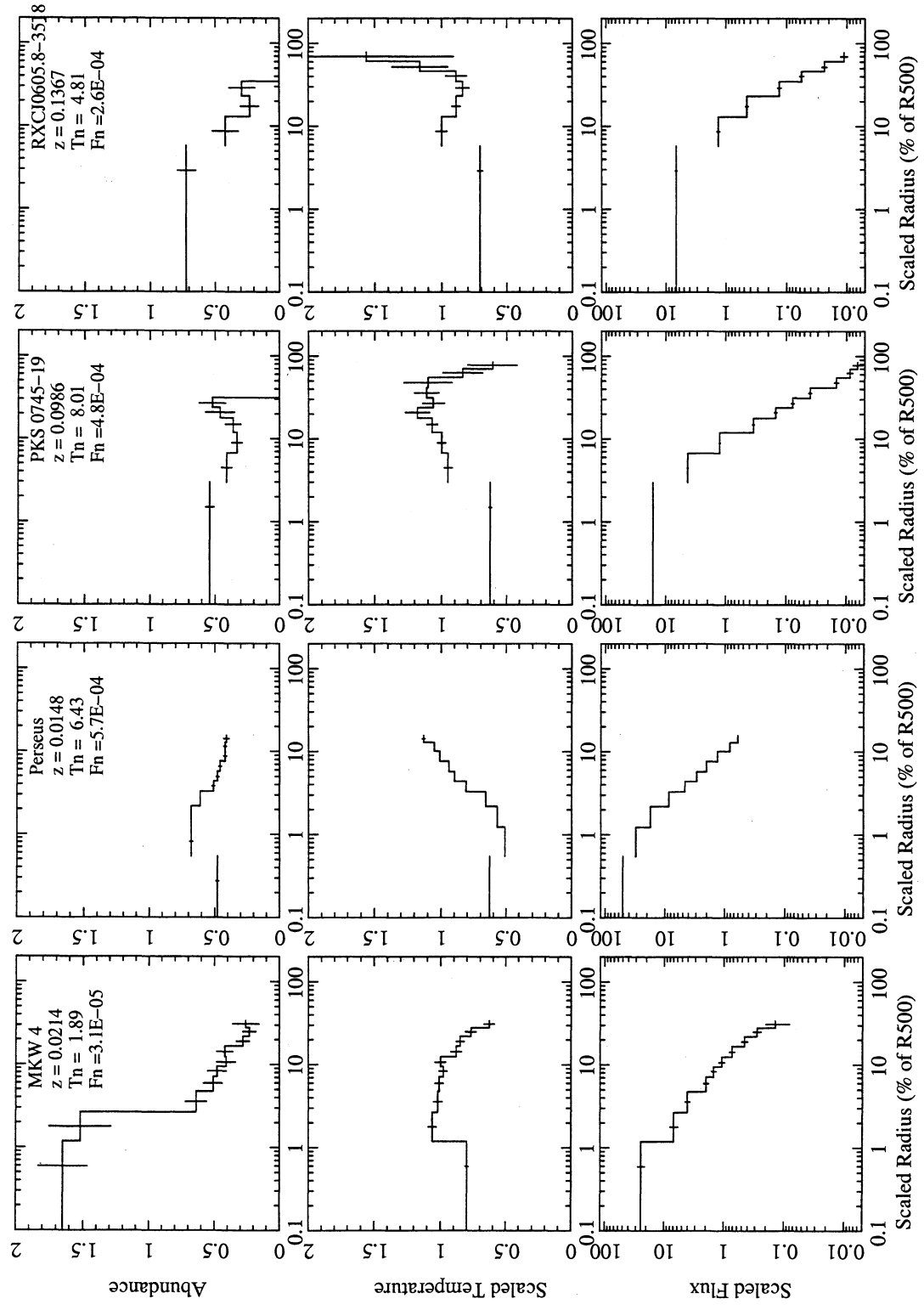

Fig. 33.— Cluster temperature, abundance, and flux radial profiles.

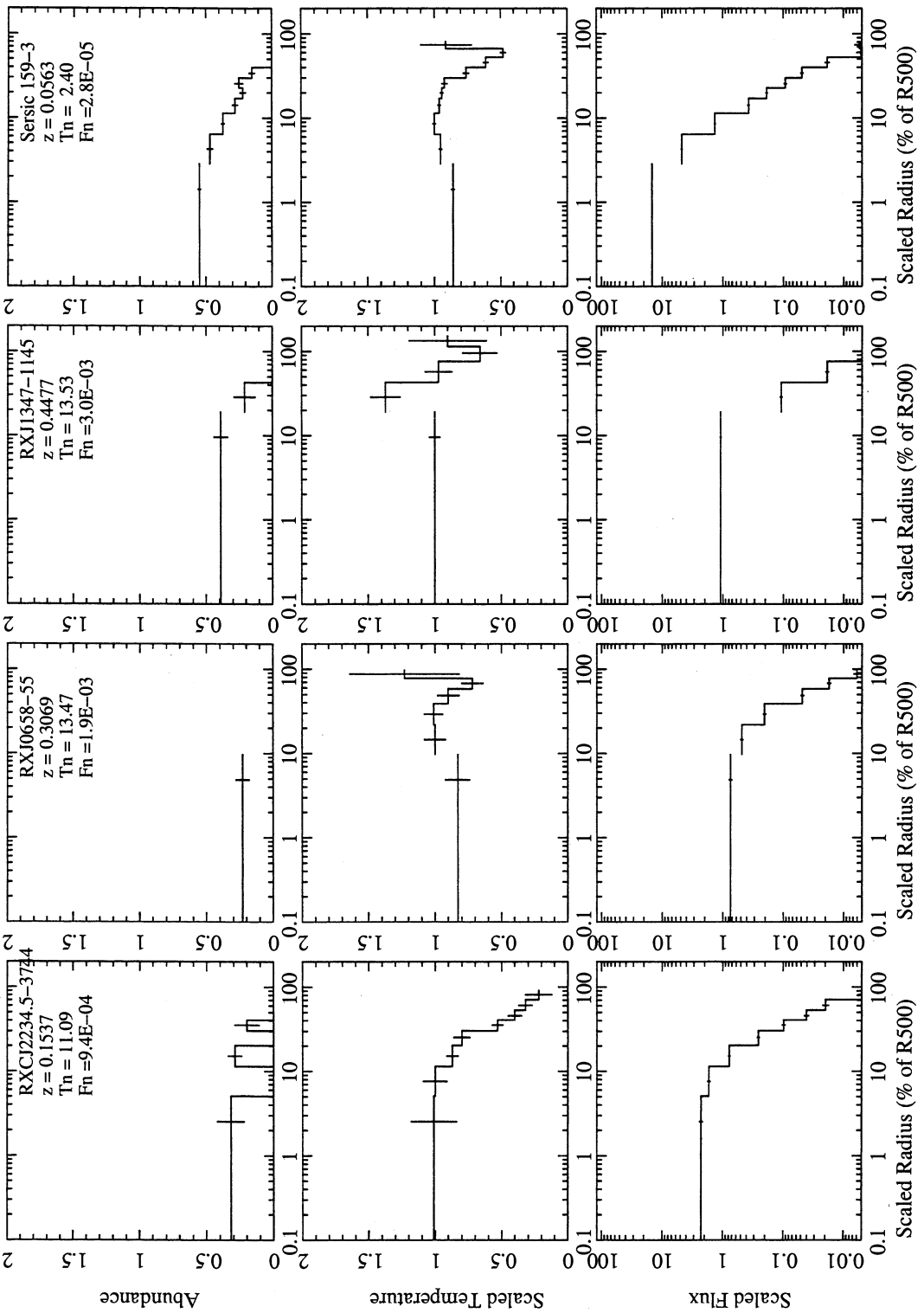

Fig. 34.— Cluster temperature, abundance, and flux radial profiles.

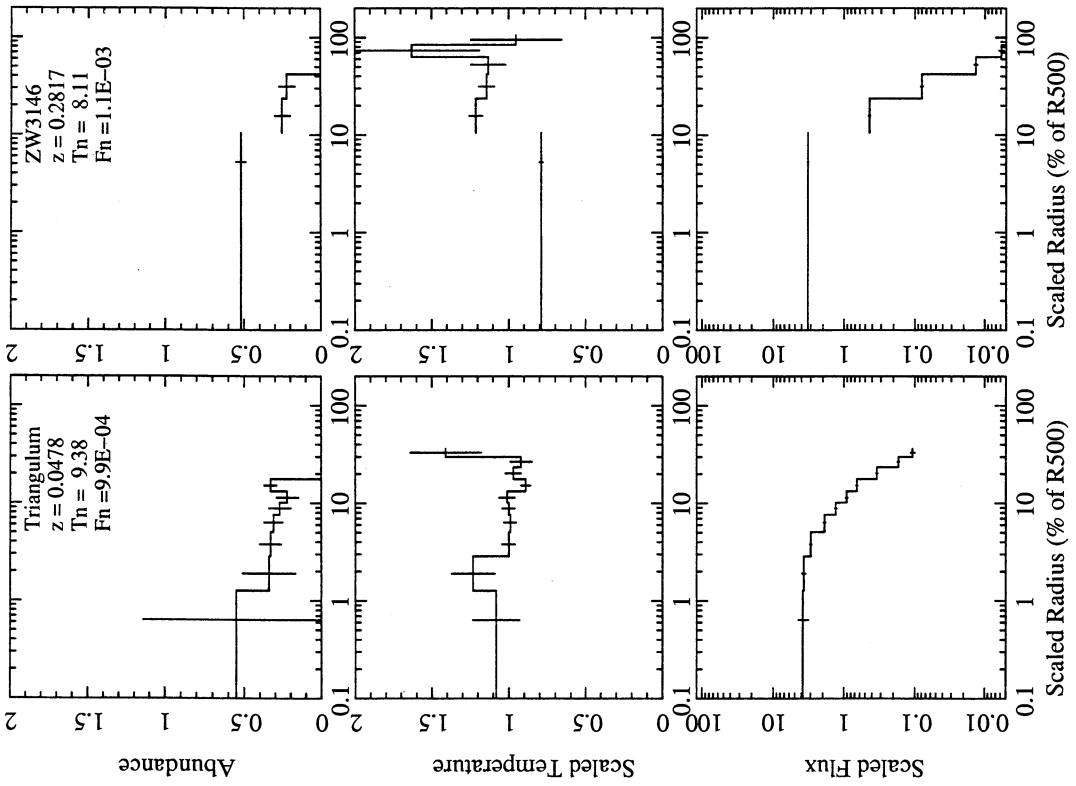

Fig. 35.— Cluster temperature, abundance, and flux radial profiles.

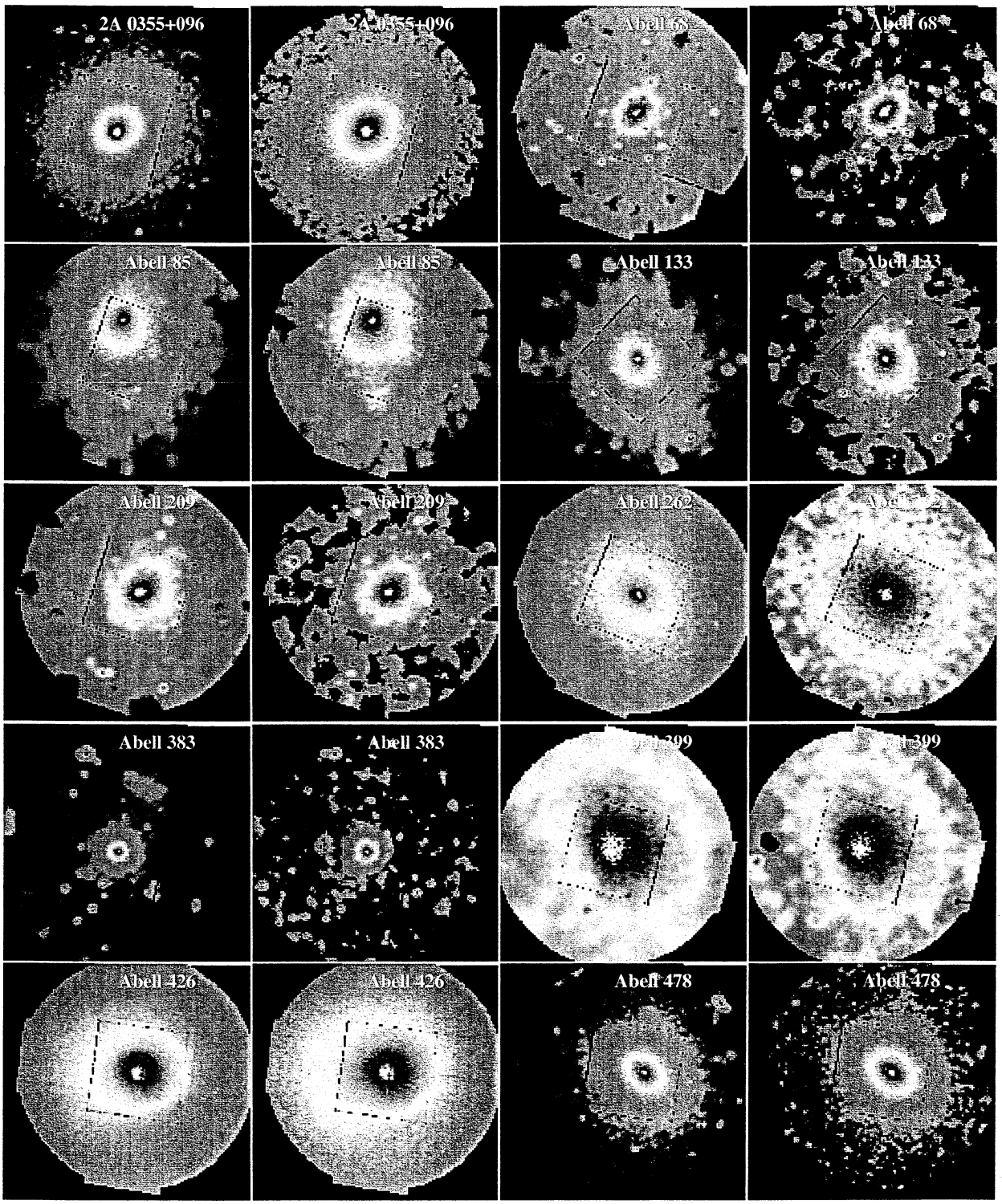

Fig. 36.— Soft (left) and hard (right) band images of the clusters.

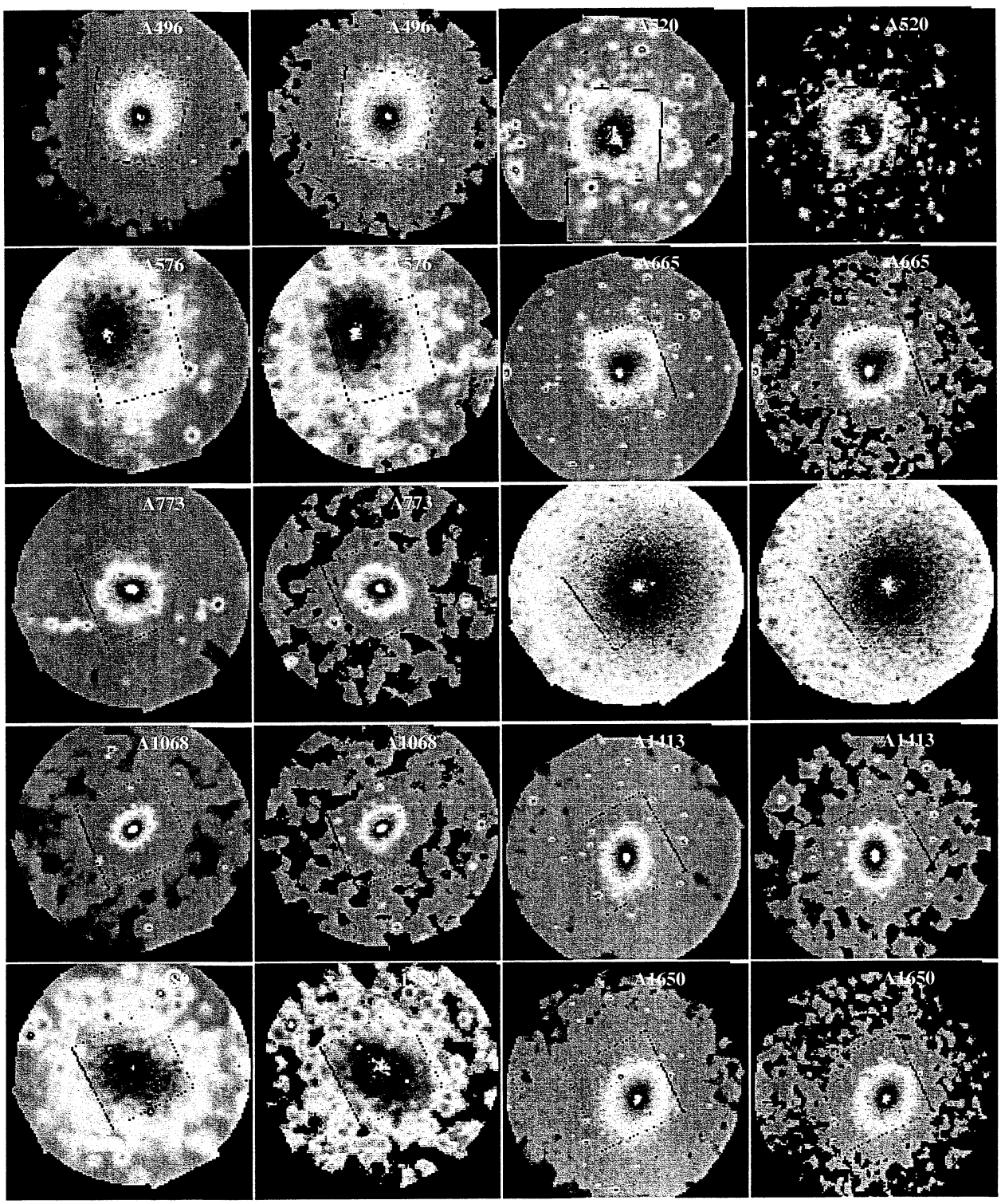

Fig. 37.— Soft (left) and hard (right) band images of the clusters.

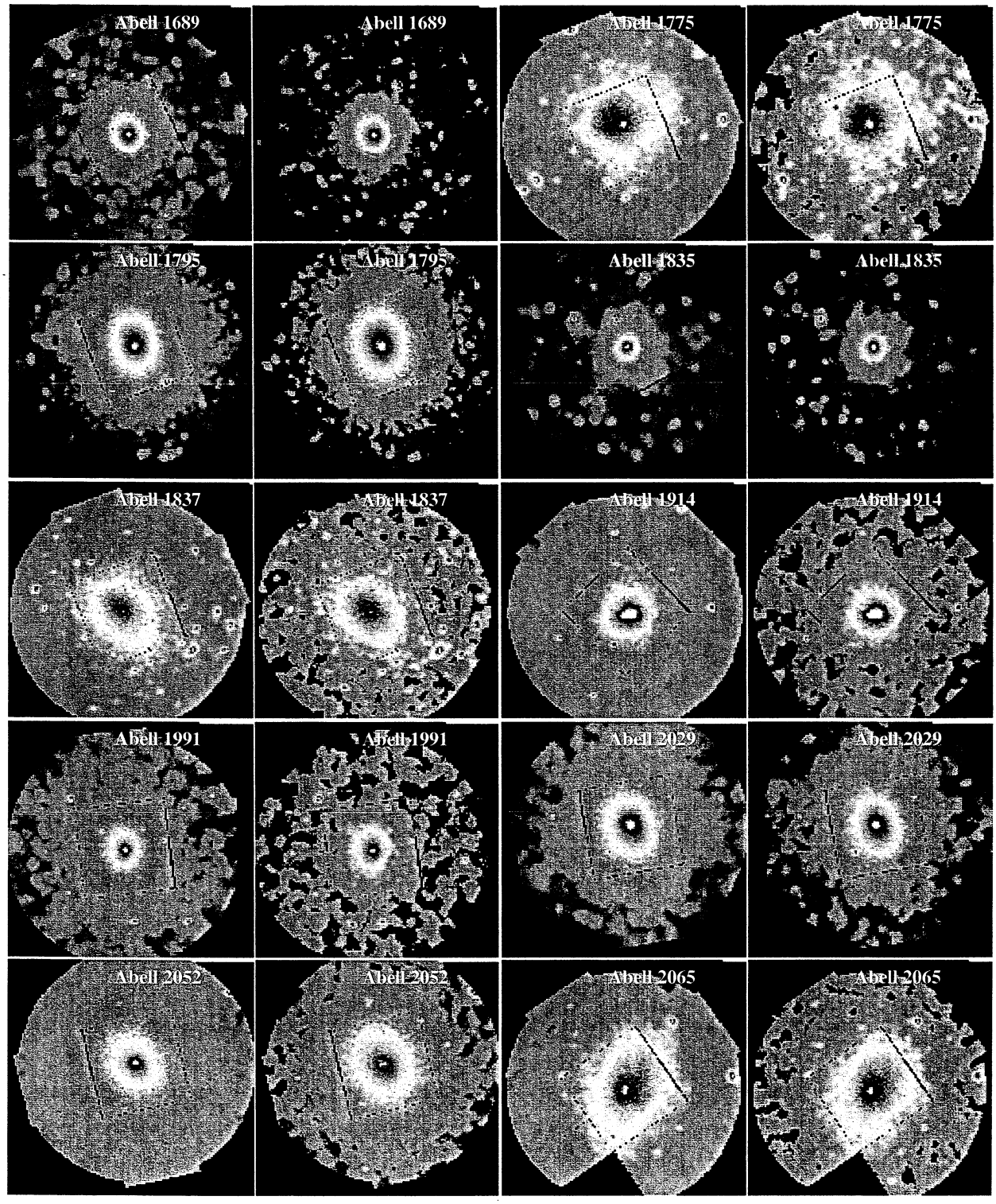

Fig. 38.— Soft (left) and hard (right) band images of the clusters.

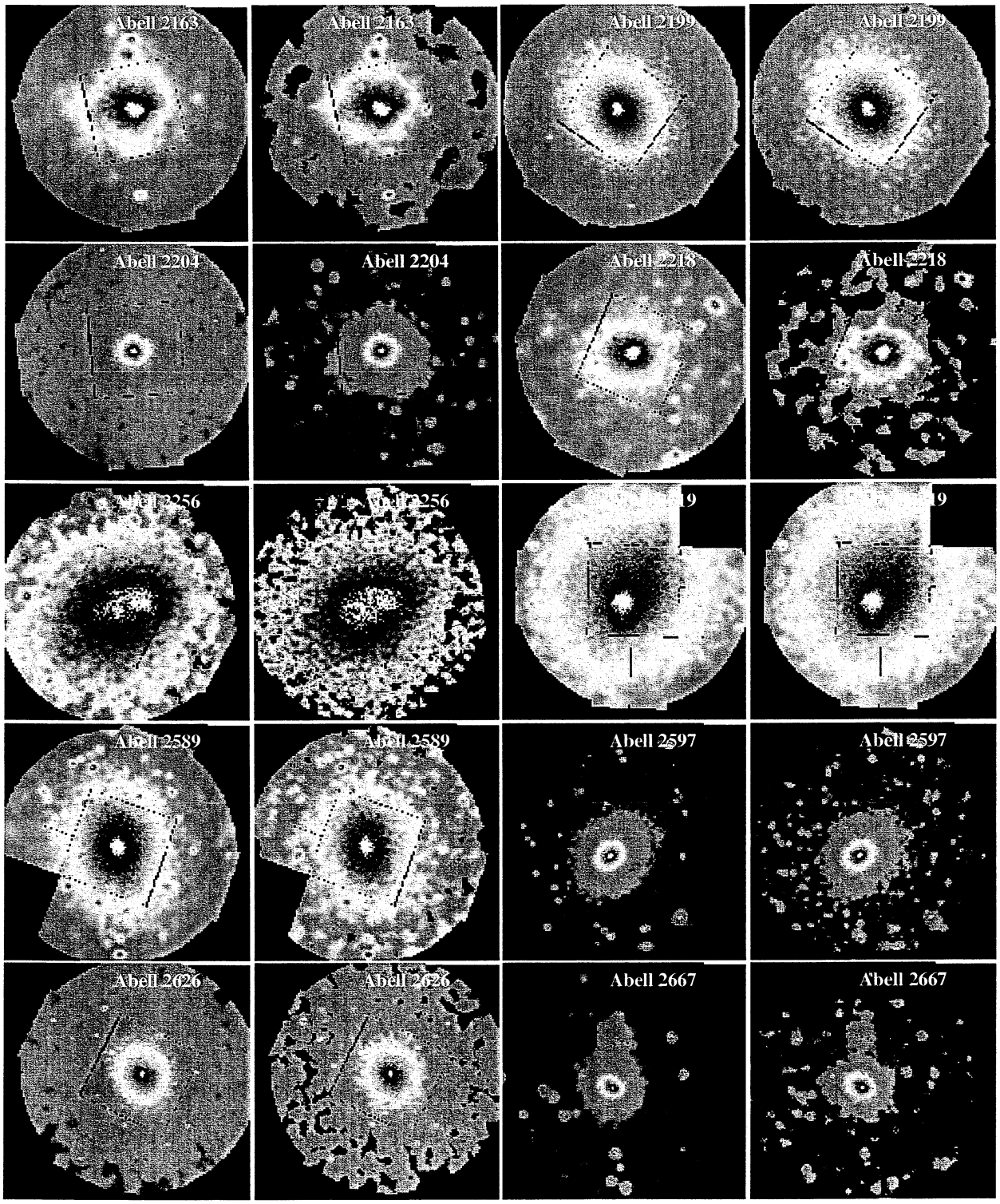

Fig. 39.— Soft (left) and hard (right) band images of the clusters.

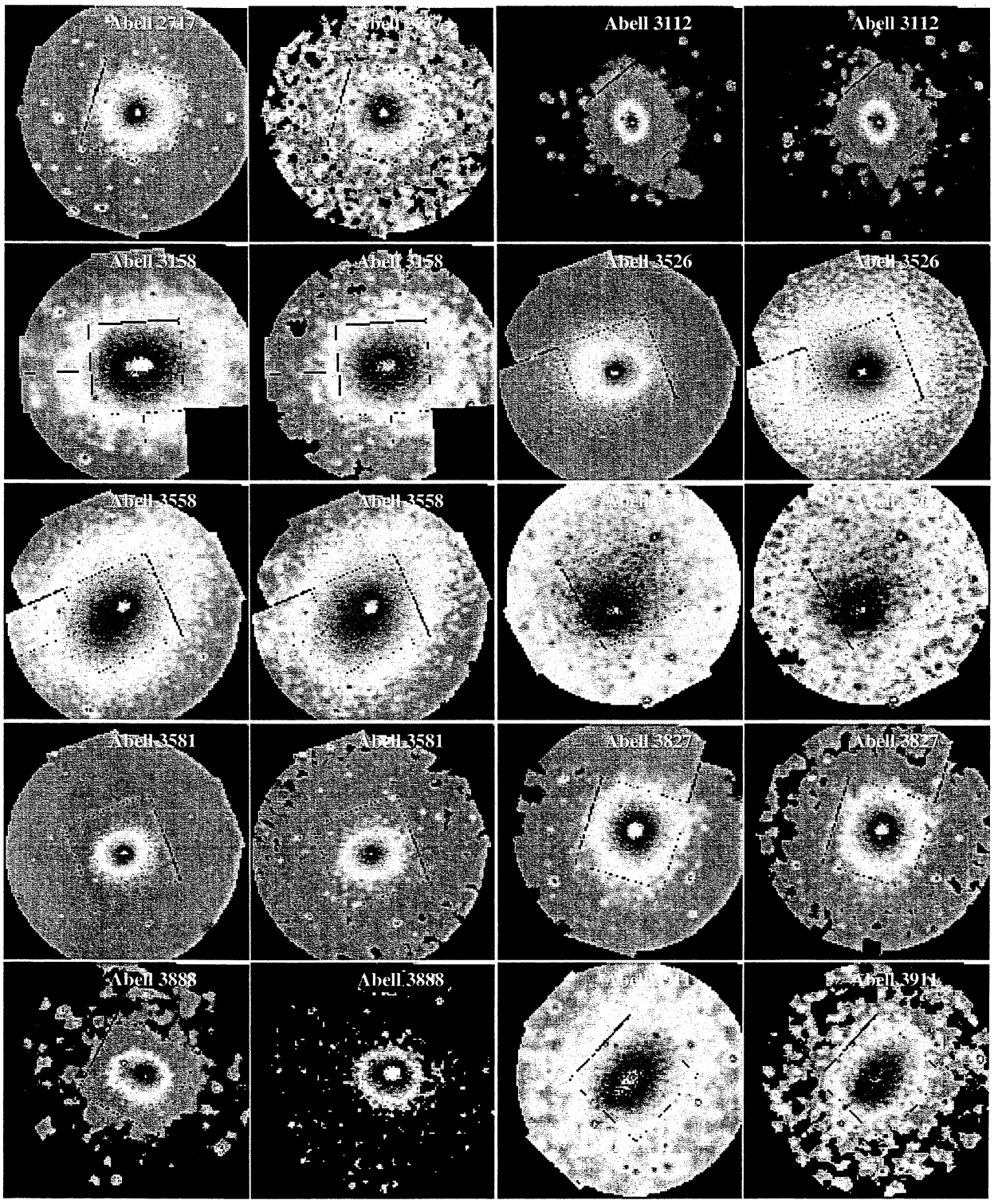

Fig. 40.— Soft (left) and hard (right) band images of the clusters.

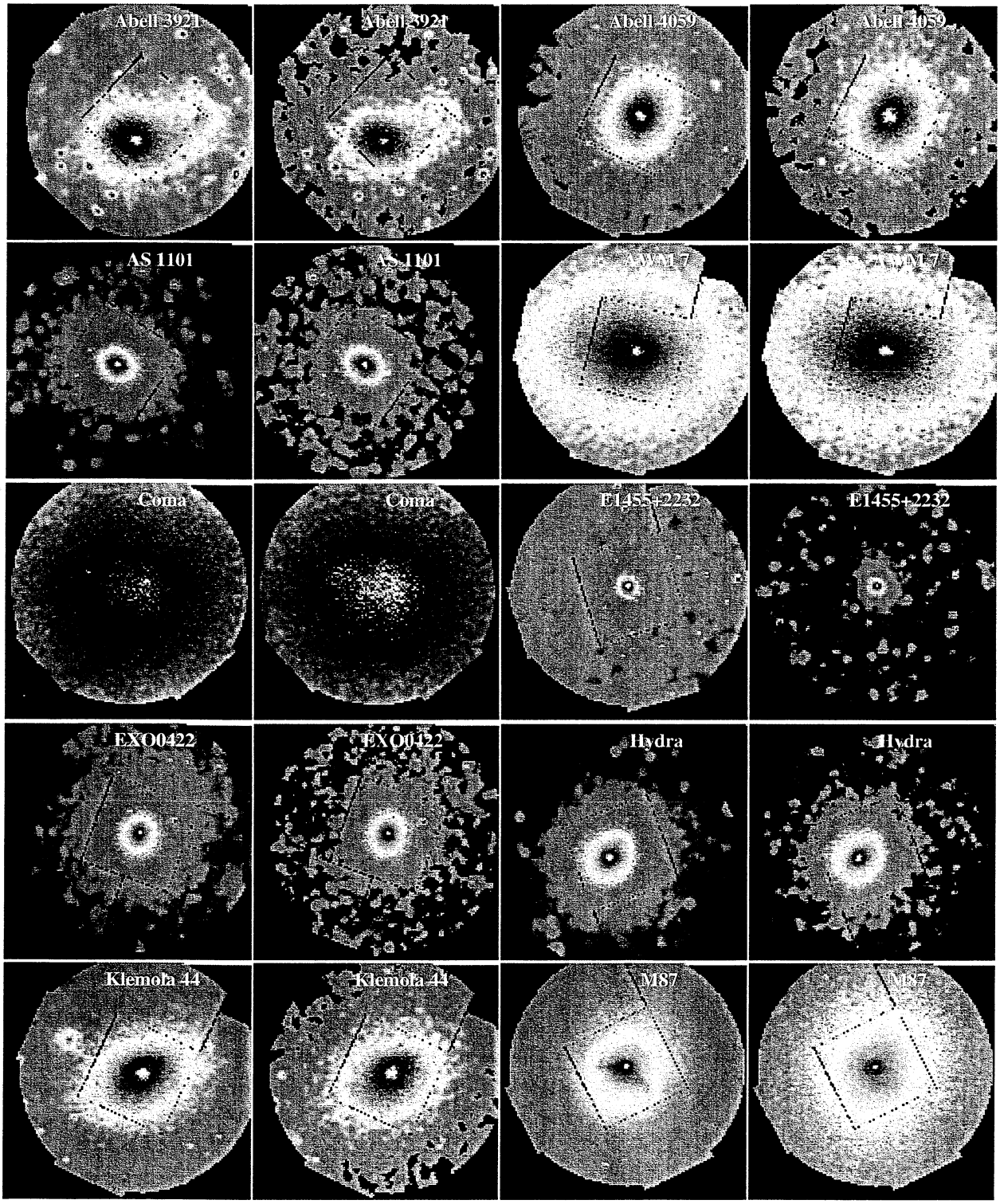

Fig. 41.— Soft (left) and hard (right) band images of the clusters.

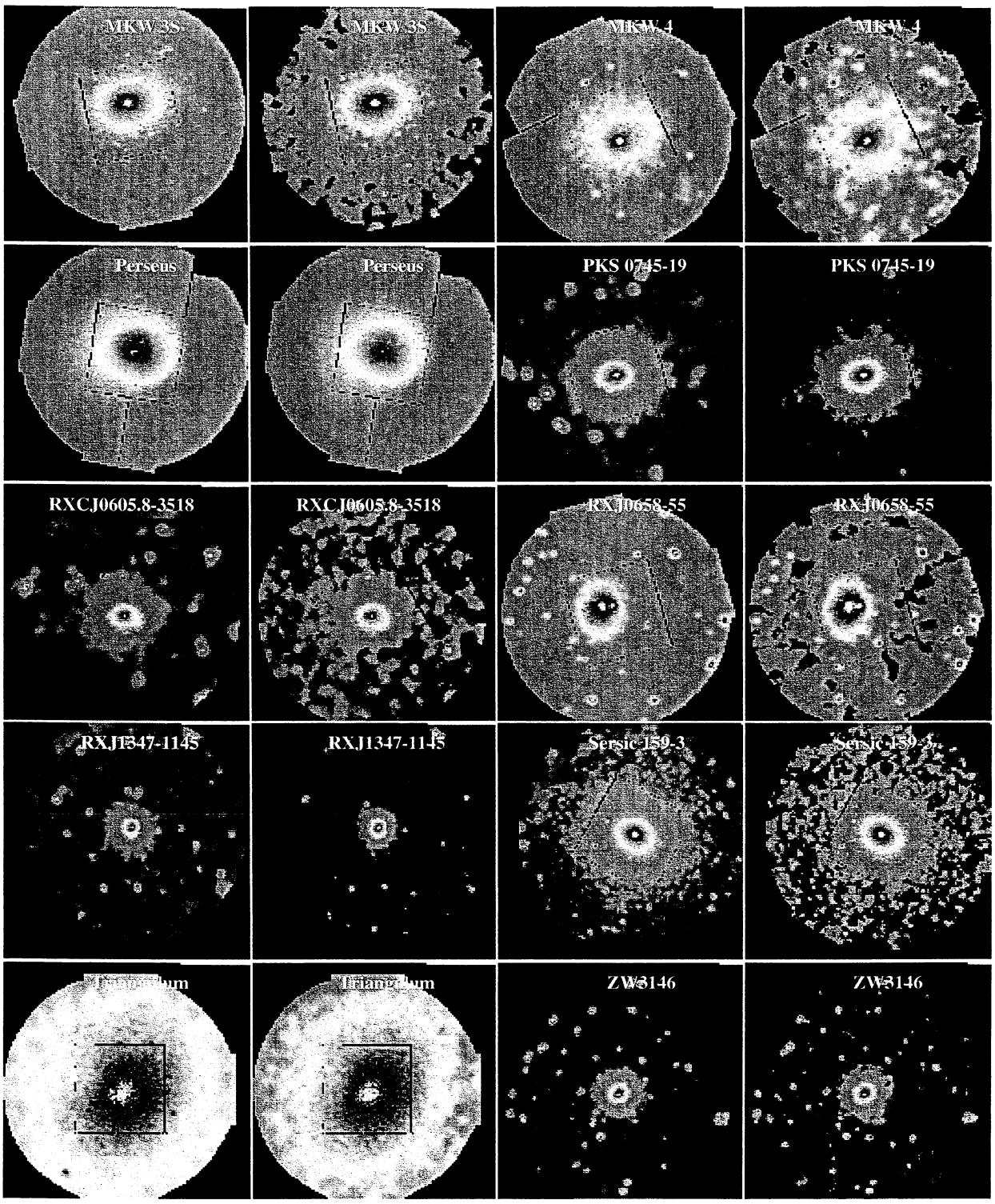

Fig. 42.— Soft (left) and hard (right) band images of the clusters.

TABLE 4
CLUSTER DETAILS

Cluster	Annulus	T (keV)	σ_T (keV)	A	σ_A	F ergs cm^{-2} s^{-1}	σ_F ergs cm^{-2} s^{-1}
2A 0335+096	1	1.542	0.008	0.371	0.011	1.876E-11	3.418E-13
-	2	2.383	0.011	0.708	0.015	8.398E-12	7.855E-14
-	3	3.011	0.014	0.612	0.013	2.607E-12	2.435E-14
-	4	3.225	0.020	0.502	0.016	9.532E-13	1.205E-14
-	5	3.233	0.025	0.449	0.018	4.965E-13	7.645E-15
-	6	3.257	0.033	0.447	0.024	2.619E-13	5.298E-15
-	7	3.072	0.041	0.321	0.021	1.557E-13	3.270E-15
-	8	3.019	0.053	0.381	0.031	6.525E-14	1.988E-15
-	9	2.826	0.078	0.346	0.037	3.062E-14	1.272E-15
-	10	2.721	0.133	0.221	0.063	1.871E-14	1.534E-15
A68	1	7.487	0.726	0.254	0.162	1.351E-12	8.749E-14
-	2	7.803	0.635	0.274	0.081	6.687E-13	3.194E-14
-	3	6.966	0.541	-	-	2.102E-13	1.026E-14
-	4	5.897	0.711	-	-	4.401E-14	3.147E-15
-	5	5.621	1.241	-	-	1.627E-14	1.696E-15
-	6	3.606	0.893	-	-	7.168E-15	1.210E-15
A85	1	3.618	0.084	1.161	0.089	1.043E-11	3.047E-13
-	2	5.089	0.145	0.567	0.077	3.921E-12	1.196E-13
-	3	5.321	0.103	0.521	0.053	1.946E-12	4.617E-14
-	4	5.972	0.185	0.379	0.062	1.043E-12	2.906E-14
-	5	6.269	0.195	0.428	0.069	6.139E-13	1.849E-14
-	6	6.246	0.273	0.356	0.095	3.046E-13	1.264E-14
-	7	6.305	0.157	0.319	0.047	2.548E-13	5.778E-15
-	8	6.047	0.292	0.322	0.080	1.005E-13	3.874E-15
-	9	5.679	0.404	-	-	5.382E-14	2.515E-15
-	10	7.177	1.115	-	-	3.768E-14	2.496E-15
A133	1	2.376	0.044	1.056	0.070	4.090E-12	1.694E-13
-	2	3.848	0.100	0.872	0.098	1.338E-12	6.631E-14
-	3	4.300	0.087	0.555	0.061	5.686E-13	1.958E-14
-	4	4.222	0.107	0.472	0.072	2.436E-13	1.022E-14
-	5	4.159	0.137	0.338	0.081	1.322E-13	6.600E-15
-	6	3.997	0.176	0.397	0.105	7.203E-14	4.713E-15
-	7	3.738	0.180	0.457	0.095	4.473E-14	2.857E-15
-	8	3.940	0.337	0.423	0.171	1.829E-14	2.092E-15
-	9	2.658	0.296	0.381	0.172	6.742E-15	1.381E-15
-	10	2.314	0.640	-	-	3.300E-15	1.160E-15
A209	1	6.946	0.855	0.778	0.486	1.608E-12	2.603E-13
-	2	6.766	0.422	0.336	0.072	7.642E-13	3.837E-14
-	3	7.303	0.470	-	-	3.035E-13	1.466E-14
-	4	7.993	0.668	-	-	1.053E-13	5.632E-15

TABLE 4—*Continued*

Cluster	Annulus	T (keV)	σ_T (keV)	A	σ_A	F ergs cm^{-2} s^{-1}	σ_F ergs cm^{-2} s^{-1}
-	5	6.892	0.915	0.233	0.164	5.042E-14	4.214E-15
-	6	5.603	0.821	-	-	2.559E-14	2.532E-15
-	7	4.867	0.776	-	-	1.127E-14	1.354E-15
A262	1	1.270	0.010	0.495	0.030	2.636E-12	1.431E-13
-	2	1.889	0.032	1.108	0.083	1.182E-12	8.022E-14
-	3	2.121	0.022	0.656	0.037	5.865E-13	2.203E-14
-	4	2.140	0.025	0.408	0.028	3.609E-13	1.258E-14
-	5	2.141	0.027	0.381	0.027	2.596E-13	9.249E-15
-	6	2.161	0.034	0.380	0.030	1.783E-13	6.973E-15
-	7	2.198	0.040	0.359	0.024	1.380E-13	4.556E-15
-	8	2.102	0.034	0.322	0.027	7.796E-14	3.110E-15
-	9	1.982	0.041	0.306	0.027	4.649E-14	2.197E-15
-	10	1.983	0.072	0.299	0.046	3.336E-14	2.703E-15
A383	1	3.643	0.078	0.746	0.062	3.913E-12	1.319E-13
-	2	5.573	0.374	0.363	0.116	6.474E-13	3.522E-14
-	3	4.812	0.251	0.325	0.095	1.463E-13	8.377E-15
-	4	4.449	0.543	-	-	2.879E-14	2.356E-15
-	5	3.615	0.628	-	-	1.149E-14	1.350E-15
-	6	3.717	0.976	-	-	6.276E-15	9.834E-16
-	7	3.678	1.145	-	-	2.919E-15	6.450E-16
-	8	0.000	0.000	-	-	2.322E-15	5.781E-16
A399	1	9.840	1.980	0.465	0.097	1.277E-12	8.760E-14
-	2	6.665	0.525	-	-	9.888E-13	5.274E-14
-	3	6.704	0.279	-	-	7.264E-13	3.330E-14
-	4	7.509	0.451	0.287	0.103	4.289E-13	1.987E-14
-	5	6.425	0.332	0.343	0.123	2.669E-13	1.452E-14
-	6	6.445	0.375	0.330	0.093	1.680E-13	8.158E-15
-	7	6.258	0.333	-	-	1.174E-13	5.524E-15
-	8	6.520	0.464	0.154	0.135	6.528E-14	4.130E-15
-	9	7.380	0.854	-	-	3.345E-14	2.304E-15
A426	1	3.973	0.021	0.560	0.014	4.996E-11	2.180E-13
-	2	3.195	0.099	0.689	0.009	3.128E-11	1.100E-13
-	3	3.598	0.088	0.675	0.006	1.912E-11	4.198E-14
-	4	4.199	0.011	0.584	0.007	9.600E-12	2.714E-14
-	5	5.044	0.019	0.506	0.009	5.425E-12	1.993E-14
-	6	5.612	0.033	0.460	0.011	3.417E-12	1.522E-14
-	7	5.926	0.030	0.441	0.010	2.217E-12	9.354E-15
-	8	6.309	0.038	0.401	0.012	1.298E-12	6.978E-15
-	9	6.612	0.040	0.410	0.014	8.264E-13	4.970E-15
-	10	7.006	0.099	0.397	0.025	6.279E-13	6.522E-15

TABLE 4—*Continued*

Cluster	Annulus	T (keV)	σ_T (keV)	A	σ_A	F ergs cm^{-2} s^{-1}	σ_F ergs cm^{-2} s^{-1}
A478	1	4.499	0.049	0.551	0.019	2.252E-11	1.605E-13
-	2	6.086	0.085	0.403	0.020	6.245E-12	5.471E-14
-	3	6.290	0.069	0.383	0.016	2.400E-12	2.168E-14
-	4	6.610	0.108	0.335	0.023	7.404E-13	1.081E-14
-	5	6.497	0.138	0.307	0.028	3.604E-13	6.688E-15
-	6	6.508	0.201	0.276	0.040	1.766E-13	4.659E-15
-	7	6.124	0.217	0.415	0.045	8.236E-14	2.378E-15
-	8	8.367	0.533	-	-	3.657E-14	1.253E-15
A496	1	2.479	0.032	1.038	0.055	9.749E-12	2.396E-13
-	2	3.176	0.048	0.715	0.046	3.833E-12	9.996E-14
-	3	3.682	0.050	0.572	0.032	1.821E-12	3.596E-14
-	4	4.135	0.063	0.449	0.038	8.506E-13	1.951E-14
-	5	4.233	0.070	0.428	0.042	5.433E-13	1.379E-14
-	6	4.536	0.122	0.290	0.047	3.372E-13	9.425E-15
-	7	4.185	0.080	0.333	0.042	2.164E-13	5.848E-15
-	8	4.130	0.111	0.300	0.041	1.146E-13	3.586E-15
-	9	4.020	0.144	-	-	5.824E-14	2.305E-15
-	10	4.289	0.305	-	-	3.519E-14	2.253E-15
A520	1	9.176	1.306	0.210	0.121	7.735E-13	4.718E-14
-	2	7.264	0.593	-	-	6.521E-13	3.517E-14
-	3	8.960	0.509	0.285	0.054	4.198E-13	1.500E-14
-	4	8.576	0.744	-	-	1.357E-13	5.567E-15
-	5	6.629	0.516	-	-	5.353E-14	2.720E-15
-	6	10.682	1.638	-	-	3.200E-14	1.986E-15
-	7	4.873	0.709	-	-	1.326E-14	1.076E-15
-	8	6.524	2.797	-	-	4.687E-15	8.559E-16
A576	1	3.270	0.411	0.838	0.536	9.522E-13	2.921E-13
-	2	3.782	0.364	0.712	0.320	6.781E-13	1.163E-13
-	3	3.804	0.165	0.714	0.143	4.255E-13	3.632E-14
-	4	4.068	0.192	0.323	0.122	2.755E-13	2.184E-14
-	5	4.262	0.188	0.529	0.155	2.270E-13	1.976E-14
-	6	3.962	0.212	0.430	0.139	1.335E-13	1.199E-14
-	7	3.322	0.137	0.432	0.091	7.780E-14	5.767E-15
-	8	3.054	0.216	0.261	0.081	3.749E-14	3.515E-15
-	9	3.212	0.304	-	-	2.039E-14	2.406E-15
-	10	2.759	0.681	-	-	9.953E-15	2.048E-15
A665	1	7.240	0.561	0.112	0.128	1.017E-12	5.132E-14
-	2	7.810	0.291	0.298	0.062	9.722E-13	2.646E-14
-	3	7.998	0.191	0.282	0.036	5.992E-13	1.106E-14
-	4	8.114	0.277	0.388	0.061	2.001E-13	5.455E-15

TABLE 4—*Continued*

Cluster	Annulus	T (keV)	σ_T (keV)	A	σ_A	F ergs cm^{-2} s^{-1}	σ_F ergs cm^{-2} s^{-1}
-	5	7.881	0.367	0.241	0.075	9.623E-14	3.204E-15
-	6	6.475	0.327	0.350	0.104	5.830E-14	2.750E-15
-	7	4.689	0.331	0.187	0.066	1.847E-14	1.027E-15
-	8	2.222	0.281	-	-	4.497E-15	7.020E-16
-	9	1.540	0.198	-	-	1.300E-15	4.385E-16
-	10	1.160	0.135	-	-	1.309E-15	5.928E-16
A773	1	10.816	1.210	0.525	0.173	1.888E-12	1.390E-13
-	2	6.933	0.725	-	-	8.006E-13	6.707E-14
-	3	8.095	0.651	0.299	0.144	2.624E-13	2.015E-14
-	4	7.505	0.907	-	-	8.074E-14	6.870E-15
-	5	7.463	1.243	0.238	0.277	3.993E-14	4.874E-15
-	6	5.162	1.127	-	-	1.194E-14	2.091E-15
-	7	3.538	0.959	-	-	5.400E-15	1.328E-15
A1060	1	3.081	0.108	0.759	0.110	1.194E-12	8.366E-14
-	2	3.374	0.071	0.671	0.071	9.606E-13	4.290E-14
-	3	3.330	0.040	0.469	0.030	7.914E-13	1.770E-14
-	4	3.291	0.037	0.483	0.027	5.704E-13	1.209E-14
-	5	3.250	0.039	0.401	0.025	4.243E-13	9.013E-15
-	6	3.220	0.042	0.491	0.030	3.336E-13	7.992E-15
-	7	3.158	0.035	0.437	0.022	2.361E-13	4.500E-15
-	8	3.012	0.043	0.415	0.024	1.573E-13	3.481E-15
-	9	3.011	0.051	0.404	0.026	9.503E-14	2.336E-15
-	10	3.087	0.101	0.419	0.054	6.314E-14	3.006E-15
A1068	1	3.123	0.055	0.631	0.048	5.377E-12	1.481E-13
-	2	4.691	0.197	0.384	0.053	1.078E-12	3.785E-14
-	3	4.743	0.201	-	-	2.483E-13	9.377E-15
-	4	5.366	0.352	-	-	6.827E-14	3.351E-15
-	5	5.163	0.543	-	-	2.801E-14	1.829E-15
-	6	5.287	0.867	-	-	1.384E-14	1.288E-15
-	7	2.220	0.562	-	-	2.919E-15	5.567E-16
A1413	1	7.682	0.332	0.409	0.079	4.639E-12	1.199E-13
-	2	7.995	0.327	0.396	0.076	1.899E-12	5.545E-14
-	3	6.898	0.269	0.492	0.061	6.280E-13	1.758E-14
-	4	7.013	0.403	0.338	0.075	2.006E-13	7.082E-15
-	5	6.806	0.366	-	-	8.671E-14	3.446E-15
-	6	6.423	0.530	0.163	0.104	4.190E-14	2.437E-15
-	7	5.650	0.615	-	-	2.249E-14	1.462E-15
-	8	3.559	0.528	-	-	8.913E-15	1.024E-15
-	9	5.015	2.030	-	-	2.495E-15	7.554E-16
A1589	1	2.634	2.668	0.276	0.146	2.234E-13	1.104E-13

TABLE 4—*Continued*

Cluster	Annulus	T (keV)	σ_T (keV)	A	σ_A	F ergs cm^{-2} s^{-1}	σ_F ergs cm^{-2} s^{-1}
-	2	5.080	0.780	-	-	2.203E-13	2.594E-14
-	3	4.676	0.308	-	-	1.645E-13	1.469E-14
-	4	5.614	0.463	0.281	0.115	1.150E-13	8.018E-15
-	5	4.443	0.339	-	-	7.515E-14	6.015E-15
-	6	3.326	0.203	0.317	0.079	4.498E-14	3.912E-15
-	7	3.583	0.291	-	-	2.948E-14	2.445E-15
-	8	3.232	0.445	-	-	9.579E-15	1.204E-15
-	9	1.588	0.204	-	-	1.953E-15	7.190E-16
A1650	1	5.145	0.114	0.654	0.069	4.832E-12	1.220E-13
-	2	6.064	0.158	0.543	0.059	2.196E-12	5.262E-14
-	3	5.812	0.126	0.396	0.040	9.004E-13	1.727E-14
-	4	5.951	0.163	0.306	0.049	3.821E-13	9.047E-15
-	5	5.401	0.141	0.332	0.061	1.828E-13	5.567E-15
-	6	5.235	0.206	0.199	0.051	1.017E-13	3.299E-15
-	7	4.967	0.244	-	-	4.088E-14	1.493E-15
-	8	3.938	0.337	-	-	1.606E-14	1.001E-15
-	9	1.991	0.219	-	-	4.182E-15	6.418E-16
A1689	1	9.435	0.280	0.437	0.048	9.087E-12	1.174E-13
-	2	11.619	0.593	0.258	0.031	2.505E-12	4.687E-14
-	3	9.927	0.309	-	-	7.202E-13	1.216E-14
-	4	8.234	0.360	-	-	1.702E-13	3.949E-15
-	5	9.743	0.780	-	-	7.142E-14	2.160E-15
-	6	7.357	0.913	-	-	2.785E-14	1.265E-15
-	7	7.804	1.481	-	-	1.113E-14	7.813E-16
A1775	1	4.341	0.382	1.687	0.517	7.223E-13	1.356E-13
-	2	3.716	0.155	0.913	0.157	7.036E-13	5.628E-14
-	3	3.862	0.089	0.711	0.070	3.867E-13	1.647E-14
-	4	3.660	0.116	0.582	0.077	1.647E-13	8.458E-15
-	5	3.413	0.116	0.404	0.083	8.308E-14	5.222E-15
-	6	3.896	0.221	0.315	0.120	5.016E-14	4.034E-15
-	7	3.276	0.166	0.363	0.078	2.834E-14	1.956E-15
-	8	3.201	0.268	-	-	1.386E-14	1.192E-15
-	9	3.546	0.744	-	-	5.478E-15	7.933E-16
-	10	3.217	0.880	-	-	4.229E-15	9.473E-16
A1795	1	3.881	0.037	0.702	0.027	1.328E-11	1.146E-13
-	2	4.707	0.054	0.553	0.027	6.189E-12	6.440E-14
-	3	5.742	0.070	0.407	0.022	2.267E-12	2.210E-14
-	4	5.958	0.092	0.338	0.028	8.825E-13	1.151E-14
-	5	6.124	0.112	0.316	0.021	4.640E-13	5.640E-15
-	6	6.060	0.141	-	-	2.574E-13	3.550E-15

TABLE 4—*Continued*

Cluster	Annulus	T (keV)	σ_T (keV)	A	σ_A	F ergs cm^{-2} s^{-1}	σ_F ergs cm^{-2} s^{-1}
-	7	5.805	0.150	-	-	1.394E-13	2.031E-15
-	8	5.744	0.248	-	-	5.622E-14	1.210E-15
-	9	4.880	0.292	-	-	2.091E-14	8.567E-16
-	10	4.426	0.693	-	-	1.115E-14	9.853E-16
A1835	1	6.062	0.121	0.457	0.034	1.099E-11	1.152E-13
-	2	10.524	0.495	0.284	0.046	1.743E-12	3.828E-14
-	3	9.123	0.497	-	-	4.054E-13	1.008E-14
-	4	8.632	0.793	-	-	8.954E-14	3.901E-15
-	5	7.667	0.741	-	-	4.165E-14	1.765E-15
-	6	8.092	1.650	-	-	1.544E-14	1.257E-15
-	7	4.969	1.125	-	-	6.206E-15	7.628E-16
A1835a	1	5.896	0.114	0.513	0.034	1.078E-11	1.148E-13
-	2	10.024	0.466	0.364	0.082	1.682E-12	4.944E-14
-	3	9.790	0.456	0.266	0.062	4.036E-13	1.102E-14
-	4	8.517	0.630	-	-	7.844E-14	3.134E-15
-	5	7.891	0.958	-	-	3.176E-14	1.698E-15
-	6	6.411	1.301	-	-	1.120E-14	1.102E-15
-	7	7.612	2.568	-	-	6.764E-15	8.281E-16
-	8	3.138	0.926	-	-	2.740E-15	6.126E-16
-	9	3.325	1.748	-	-	1.290E-15	5.539E-16
A1837	1	3.959	0.256	1.268	0.386	5.620E-13	9.212E-14
-	2	4.110	0.143	0.484	0.106	4.097E-13	2.530E-14
-	3	3.855	0.088	0.469	0.053	2.367E-13	8.884E-15
-	4	3.860	0.112	0.453	0.068	1.071E-13	4.996E-15
-	5	3.393	0.122	0.196	0.035	5.081E-14	2.176E-15
-	6	3.286	0.160	-	-	2.941E-14	1.293E-15
-	7	2.678	0.122	-	-	1.616E-14	7.874E-16
-	8	2.893	0.320	-	-	6.978E-15	5.543E-16
-	9	1.621	0.099	-	-	2.805E-15	3.821E-16
A1914	1	11.219	1.021	0.614	0.126	4.565E-12	1.879E-13
-	2	12.007	0.728	0.329	0.083	3.317E-12	1.139E-13
-	3	10.327	0.422	0.242	0.070	7.948E-13	2.476E-14
-	4	8.967	0.712	0.336	0.117	1.845E-13	9.038E-15
-	5	9.057	1.015	0.326	0.194	8.221E-14	6.265E-15
-	6	8.996	1.556	0.280	0.238	3.770E-14	3.642E-15
-	7	8.053	1.404	-	-	1.673E-14	1.746E-15
A1991	1	1.785	0.033	0.654	0.043	3.296E-12	1.426E-13
-	2	2.611	0.057	0.778	0.082	9.264E-13	5.678E-14
-	3	2.795	0.075	0.451	0.050	2.954E-13	1.390E-14
-	4	2.603	0.087	0.310	0.044	9.172E-14	5.047E-15

TABLE 4—*Continued*

Cluster	Annulus	T (keV)	σ_T (keV)	A	σ_A	F ergs cm^{-2} s^{-1}	σ_F ergs cm^{-2} s^{-1}
-	5	2.388	0.106	-	-	5.005E-14	3.211E-15
-	6	2.377	0.183	0.308	0.100	2.319E-14	3.011E-15
-	7	2.262	0.235	0.230	0.072	1.140E-14	1.456E-15
-	8	1.573	0.126	-	-	4.611E-15	1.003E-15
A2029	1	5.585	0.134	0.951	0.065	1.900E-11	2.732E-13
-	2	7.273	0.224	0.483	0.058	8.060E-12	1.335E-13
-	3	7.827	0.189	0.377	0.044	2.905E-12	4.747E-14
-	4	7.558	0.250	0.382	0.061	1.029E-12	2.500E-14
-	5	7.695	0.322	0.367	0.064	5.066E-13	1.396E-14
-	6	8.187	0.403	-	-	2.837E-13	8.437E-15
-	7	7.531	0.429	-	-	1.515E-13	6.381E-15
-	8	10.599	1.042	-	-	6.345E-14	3.422E-15
A2052	1	1.968	0.021	0.701	0.031	5.517E-12	1.274E-13
-	2	2.839	0.038	0.805	0.037	2.871E-12	6.694E-14
-	3	3.105	0.033	0.552	0.026	1.085E-12	2.145E-14
-	4	3.254	0.041	0.454	0.029	4.902E-13	1.128E-14
-	5	3.230	0.049	0.393	0.032	2.827E-13	7.523E-15
-	6	3.053	0.058	0.442	0.038	1.698E-13	5.478E-15
-	7	2.913	0.061	0.341	0.031	9.754E-14	2.998E-15
-	8	3.027	0.103	0.420	0.057	4.174E-14	2.174E-15
-	9	2.633	0.119	0.421	0.076	1.733E-14	1.510E-15
-	10	2.517	0.197	-	-	1.146E-14	1.355E-15
A2065	1	4.236	0.123	0.829	0.124	2.491E-12	1.383E-13
-	2	5.182	0.190	0.402	0.096	1.306E-12	5.790E-14
-	3	5.704	0.176	0.461	0.059	7.381E-13	2.137E-14
-	4	5.906	0.210	0.343	0.065	3.649E-13	1.177E-14
-	5	5.823	0.242	0.309	0.080	2.276E-13	8.610E-15
-	6	5.374	0.188	0.430	0.103	1.441E-13	7.013E-15
-	7	4.880	0.192	0.331	0.066	9.532E-14	3.770E-15
-	8	4.719	0.339	-	-	4.190E-14	2.150E-15
-	9	4.824	0.655	-	-	1.682E-14	1.445E-15
-	10	4.967	1.320	-	-	1.160E-14	1.789E-15
A2163	1	9.871	1.153	0.648	0.227	3.807E-12	2.550E-13
-	2	11.801	1.177	0.250	0.068	2.939E-12	1.120E-13
-	3	12.472	0.835	-	-	1.337E-12	4.896E-14
-	4	13.101	1.117	0.331	0.095	4.721E-13	2.303E-14
-	5	15.446	1.803	-	-	2.505E-13	1.215E-14
-	6	13.591	1.745	-	-	1.397E-13	8.328E-15
-	7	13.884	2.783	-	-	6.871E-14	4.199E-15
-	8	7.125	1.593	-	-	2.234E-14	2.046E-15

TABLE 4—*Continued*

Cluster	Annulus	T (keV)	σ_T (keV)	A	σ_A	F ergs cm^{-2} s^{-1}	σ_F ergs cm^{-2} s^{-1}
-	9	6.906	5.839	-	-	3.493E-15	1.253E-15
A2199	1	3.011	0.052	1.023	0.063	8.126E-12	2.111E-13
-	2	3.721	0.066	0.695	0.050	4.617E-12	1.066E-13
-	3	4.129	0.046	0.483	0.029	2.649E-12	4.086E-14
-	4	4.278	0.053	0.498	0.035	1.256E-12	2.403E-14
-	5	4.161	0.061	0.430	0.037	7.471E-13	1.610E-14
-	6	4.272	0.074	0.383	0.044	4.469E-13	1.137E-14
-	7	4.251	0.071	0.396	0.042	2.695E-13	6.608E-15
-	8	4.117	0.099	0.519	0.050	1.245E-13	3.927E-15
-	9	4.422	0.192	-	-	6.276E-14	2.291E-15
-	10	4.611	0.390	-	-	3.822E-14	2.302E-15
A2204	1	4.807	0.071	0.655	0.035	1.879E-11	2.017E-13
-	2	8.706	0.433	0.348	0.068	3.387E-12	8.021E-14
-	3	8.335	0.269	0.370	0.061	9.448E-13	2.381E-14
-	4	8.384	0.463	0.372	0.078	2.374E-13	8.514E-15
-	5	8.323	0.575	-	-	1.190E-13	4.758E-15
-	6	9.085	1.276	-	-	5.940E-14	2.980E-15
-	7	7.499	1.109	-	-	2.721E-14	1.662E-15
-	8	7.486	3.432	-	-	6.861E-15	1.134E-15
A2218	1	7.295	0.806	0.730	0.386	1.393E-12	1.795E-13
-	2	8.342	0.599	0.368	0.148	9.645E-13	5.794E-14
-	3	6.759	0.304	0.230	0.059	3.572E-13	1.572E-14
-	4	6.675	0.451	-	-	1.048E-13	5.416E-15
-	5	5.484	0.610	-	-	4.587E-14	2.873E-15
-	6	6.357	0.857	-	-	2.687E-14	1.989E-15
-	7	3.387	0.392	-	-	1.077E-14	1.133E-15
-	8	1.323	0.095	-	-	2.543E-15	7.201E-16
-	9	0.609	0.098	-	-	7.458E-16	4.554E-16
A2256	1	6.241	2.232	0.342	0.063	8.576E-13	8.002E-14
-	2	6.173	0.722	-	-	8.819E-13	4.740E-14
-	3	5.937	0.302	-	-	1.031E-12	3.857E-14
-	4	5.813	0.246	-	-	7.972E-13	2.885E-14
-	5	5.497	0.236	0.434	0.061	5.563E-13	2.105E-14
-	6	6.633	0.263	-	-	4.054E-13	1.479E-14
-	7	6.704	0.240	0.278	0.063	2.179E-13	7.897E-15
-	8	6.767	0.345	-	-	1.103E-13	4.435E-15
-	9	7.647	0.889	-	-	4.244E-14	2.227E-15
-	10	6.727	1.572	-	-	1.428E-14	1.809E-15
A2319	1	8.310	0.811	0.611	0.315	2.251E-12	2.207E-13
-	2	10.162	0.716	0.316	0.132	2.052E-12	8.895E-14

TABLE 4—*Continued*

Cluster	Annulus	T (keV)	σ_T (keV)	A	σ_A	F ergs cm^{-2} s^{-1}	σ_F ergs cm^{-2} s^{-1}
-	3	8.944	0.308	0.265	0.048	2.182E-12	3.932E-14
-	4	8.894	0.272	0.303	0.041	1.738E-12	2.845E-14
-	5	8.427	0.195	0.312	0.044	1.181E-12	2.104E-14
-	6	8.919	0.333	0.313	0.053	7.701E-13	1.633E-14
-	7	9.006	0.313	0.233	0.037	5.671E-13	9.794E-15
-	8	8.871	0.443	-	-	3.489E-13	7.199E-15
-	9	8.448	0.362	-	-	1.907E-13	4.445E-15
-	10	7.671	0.703	-	-	1.211E-13	4.658E-15
A2589	1	3.349	0.107	0.975	0.150	1.749E-12	1.338E-13
-	2	3.730	0.110	0.816	0.096	9.821E-13	5.145E-14
-	3	3.622	0.071	0.582	0.045	6.220E-13	1.894E-14
-	4	3.575	0.081	0.567	0.050	3.139E-13	1.084E-14
-	5	3.579	0.099	0.437	0.055	1.826E-13	7.206E-15
-	6	3.625	0.129	0.449	0.070	1.050E-13	5.071E-15
-	7	3.378	0.098	0.392	0.061	7.137E-14	3.368E-15
-	8	3.473	0.217	0.442	0.097	3.668E-14	2.601E-15
-	9	2.863	0.276	0.307	0.095	1.631E-14	1.736E-15
-	10	4.660	0.880	-	-	1.628E-14	1.744E-15
A2597	1	3.054	0.027	0.530	0.020	1.113E-11	1.054E-13
-	2	3.800	0.055	0.394	0.030	2.562E-12	4.514E-14
-	3	3.869	0.056	0.310	0.028	6.003E-13	1.168E-14
-	4	3.722	0.092	0.299	0.045	1.543E-13	5.011E-15
-	5	3.665	0.120	0.268	0.057	7.358E-14	3.066E-15
-	6	3.399	0.142	0.278	0.079	3.380E-14	2.145E-15
-	7	3.170	0.178	0.372	0.073	1.552E-14	1.043E-15
-	8	2.751	0.311	-	-	6.340E-15	5.927E-16
-	9	2.877	0.438	-	-	3.688E-15	4.266E-16
A2626	1	2.610	0.042	0.693	0.054	2.492E-12	9.715E-14
-	2	3.084	0.066	0.571	0.056	8.441E-13	3.538E-14
-	3	3.134	0.049	0.501	0.036	4.176E-13	1.262E-14
-	4	3.323	0.064	0.448	0.047	1.722E-13	6.440E-15
-	5	3.251	0.086	0.413	0.047	8.561E-14	3.521E-15
-	6	3.288	0.119	-	-	4.422E-14	1.984E-15
-	7	2.762	0.149	0.229	0.055	2.233E-14	1.481E-15
-	8	1.973	0.133	0.271	0.073	7.593E-15	1.039E-15
-	9	1.901	0.261	0.289	0.124	2.561E-15	7.842E-16
-	10	1.685	0.158	-	-	2.120E-15	8.589E-16
A2667	1	5.530	0.196	0.554	0.061	5.890E-12	1.419E-13
-	2	8.529	0.455	0.352	0.061	1.321E-12	4.140E-14
-	3	7.616	0.442	-	-	3.116E-13	1.083E-14

TABLE 4—*Continued*

Cluster	Annulus	T (keV)	σ_T (keV)	A	σ_A	F ergs cm^{-2} s^{-1}	σ_F ergs cm^{-2} s^{-1}
-	4	7.788	0.810	-	-	7.479E-14	3.664E-15
-	5	5.558	0.810	-	-	2.791E-14	1.900E-15
-	6	8.407	2.186	-	-	1.370E-14	1.428E-15
-	7	3.807	0.973	-	-	5.288E-15	7.856E-16
-	8	3.145	0.777	-	-	3.624E-15	6.280E-16
A2717	1	2.040	0.039	0.953	0.085	8.896E-13	6.071E-14
-	2	2.538	0.057	0.819	0.079	3.955E-13	2.396E-14
-	3	2.430	0.044	0.495	0.037	1.952E-13	7.897E-15
-	4	2.497	0.059	0.437	0.044	8.545E-14	4.068E-15
-	5	2.291	0.078	0.359	0.043	4.538E-14	2.503E-15
-	6	2.303	0.107	0.384	0.058	2.579E-14	1.840E-15
-	7	2.310	0.128	0.364	0.063	1.419E-14	1.135E-15
-	8	2.085	0.119	0.473	0.112	5.339E-15	8.498E-16
-	9	1.954	0.199	-	-	2.055E-15	5.416E-16
-	10	1.682	0.118	-	-	1.729E-15	6.422E-16
A3112	1	3.379	0.036	1.113	0.053	9.632E-12	1.837E-13
-	2	4.797	0.100	0.590	0.053	3.081E-12	7.139E-14
-	3	4.979	0.091	0.427	0.040	1.020E-12	2.141E-14
-	4	4.876	0.123	0.518	0.063	3.337E-13	1.077E-14
-	5	4.552	0.165	0.270	0.071	1.499E-13	6.010E-15
-	6	4.697	0.226	0.212	0.050	8.087E-14	2.995E-15
-	7	4.184	0.180	-	-	4.278E-14	1.844E-15
-	8	4.048	0.328	-	-	1.723E-14	1.150E-15
-	9	2.354	0.246	-	-	6.746E-15	8.338E-16
A3158	1	6.253	0.470	0.710	0.472	1.515E-12	2.301E-13
-	2	5.305	0.183	0.724	0.130	1.239E-12	6.591E-14
-	3	5.627	0.160	0.350	0.050	9.060E-13	2.207E-14
-	4	5.293	0.114	0.444	0.054	5.160E-13	1.399E-14
-	5	5.018	0.125	0.433	0.060	3.296E-13	1.037E-14
-	6	5.230	0.151	0.432	0.071	2.049E-13	7.329E-15
-	7	5.014	0.163	0.285	0.066	1.362E-13	4.877E-15
-	8	5.875	0.404	0.279	0.118	7.133E-14	4.062E-15
-	9	6.460	0.525	-	-	3.595E-14	2.439E-15
A3526	1	1.299	0.037	0.503	0.012	1.013E-11	1.383E-13
-	2	1.983	0.010	1.831	0.054	4.244E-12	1.200E-13
-	3	2.558	0.012	1.492	0.032	2.147E-12	3.747E-14
-	4	2.907	0.020	1.176	0.028	1.194E-12	1.998E-14
-	5	3.207	0.023	0.782	0.025	7.746E-13	1.263E-14
-	6	3.268	0.027	0.591	0.023	5.541E-13	9.253E-15
-	7	3.324	0.024	0.482	0.018	4.419E-13	6.056E-15

TABLE 4—*Continued*

Cluster	Annulus	T (keV)	σ_T (keV)	A	σ_A	F ergs cm^{-2} s^{-1}	σ_F ergs cm^{-2} s^{-1}
-	8	3.369	0.030	0.447	0.021	2.902E-13	4.735E-15
-	9	3.372	0.033	0.447	0.023	1.864E-13	3.345E-15
-	10	3.300	0.056	0.487	0.039	1.404E-13	4.330E-15
A3558	1	4.677	0.136	0.761	0.082	2.637E-12	9.444E-14
-	2	5.552	0.168	0.476	0.056	1.790E-12	4.473E-14
-	3	5.757	0.099	0.455	0.032	1.161E-12	1.774E-14
-	4	5.724	0.106	0.378	0.032	6.826E-13	1.083E-14
-	5	5.492	0.105	0.353	0.031	5.075E-13	8.124E-15
-	6	5.114	0.078	0.412	0.034	3.728E-13	6.825E-15
-	7	5.122	0.071	0.294	0.028	2.667E-13	4.196E-15
-	8	4.878	0.097	0.337	0.040	1.373E-13	3.084E-15
-	9	5.043	0.133	0.264	0.053	6.947E-14	2.095E-15
-	10	4.710	0.264	0.376	0.119	4.147E-14	2.783E-15
A3560	1	3.331	0.359	0.346	0.115	2.771E-13	3.057E-14
-	2	3.253	0.190	-	-	2.286E-13	2.237E-14
-	3	3.997	0.139	0.393	0.083	2.083E-13	1.182E-14
-	4	3.841	0.141	0.458	0.083	1.293E-13	7.521E-15
-	5	3.479	0.164	0.351	0.080	9.652E-14	6.174E-15
-	6	3.827	0.182	0.392	0.100	6.497E-14	4.543E-15
-	7	3.693	0.163	0.285	0.069	4.344E-14	2.444E-15
-	8	3.528	0.207	0.329	0.065	2.858E-14	1.756E-15
-	9	3.856	0.246	-	-	2.028E-14	1.380E-15
-	10	4.093	0.442	-	-	1.519E-14	1.414E-15
A3581	1	1.396	0.017	0.432	0.022	3.243E-12	1.129E-13
-	2	1.585	0.013	0.593	0.028	1.484E-12	5.613E-14
-	3	1.764	0.020	0.536	0.022	5.915E-13	1.851E-14
-	4	1.895	0.028	0.346	0.022	2.212E-13	8.023E-15
-	5	1.909	0.035	0.320	0.025	1.221E-13	5.155E-15
-	6	1.886	0.046	0.307	0.030	6.876E-14	3.663E-15
-	7	1.843	0.046	0.238	0.023	4.600E-14	2.222E-15
-	8	1.648	0.034	0.195	0.023	2.526E-14	1.540E-15
-	9	1.623	0.042	0.225	0.031	1.388E-14	1.209E-15
-	10	1.535	0.092	0.176	0.048	9.583E-15	1.583E-15
A3827	1	7.938	0.565	0.682	0.206	2.633E-12	1.693E-13
-	2	6.944	0.373	0.345	0.091	1.718E-12	6.258E-14
-	3	7.144	0.247	0.378	0.054	8.827E-13	2.182E-14
-	4	6.920	0.304	0.385	0.044	3.679E-13	9.221E-15
-	5	6.683	0.257	-	-	1.902E-13	5.267E-15
-	6	6.926	0.498	-	-	1.038E-13	3.296E-15
-	7	5.804	0.382	-	-	5.573E-14	2.028E-15

TABLE 4—*Continued*

Cluster	Annulus	T (keV)	σ_T (keV)	A	σ_A	F ergs cm^{-2} s^{-1}	σ_F ergs cm^{-2} s^{-1}
-	8	5.867	0.650	-	-	2.549E-14	1.463E-15
-	9	6.561	1.230	-	-	1.033E-14	1.292E-15
A3911	1	6.454	0.707	1.265	0.716	5.754E-13	1.407E-13
-	2	6.636	0.467	0.666	0.245	4.875E-13	4.524E-14
-	3	6.389	0.233	0.401-0.080	3.971E-13	1.498E-14	
-	4	5.538	0.246	0.316	0.077	2.185E-13	8.699E-15
-	5	5.591	0.301	0.176	0.049	1.203E-13	4.168E-15
-	6	5.953	0.405	-	-	7.168E-14	2.836E-15
-	7	4.981	0.290	-	-	4.071E-14	1.850E-15
-	8	3.697	0.420	-	-	1.351E-14	1.202E-15
-	9	3.215	0.379	-	-	8.326E-15	1.054E-15
-	10	3.611	1.182	-	-	5.228E-15	1.288E-15
A3921	1	5.234	0.245	0.588	0.160	1.322E-12	9.053E-14
-	2	6.095	0.287	0.341	0.095	9.003E-13	3.817E-14
-	3	5.570	0.183	0.377	0.057	4.962E-13	1.454E-14
-	4	5.302	0.144	0.354	0.059	2.444E-13	7.813E-15
-	5	5.312	0.170	0.479	0.090	1.409E-13	6.181E-15
-	6	5.036	0.232	0.313	0.059	7.505E-14	3.026E-15
-	7	5.577	0.337	-	-	4.503E-14	1.775E-15
-	8	4.711	0.371	-	-	2.138E-14	1.223E-15
-	9	2.551	0.231	-	-	6.745E-15	8.509E-16
-	10	2.854	0.638	-	-	5.575E-15	9.891E-16
A4059	1	2.868	0.071	1.356	0.108	2.976E-12	1.553E-13
-	2	3.688	0.077	0.880	0.069	1.852E-12	6.578E-14
-	3	4.087	0.060	0.503	0.038	9.636E-13	2.209E-14
-	4	4.285	0.078	0.456	0.049	4.045E-13	1.152E-14
-	5	4.154	0.096	0.371	0.056	2.194E-13	7.527E-15
-	6	4.038	0.118	0.411	0.071	1.268E-13	5.547E-15
-	7	4.093	0.121	0.443	0.071	7.628E-14	3.295E-15
-	8	4.118	0.211	0.355	0.093	3.329E-14	2.189E-15
-	9	4.143	0.363	-	-	1.443E-14	1.381E-15
-	10	3.326	0.576	-	-	7.179E-15	1.351E-15
AS 1101	1	2.374	0.026	0.554	0.024	7.165E-12	1.124E-13
-	2	2.600	0.030	0.486	0.027	2.424E-12	5.416E-14
-	3	2.744	0.039	0.351	0.022	6.678E-13	1.480E-14
-	4	2.606	0.051	0.246	0.030	1.739E-13	6.053E-15
-	5	2.620	0.065	0.278	0.039	8.679E-14	3.757E-15
-	6	2.424	0.094	0.155	0.024	4.177E-14	1.873E-15
-	7	2.276	0.121	-	-	1.952E-14	1.069E-15
-	8	1.898	0.136	-	-	7.853E-15	7.060E-16

TABLE 4—*Continued*

Cluster	Annulus	T (keV)	σ_T (keV)	A	σ_A	F ergs cm^{-2} s^{-1}	σ_F ergs cm^{-2} s^{-1}
-	9	1.519	0.140	-	-	2.530E-15	4.775E-16
-	10	1.287	0.085	-	-	2.632E-15	6.152E-16
AWM7	1	2.780	0.056	1.440	0.094	3.722E-12	1.690E-13
-	2	3.351	0.046	1.120	0.070	2.023E-12	7.219E-14
-	3	3.526	0.040	0.798	0.032	1.451E-12	2.728E-14
-	4	3.616	0.040	0.647	0.027	9.924E-13	1.745E-14
-	5	3.728	0.041	0.623	0.028	7.379E-13	1.338E-14
-	6	3.609	0.044	0.538	0.027	5.481E-13	1.018E-14
-	7	3.631	0.039	0.476	0.021	4.421E-13	6.756E-15
-	8	3.547	0.049	0.391	0.024	2.772E-13	4.972E-15
-	9	3.528	0.057	0.434	0.027	1.639E-13	3.389E-15
-	10	3.391	0.079	0.334	0.044	1.108E-13	4.147E-15
Coma	1	9.933	1.389	0.490	0.154	1.500E-12	9.075E-14
-	2	8.079	0.528	-	-	1.326E-12	7.121E-14
-	3	8.396	0.222	0.275	0.056	1.400E-12	2.862E-14
-	4	8.395	0.184	0.257	0.044	1.310E-12	2.179E-14
-	5	8.156	0.168	0.251	0.038	1.165E-12	1.753E-14
-	6	8.324	0.166	0.233	0.039	1.032E-12	1.569E-14
-	7	8.231	0.121	0.297	0.028	9.749E-13	1.109E-14
-	8	8.339	0.132	0.270	0.032	6.986E-13	8.788E-15
-	9	8.140	0.132	0.333	0.033	4.489E-13	6.048E-15
-	10	8.320	0.222	0.278	0.063	3.279E-13	7.793E-15
E1455+2232	1	4.409	0.095	0.503	0.040	4.869E-12	9.767E-14
-	2	5.247	0.244	0.401	0.117	5.104E-13	2.973E-14
-	3	4.954	0.263	0.509	0.125	9.724E-14	6.642E-15
-	4	5.165	0.796	-	-	1.468E-14	1.681E-15
-	5	5.408	0.772	-	-	1.197E-14	1.291E-15
-	6	6.167	2.284	-	-	5.321E-15	9.387E-16
-	7	4.679	3.423	-	-	1.590E-15	6.037E-16
EXO0422	1	2.429	0.027	0.705	0.033	6.726E-12	1.437E-13
-	2	2.938	0.045	0.557	0.037	2.158E-12	6.009E-14
-	3	2.953	0.039	0.389	0.025	8.194E-13	1.924E-14
-	4	3.047	0.055	0.310	0.032	3.005E-13	9.390E-15
-	5	3.140	0.072	0.342	0.044	1.531E-13	6.167E-15
-	6	2.825	0.097	0.402	0.055	8.436E-14	4.571E-15
-	7	2.564	0.078	0.290	0.044	5.283E-14	2.954E-15
-	8	2.296	0.134	0.367	0.075	2.223E-14	2.251E-15
-	9	2.366	0.189	0.244	0.074	1.221E-14	1.515E-15
-	10	3.089	0.434	-	-	1.069E-14	1.353E-15
HYDRA	1	3.251	0.040	0.620	0.035	1.179E-11	1.653E-13

TABLE 4—*Continued*

Cluster	Annulus	T (keV)	σ_T (keV)	A	σ_A	F ergs cm^{-2} s^{-1}	σ_F ergs cm^{-2} s^{-1}
-	2	3.653	0.064	0.468	0.037	3.962E-12	8.092E-14
-	3	3.503	0.057	0.426	0.030	1.247E-12	2.670E-14
-	4	3.810	0.070	0.293	0.034	5.933E-13	1.430E-14
-	5	3.943	0.088	0.346	0.046	2.957E-13	9.141E-15
-	6	3.970	0.127	0.340	0.070	1.451E-13	6.598E-15
-	7	4.170	0.142	0.322	0.071	7.686E-14	3.554E-15
-	8	6.665	0.484	-	-	4.059E-14	2.137E-15
Klemola 44	1	3.141	0.067	0.687	0.063	3.555E-12	1.251E-13
-	2	3.238	0.047	0.628	0.040	2.171E-12	5.538E-14
-	3	3.240	0.033	0.490	0.024	1.225E-12	2.218E-14
-	4	3.241	0.039	0.457	0.027	5.435E-13	1.157E-14
-	5	3.060	0.045	0.417	0.028	3.156E-13	7.587E-15
-	6	3.082	0.056	0.451	0.036	1.857E-13	5.527E-15
-	7	3.002	0.055	0.393	0.030	1.301E-13	3.481E-15
-	8	2.610	0.062	0.251	0.031	6.013E-14	2.238E-15
-	9	2.402	0.086	0.215	0.031	3.037E-14	1.495E-15
-	10	2.093	0.128	0.140	0.044	1.693E-14	1.663E-15
M87	1	1.517	0.006	0.379	0.007	2.240E-11	1.456E-13
-	2	1.650	0.004	0.879	0.015	7.215E-12	8.012E-14
-	3	1.802	0.006	0.772	0.010	3.905E-12	3.315E-14
-	4	2.033	0.006	0.635	0.009	2.494E-12	2.007E-14
-	5	2.065	0.007	0.556	0.008	1.756E-12	1.468E-14
-	6	2.231	0.011	0.538	0.009	1.242E-12	1.115E-14
-	7	2.347	0.009	0.465	0.007	1.060E-12	7.597E-15
-	8	2.470	0.011	0.406	0.008	6.960E-13	5.754E-15
-	9	2.526	0.013	0.362	0.008	4.294E-13	3.926E-15
-	10	2.604	0.021	0.362	0.014	3.265E-13	4.987E-15
MKW 3S	1	3.043	0.044	0.910	0.048	4.954E-12	1.204E-13
-	2	3.397	0.043	0.656	0.040	2.432E-12	5.666E-14
-	3	3.619	0.047	0.443	0.026	1.032E-12	1.874E-14
-	4	3.812	0.060	0.312	0.030	4.453E-13	9.511E-15
-	5	3.549	0.076	0.287	0.036	2.038E-13	5.607E-15
-	6	3.530	0.099	0.401	0.052	1.131E-13	4.249E-15
-	7	3.473	0.101	0.327	0.046	6.595E-14	2.375E-15
-	8	3.625	0.157	0.482	0.070	3.148E-14	1.678E-15
-	9	3.955	0.225	-	-	1.610E-14	1.046E-15
-	10	4.597	0.866	-	-	8.398E-15	1.077E-15
MKW 4	1	1.573	0.023	1.651	0.184	2.340E-12	3.023E-13
-	2	2.096	0.056	1.521	0.235	5.578E-13	8.200E-14
-	3	2.008	0.052	0.643	0.076	2.307E-13	1.922E-14

TABLE 4—*Continued*

Cluster	Annulus	T (keV)	σ_T (keV)	A	σ_A	F ergs cm^{-2} s^{-1}	σ_F ergs cm^{-2} s^{-1}
-	4	2.001	0.064	0.506	0.074	1.056E-13	9.639E-15
-	5	1.944	0.067	0.483	0.070	7.648E-14	7.030E-15
-	6	1.984	0.078	0.412	0.070	5.420E-14	5.246E-15
-	7	1.741	0.078	0.419	0.056	3.543E-14	3.265E-15
-	8	1.679	0.053	0.278	0.052	1.979E-14	2.187E-15
-	9	1.523	0.079	0.235	0.052	1.160E-14	1.770E-15
-	10	1.244	0.078	0.259	0.103	5.885E-15	2.469E-15
Perseus	1	4.043	0.014	0.477	0.008	5.565E-11	1.485E-13
-	2	3.292	0.007	0.681	0.007	3.332E-11	8.471E-14
-	3	3.686	0.006	0.676	0.005	1.964E-11	3.059E-14
-	4	4.276	0.007	0.610	0.005	9.889E-12	1.953E-14
-	5	5.215	0.014	0.508	0.006	5.551E-12	1.423E-14
-	6	5.766	0.023	0.482	0.008	3.584E-12	1.118E-14
-	7	6.071	0.022	0.456	0.007	2.514E-12	7.591E-15
-	8	6.484	0.028	0.416	0.009	1.631E-12	6.439E-15
-	9	6.741	0.029	0.424	0.010	1.030E-12	4.373E-15
-	10	7.258	0.072	0.405	0.018	7.729E-13	5.581E-15
PKS 0745-19	1	4.875	0.080	0.538	0.033	2.748E-11	2.968E-13
-	2	7.354	0.226	0.413	0.044	7.893E-12	1.208E-13
-	3	7.733	0.210	0.332	0.039	2.275E-12	4.123E-14
-	4	8.278	0.326	0.362	0.065	6.574E-13	1.936E-14
-	5	9.087	0.659	0.463	0.111	2.923E-13	1.282E-14
-	6	8.200	0.616	0.524	0.101	1.514E-13	7.021E-15
-	7	8.579	0.687	-	-	7.834E-14	3.803E-15
-	8	8.506	1.375	-	-	2.868E-14	2.192E-15
-	9	6.472	1.167	-	-	1.626E-14	1.652E-15
-	10	4.732	1.481	-	-	1.090E-14	2.019E-15
RXCJ0605.8-3518	1	3.866	0.089	0.717	0.069	5.409E-12	1.709E-13
-	2	5.408	0.220	0.416	0.103	1.104E-12	5.435E-14
-	3	4.811	0.189	0.227	0.074	3.412E-13	1.525E-14
-	4	4.537	0.286	0.295	0.103	9.945E-14	6.449E-15
-	5	4.834	0.437	-	-	4.333E-14	3.125E-15
-	6	6.248	1.149	-	-	1.980E-14	1.803E-15
-	7	8.425	3.500	-	-	1.031E-14	1.318E-15
RXCJ2234.5-3744	1	11.165	1.896	0.323	0.102	2.133E-12	1.243E-13
-	2	11.087	1.011	-	-	1.577E-12	6.927E-14
-	3	9.664	0.415	0.290	0.055	6.989E-13	1.924E-14
-	4	8.816	0.651	-	-	2.285E-13	7.606E-15
-	5	5.890	0.477	0.198	0.094	7.595E-14	4.053E-15
-	6	4.478	0.584	-	-	2.822E-14	2.157E-15

TABLE 4—*Continued*

Cluster	Annulus	T (keV)	σ_T (keV)	A	σ_A	F ergs cm^{-2} s^{-1}	σ_F ergs cm^{-2} s^{-1}
-	7	3.566	0.594	-	-	1.229E-14	1.282E-15
-	8	2.412	1.099	-	-	2.150E-15	6.970E-16
RXJ0658-55	1	12.257	1.286	0.229	0.050	2.409E-12	1.087E-13
-	2	14.686	1.205	-	-	1.592E-12	6.374E-14
-	3	14.799	0.975	-	-	6.728E-13	2.756E-14
-	4	13.160	1.248	-	-	1.555E-13	8.220E-15
-	5	10.503	1.156	-	-	5.489E-14	3.144E-15
-	6	18.091	6.064	-	-	2.052E-14	2.429E-15
RXJ1347-1145	1	11.426	0.446	0.390	0.045	9.748E-12	1.228E-13
-	2	15.643	1.239	0.214	0.081	9.690E-13	3.289E-14
-	3	11.086	1.179	-	-	1.594E-13	7.219E-15
-	4	7.533	1.484	-	-	1.935E-14	1.795E-15
-	5	10.277	3.281	-	-	9.269E-15	1.140E-15
Sersic 159-3	1	2.365	0.016	0.554	0.015	7.273E-12	7.407E-14
-	2	2.614	0.018	0.466	0.016	2.359E-12	3.257E-14
-	3	2.741	0.024	0.366	0.014	6.529E-13	9.157E-15
-	4	2.642	0.031	0.278	0.019	1.670E-13	3.664E-15
-	5	2.572	0.041	0.224	0.021	8.322E-14	2.222E-15
-	6	2.523	0.061	0.255	0.030	4.061E-14	1.531E-15
-	7	2.093	0.056	0.152	0.018	1.848E-14	7.610E-16
-	8	1.681	0.053	-	-	6.327E-15	4.433E-16
-	9	1.322	0.059	-	-	1.637E-15	2.912E-16
-	10	2.491	0.528	-	-	2.306E-15	4.364E-16
Triangulum	1	10.192	1.381	0.554	0.588	3.323E-12	5.096E-13
-	2	11.615	1.334	0.344	0.172	3.126E-12	1.832E-13
-	3	9.432	0.388	0.330	0.066	2.436E-12	5.881E-14
-	4	9.337	0.388	0.308	0.065	1.538E-12	3.850E-14
-	5	9.405	0.410	0.272	0.067	1.053E-12	2.798E-14
-	6	9.528	0.450	0.222	0.074	7.344E-13	2.127E-14
-	7	8.379	0.252	0.331	0.043	5.297E-13	1.111E-14
-	8	9.156	0.495	-	-	2.796E-13	6.509E-15
-	9	8.701	0.633	-	-	1.385E-13	3.779E-15
-	10	13.256	2.205	-	-	9.028E-14	6.007E-15
ZW3146	1	5.289	0.068	0.517	0.028	7.745E-12	8.265E-14
-	2	8.106	0.259	0.255	0.054	1.116E-12	2.726E-14
-	3	7.668	0.312	0.221	0.053	1.985E-13	5.647E-15
-	4	7.542	0.746	-	-	3.378E-14	1.618E-15
-	5	10.906	2.961	-	-	1.589E-14	1.395E-15
-	6	6.385	1.955	-	-	4.422E-15	6.419E-16